SAPIENZA
UNIVERSITÀ DI ROMA

Hierarchical 3D Models of the Mineralized Collagen Fibrils

Faculty of Civil and Industrial Engineering

Department of Mechanical and Aerospace Engineering

Research Doctorate in Industrial and Management Engineering – XXXIII Cycle

Supervisors

Prof. Franco Marinozzi

Prof. Fabiano Bini

PhD Candidate

Andrada Pica

Academic Year 2020 - 2021

Hierarchical 3D Models of the Mineralized Collagen Fibrils

Ph.D. Thesis – Sapienza University of Rome

ABSTRACT

Bone tissue is characterized by a remarkable hierarchical structure, from nano – to macro – scale. The structural organization of bone is based on the nanoscale building block, i.e. the mineralized collagen fibril, mainly composed of type I collagen, apatite minerals and water. The properties at the nanoscale define the behaviour of the macroscale. Several experimental techniques have been used to assess the arrangement of bone components at the nanoscale, but information is still elusive due to resolution limits. Computational modelling can be used as a complementary method to model and quantify the main nanoscale mechanisms that influence the properties of bone tissue.

This Thesis aims to provide further insights into the nanostructure of human bone tissue. An initial 3D model of a unit cell of the mineralized collagen fibril is developed based on the 2D models available in Literature. Subsequently, a system of equations is implemented to describe the diffusion phenomenon at the collagen-apatite level of porosity. Monte Carlo method is used to consider the majority of the unit cell geometric characteristics and possible flow paths in the three main directions of a coordinate system aligned with the axes of a single trabecula. The outcomes allow to assess the orientation of the apatite platelets and to provide information concerning structural factors that mainly influence water diffusion within the mineralized collagen fibril.

A further step of this Thesis concerns the development of a 3D geometric model of the entire mineralized collagen fibril. The study aims to analyse the effects of the mineral volume fraction on the organization of the nanostructure by means of the continuum percolation theory. The latter is a pillar of statistical physics that studies the connectivity in a system. It is the first attempt to determine whether the mineralized collagen fibril may develop an extended network of connected apatite minerals. The methodology of the continuum percolation is adapted to the geometry of the mineralized collagen fibril and the Monte Carlo method is implemented for ten different mineral volume fractions. The outcomes provide evidence that for hypermineralized conditions, the number of extended network of minerals increases. Therefore, an abnormal mineral arrangement at the nanostructure may contribute to the critical behaviour of the tissue.

The outcomes of the presented research related to the apatite arrangement at bone nanoscale may facilitate the design and optimization of bio-scaffolds for tissue engineering. In-depth knowledge of bone nanostructure is essential to enhance the longevity of bio-scaffolds and to decrease the risk of failure.

SOMMARIO

Il tessuto osseo è caratterizzato da una struttura gerarchica complessa, che comprende diversi livelli a partire dalla scala nanometrica fino alla macroscala. L'organizzazione multiscala dell'osso si basa sull'unità strutturale fondamentale della nanoscala, la fibrilla mineralizzata di collagene, costituita principalmente da collagene di tipo I, cristalli di apatite ed acqua. Le proprietà del tessuto alla nanoscala definiscono il comportamento osseo a livello macroscopico. Per analizzare l'organizzazione spaziale dei componenti primari dell'osso a livello nanometrico si possono applicare diverse tecniche sperimentali. Tuttavia, le informazioni presenti in letteratura sono limitate a causa dell'insufficiente risoluzione delle tecniche utilizzate. I modelli computazionali rappresentano metodi complementari per sviluppare modelli e quantificare i principali meccanismi al livello della nanoscala che influenzano le proprietà del tessuto osseo.

Questa Tesi ha l'obiettivo di approfondire alcuni aspetti attinenti all'organizzazione della nanostruttura del tessuto osseo umano. Inizialmente, è stato sviluppato un modello 3D di un'unità strutturale ripetitiva della fibrilla mineralizzata di collagene, a partire da modelli 2D presenti in Letteratura. Successivamente, è stato implementato un sistema di equazioni per descrivere il fenomeno della diffusione al livello di porosità collagene - apatite. Lo studio computazionale si basa sul metodo probabilistico Monte Carlo, al fine di poter considerare la maggior parte dei valori numerici che caratterizzano la geometria dell'unità strutturale e per analizzare la maggioranza dei percorsi che una particella di fluido può compiere nelle tre direzioni principali di un sistema di riferimento allineato con gli assi di una singola trabecola. I risultati permettono di valutare l'orientamento dei cristalli di apatite. Si ottengono, inoltre, informazioni riguardo i fattori strutturali che influenzano principalmente la diffusione dell'acqua all'interno della fibrilla mineralizzata di collagene.

Successivamente, è stato sviluppato un modello geometrico 3D dell'intera fibrilla mineralizzata di collagene. Lo studio ha lo scopo di analizzare gli effetti del grado di mineralizzazione sull'organizzazione strutturale dei nanocomponenti del tessuto osseo mediante la teoria della percolazione nel mezzo continuo. Quest'ultimo metodo rappresenta un pilastro della fisica statistica che studia la connettività in un sistema. Si tratta del primo tentativo di determinare se la fibrilla mineralizzata di collagene sia in grado di sviluppare una rete estesa di cristalli di apatite connessi tra loro. La metodologia della percolazione nel continuo è stata adattata alla geometria della fibrilla

mineralizzata di collagene e la tecnica Monte Carlo è stata implementata per dieci valori diversi di mineralizzazione. I risultati evidenziano che in condizioni di ipermineralizzazione, il numero di reti estese costituite da minerali connessi aumenta. Quindi un'anomala disposizione del minerale a livello della nanoscala può contribuire ad un comportamento critico del tessuto osseo.

I risultati presentati in questa Tesi attinenti all'organizzazione dell'apatite a livello nanometrico possono facilitare la progettazione e l'ottimizzazione di scaffold (sostituti ossei) per l'ingegneria tissutale. La conoscenza approfondita della nanostruttura dell'osso è fondamentale per aumentare la longevità degli scaffold e per diminuire il rischio di cedimento.

Acknowledgements

I take this opportunity to thank my supervisors, Prof. Franco Marinozzi and Prof. Fabiano Bini for all teachings, insightful discussions and professional guidance during the PhD experience. I thank you for giving me the opportunity to further study this compelling research topic.

I would also like to thank my parents for the continuous support, encouragement and guidance throughout my life.

Table of Contents

Introduction **17**

1.1 General context of the study 17

1.2 Objective of the Thesis 19

1.3 Overview of the Thesis 19

Background: Bone structure and organization **21**

2.1 Bone functions 22

2.2 Bone composition 24

2.3 Nanoscale organization of bone 24

2.3.1 Collagen fibril 24

2.3.2 Apatite mineral 26

2.3.2.1 Mineral shape and size 27

2.3.2.2 Mineral orientation 30

2.3.2.3 Mineral-collagen arrangement 32

2.3.2.4 Mineral volume fraction 32

2.3.2.5 Amorphous calcium phosphate layer 33

2.3.3 Water 34

2.3.4 Non-collagenous protein 35

2.4 Models of the mineralized collagen fibril 36

2.4.1 Mechanical models 36

2.4.2 Finite element models 39

2.4.3 Molecular dynamics studies 41

3D Model of Water Diffusion within the Human Mineralized Collagen Fibril **44**

3.1 INTRODUCTION 45

3.1.1 State of art of water diffusion studies within the mineralized collagen fibril 45

3.1.2 State of art of diffusion coefficient assessment methods 47
3.1.3. Introduction to Monte Carlo Technique 50
3.1.4 Aim of the study 52
3.2 METHODS 52
3.2.1 Geometric model 52
3.2.2. Diffusion coefficient 56
3.2.3 Tortuosity 57
3.2.3.1 Determination of tortuosity in the mineral matrix 57
3.2.3.2 Determination of tortuosity in the collagen matrix 58
3.2.4 Constrictivity 60
3.2.5 Porosity 61
3.2.6 Determination of the diffusion coefficients 61
3.2.7 Statistical analysis 62
3.3 RESULTS 63
3.4 DISCUSSIONS 68
Percolation in a 3D Model of the Human Mineralized Collagen Fibril 71
4.1 INTRODUCTION 72
4.1.1 Problem contextualization 72
4.1.2 Percolation theory 73
4.1.2.1 Discrete percolation 74
4.1.2.2 Continuum percolation 75
4.1.3 Aim of the study 79
4.2 METHODS 80
4.2.1 Initial configuration of mineral within the MCF 80
4.2.2 Generating configurations 84
4.2.2.1 Detection of interpenetrating platelets 87
4.2.3 Equilibrium 90
4.2.3.1 Radial distribution function 90

4.2.3.2 Nematic order parameter 96
4.2.4 Cluster identification 98
4.2.5 Percolating cluster assessment 100
4.3 RESULTS 104
4.4 DISCUSSIONS 109
Conclusions and perspectives 114
5.1 Conclusions 115
5.2 Future perspectives 119
Appendix A 121
Appendix B 124
Appendix C: Publications and presentations 137
REFERENCES 138

List of Figures

Figure 2.1: Schematic illustration of the hierarchical organization of trabecular bone tissue …….. 23

Figure 3.1: Schematic representation of the mineralized collagen fibril composed of tropocollagen molecules (light yellow region) and apatite platelets (grey region). Four unit cells of bone nanostructure are illustrated in order to represent the spatial arrangement of the apatite mineral embedded in the organic matrix of collagen. Each unit cell is constituted by three apatite platelets disposed in a staggered configuration in the longitudinal direction. The inclination of mineral with respect to the longitudinal axis **L** is identified by the angle θ_{LT} in the LT plane, and by θ_{LW} in the LW plane. In the WT plane, the inclination, θ_{WT}, is considered with respect to the width axis **W**. There are also indicated the variables that characterize the geometric parameters of the platelet (L, W, T) the distance between the platelets (a_L, a_W and a_T) and the period length (D_{period}) between adjacent mineral platelets in the longitudinal direction. …… 53

Figure 3.2: Diffusion coefficient (D_L) for a flow parallel to the longitudinal axis (L) represented in function of the constrictivity (a, c, e, g) and tortuosity factors (b, d, f, h) for different mineralization degrees, i.e. $V_{f\_A} = 0.07$ (a, b), $V_{f\_A} = 0.32$ (c, d), $V_{f\_A} = 0.42$ (e, f) and $V_{f\_A} = 0.52$ (g, h). The colour gradient indicates the standard deviation (σ_{LT}) of the Gaussian PDF that characterizes the inclination of the apatite minerals in the LT plane. The grey bands show the Confidence Interval at 95 percent. …….. 65

Figure 3.3: Diffusion coefficient (D_W) for a flow parallel to the width direction (W) represented in function of the constrictivity (a, c, e, g) and tortuosity factors (b, d, f, h) for different mineralization degrees, i.e. $V_{f\_A} = 0.07$ (a, b), $V_{f\_A} = 0.32$ (c, d), $V_{f\_A} = 0.42$ (e, f) and $V_{f\_A} = 0.52$ (g, h). The colour gradient indicates the standard deviation (σ_{LW}) of the Gaussian PDF that characterizes the inclination of the apatite minerals in the LW plane. The grey bands show the Confidence Interval at 95 percent. …….. 66

Figure 3.4: Diffusion coefficient (D_T) for a flow parallel to the thickness direction (T) represented in function of the constrictivity (a, c, e, g) and tortuosity factors (b, d, f, h) for different mineralization degrees, i.e. $V_{f\_A} = 0.07$ (a, b), $V_{f\_A} = 0.32$ (c, d), $V_{f\_A} = 0.42$ (e, f) and $V_{f\_A} = 0.52$ (g, h). The colour gradient indicates the standard deviation (σ_{LT}) of the Gaussian PDF that characterizes the inclination of the apatite minerals in the LT plane. The grey bands show the Confidence Interval at 95 percent. …… 67

Figure 4.1: Bond networks on a square lattice below (a) and above (b) the percolation threshold. In (c) and (d) site networks on a square lattice below and above the percolation threshold, respectively. …… 75

Figure 4.2: (a) Representation of the staggered prismatic lattice (orange) used for the generation of the starting configuration for the 3D apatite model (grey). The

centroids (blue dots) of apatite platelets are placed in correspondence of the lattice sites (b). The configuration of mineral platelets is initialized by occupying the lattice sites randomly. ……..…… 81
Figure 4.3: Comparison of acceptance ratio of perturbed platelets, maximum displacement and inclination factors between configurations realized with two interpenetration conditions of mineral platelets, i.e. allowed interpenetration up to 5 percent (a, c, e) and up to 10 percent (b, d, f) of platelet volume. …… 86
Figure 4.4: Spherical (a) and ellipsoidal (b) shells used in the algorithm of the radial distribution function in the equatorial plane and longitudinal direction, respectively. The black points represent the centroids of the platelets (grey) at equilibrium within the MCF with a diameter of 200 nm. The distance r represents the distance from the refence platelet, while Δr is the shell thickness. ……. 91
Figure 4.5: Typical plot highlighting the artificial decay of the Radial distribution function $g_2(r)$ for large interplatelets distance r in the equatorial plane (a, b) and in longitudinal direction (c, d) due to the boundaries of the finite sample volume. The RDF is computed for an equilibrium configuration of platelets at 32 percent mineral VF within the MCF characterized by a diameter of 50 nm (a, c) and 200 nm (b, d), without taking into account periodic boundaries conditions. ……. 92
Figure 4.6: Radial distribution function $g_2(r)$ in function of interplatelets distance r in the equatorial plane (a, c, e, g) and in longitudinal direction (b, d, f, h) for an equilibrium configuration of platelets at 7 percent (a, b), 32 percent (c, d), 42 percent (e, f) and 52 percent (g, h) of mineral VF within the MCF characterized by a diameter of 50 nm. ……. 94
Figure 4.7: Radial distribution function $g_2(r)$ in function of interplatelets distance r in the equatorial plane (a, c, e, g) and in longitudinal direction (b, d, f, h) for an equilibrium configuration of platelets at 7 percent (a, b), 32 percent (c, d), 42 percent (e, f) and 52 percent (g, h) of mineral VF within the MCF characterized by a diameter of 200 nm. ……... 95
Figure 4.8: Nematic order parameter calculated for mineral volume fraction of 7 percent (a, b), 32 percent (c, d), 42 percent (e,f) and 52 percent (g, h) within the mineralized collagen fibril with diameter of 50 nm (a, c, e,g) and 200 nm (b, d, f,h) 97
Figure 4.9: In (a) illustration of a group of connected platelets that verify the connectedness criterion based on the cut off distance δ = 14 Å of long-range interactions between minerals is represented. Apatite platelets (blue-gray regions) are covered by a shell (yellow) of thickness δ/2 that mimics the long-range interactions which occur between apatite crystals due to their hydrated layers. In (b) a representation of a group of interpenetrating platelets is depicted. …… 100
Figure 4.10: Typical clusters spanning the mineralized collagen fibril of 200 nm diameter in the equatorial plane, namely in W direction (a) and T direction (b). Depicted clusters are composed of interpenetrating platelets. …… 101
Figure 4.11: Typical cluster spanning the mineralized collagen fibril of 200 nm diameter in the longitudinal direction. Depicted cluster is composed of interpenetrating platelets. ……... 103

Figure 4.12: Frequency of percolating clusters (%) in function of cluster size, i.e. number of apatite platelets, for a mineral volume fraction of 7 percent in the equatorial plane of the mineralized collagen fibril (MCF) with diameter of 50 nm (a, b) and 200 nm (c). Clusters achieved assuming long-range interaction between minerals (blue) and interpenetrating crystals (light red) are reported. For the MCF of 200 nm diameter, percolating clusters composed of interpenetrating platelets were not found. 105
Figure 4.13: Frequency of percolating clusters (%) in function of cluster size, i.e. number of apatite platelets, for a mineral volume fraction of 7 percent in the longitudinal direction of the mineralized collagen fibril with diameter of 50 nm (a) and 200 nm (b). Spanning clusters were identified only assuming long-range interaction between minerals (blue); percolating clusters composed of interpenetrating platelets were not found. 106
Figure 4.14: Frequency of percolating clusters (%) in function of cluster size, i.e. number of apatite platelets, for mineral volume fraction of 32 percent (a, b), 42 percent (c, d), and 52 percent (e, f) in the equatorial plane of the mineralized collagen fibril with diameter of 50 nm. The dark red curve represents the cumulative frequency (%) of percolating clusters. Clusters achieved assuming long-range interaction between minerals (blue) and interpenetrating crystals (light red) are reported. 107
Figure 4.15: Frequency of percolating clusters (%) in function of cluster size, i.e. number of apatite platelets, for mineral volume fraction of 32 percent (a, b), 42 percent (c, d), and 52 percent (e, f) in the equatorial plane of the mineralized collagen fibril with diameter of 200 nm. The dark red curve represents the cumulative frequency (%) of percolating clusters. Clusters achieved assuming long-range interaction between minerals (blue) and interpenetrating crystals (light red) are reported. 108
Figure 4.16: Frequency of percolating clusters (%) in function of cluster size, i.e. number of apatite platelets, for mineral volume fraction of 32 percent (a, b), 42 percent (c, d), and 52 percent (e,f) in the longitudinal axis of the mineralized collagen fibril with diameter of 50 nm. The dark red curve represents the cumulative frequency (%) of percolating clusters. Clusters achieved assuming long-range interaction between minerals (blue) and interpenetrating crystals (light red) are reported. 110
Figure 4.17: Frequency of percolating clusters (%) in function of cluster size, i.e. number of apatite platelets, mineral volume fraction of 32 percent (a, b), 42 percent (c, d), and 52 percent (e,f) in the longitudinal axis of the mineralized collagen fibril with diameter of 200 nm. The dark red curve represents the cumulative frequency (%) of percolating clusters. Clusters achieved assuming long-range interaction between minerals (blue) and interpenetrating crystals (light red) are reported. 111
Figure A.1: Diffusion coefficient (D_L) for a flow parallel to the longitudinal axis (L) represented in function of the constrictivity (a, c, e, g) and tortuosity factors (b, d, f, h) for different mineralization degrees, i.e. $V_{f\_A} = 0.07$ (a, b), $V_{f\_A} = 0.32$ (c, d), $V_{f\_A} = 0.42$ (e, f) and $V_{f\_A} = 0.52$ (g, h). The colour gradient indicates the standard 121

deviation (σ_{LW}) of the Gaussian PDF that characterizes the inclination of the apatite minerals in the LW plane. The grey bands show the Confidence Interval at 95 percent. ……..

Figure A.2: Diffusion coefficient (D_W) for a flow parallel to the width direction (W) represented in function of the constrictivity (a, c, e, g) and tortuosity factors (b, d, f, h) for different mineralization degrees, i.e. V_{f_A} = 0.07 (a, b), V_{f_A} = 0.32 (c, d), V_{f_A} = 0.42 (e, f) and V_{f_A} = 0.52 (g, h). The colour gradient indicates the standard deviation (σ_{WT}) of the Gaussian PDF that characterizes the inclination of the apatite minerals in the WT plane. The grey bands show the Confidence Interval at 95 percent. …….. 122

Figure A.3: Diffusion coefficient (D_T) for a flow parallel to the thickness direction (T) represented in function of the constrictivity (a, c, e, g) and tortuosity factors (b, d, f, h) for different mineralization degrees, i.e. V_{f_A} = 0.07 (a, b), V_{f_A} = 0.32 (c, d), V_{f_A} = 0.42 (e, f) and V_{f_A} = 0.52 (g, h). The colour gradient indicates the standard deviation (σ_{WT}) of the Gaussian PDF that characterizes the inclination of the apatite minerals in the WT plane. The grey bands show the Confidence Interval at 95 percent. …… 123

Figure B.1: Frequency of percolating clusters (%) in function of cluster size, i.e. number of apatite platelets, for a mineral volume fraction of 12 percent in the equatorial plane of the mineralized collagen fibril with diameter of 50 nm (a, b) and 200 nm (c). Clusters achieved assuming long-range interaction between minerals (blue) and interpenetrating crystals (light red) are reported. For the MCF of 200 nm diameter, percolating clusters composed of interpenetrating platelets were not found. …… 124

Figure B.2: Frequency of percolating clusters (%) in function of cluster size, i.e. number of apatite platelets, for a mineral volume fraction of 12 percent in the longitudinal direction of the mineralized collagen fibril with diameter of 50 nm (a) and 200 nm (b). Spanning clusters were identified only assuming long-range interaction between minerals (blue). ……. 125

Figure B.3: Frequency of percolating clusters (%) in function of cluster size, i.e. number of apatite platelets, for a mineral volume fraction of 17 percent (a, b), 22 percent (c, d), and 27 percent (e,f) in the equatorial plane of the mineralized collagen fibril with diameter of 50 nm. The dark red curve represents the cumulative frequency (%) of percolating clusters. Clusters achieved assuming long-range interaction between minerals (blue) and interpenetrating crystals (light red) are reported. …….. 126

Figure B.4: Frequency of percolating clusters (%) in function of cluster size, i.e. number of apatite platelets, for a mineral volume fraction of 37 percent (a, b), 47 percent (c, d) in the equatorial plane of the mineralized collagen fibril with diameter of 50 nm. The dark red curve represents the cumulative frequency (%) of percolating clusters. Clusters achieved assuming long-range interaction between minerals (blue) and interpenetrating crystals (light red) are reported. …….. 127

Figure B.5: Frequency of percolating clusters (%) in function of cluster size, i.e. number of apatite platelets, for a mineral volume fraction of 17 percent (a, b), 22

percent (c, d), and 27 percent (e,f) in the longitudinal direction of the mineralized collagen fibril with diameter of 50 nm. The dark red curve represents the cumulative frequency (%) of percolating clusters. Clusters achieved assuming long-range interaction between minerals (blue) and interpenetrating crystals (light red) are reported. The clusters have been identified considering a MCF length of 300 nm. … 128

Figure B.6: Frequency of percolating clusters (%) in function of cluster size, i.e. number of apatite platelets, for a mineral volume fraction of 37 percent (a, b), 47 percent (c, d) in the longitudinal direction of the mineralized collagen fibril with diameter of 50 nm. The dark red curve represents the cumulative frequency (%) of percolating clusters. Clusters achieved assuming long-range interaction between minerals (blue) and interpenetrating crystals (light red) are reported. The clusters have been identified considering a MCF length of 300 nm. …… 129

Figure B.7: Frequency of percolating clusters (%) in function of cluster size, i.e. number of apatite platelets, for a mineral volume fraction of 17 percent (a, b), 22 percent (c, d), and 27 percent (e,f) in the equatorial plane of the mineralized collagen fibril with diameter of 200 nm. The dark red curve represents the cumulative frequency (%) of percolating clusters. Clusters achieved assuming long-range interaction between minerals (blue) and interpenetrating crystals (light red) are reported. ……. 130

Figure B.8: Frequency of percolating clusters (%) in function of cluster size, i.e. number of apatite platelets, for a mineral volume fraction of 37 percent (a, b), 47 percent (c, d) in the equatorial plane of the mineralized collagen fibril with diameter of 200 nm. The dark red curve represents the cumulative frequency (%) of percolating clusters. Clusters achieved assuming long-range interaction between minerals (blue) and interpenetrating crystals (light red) are reported. …….. 131

Figure B.9: Frequency of percolating clusters (%) in function of cluster size, i.e. number of apatite platelets, for a mineral volume fraction of 17 percent (a, b), 22 percent (c, d), and 27 percent (e,f) in the longitudinal direction of the mineralized collagen fibril with diameter of 200 nm. The dark red curve represents the cumulative frequency (%) of percolating clusters. The clusters have been identified considering a MCF length of 450 nm. Clusters achieved assuming long-range interaction between minerals (blue) and interpenetrating crystals (light red) are reported. ……. 132

Figure B.10: Frequency of percolating clusters (%) in function of cluster size, i.e. number of apatite platelets, for a mineral volume fraction of 37 percent (a, b), 47 percent (c, d) in the longitudinal direction of the mineralized collagen fibril with diameter of 200 nm. The dark red curve represents the cumulative frequency (%) of percolating clusters. The clusters have been identified considering a MCF length of 450 nm. Clusters achieved assuming long-range interaction between minerals (blue) and interpenetrating crystals (light red) are reported. ……. 133

Figure B.11: Frequency of percolating clusters (%) in function of cluster size, i.e. number of apatite platelets, for a mineral volume fraction of 42 percent (a), 47 percent (b) in the longitudinal direction of the mineralized collagen fibril with 134

diameter of 50 nm. The dark red curve represents the cumulative frequency (%) of percolating clusters. Clusters achieved assuming long-range interaction between minerals. Spanning clusters along the full length of the MCF are considered. …….
Figure B.12: Frequency of percolating clusters (%) in function of cluster size, i.e. number of apatite platelets, for a mineral volume fraction of 52 percent in the longitudinal direction of the mineralized collagen fibril with diameter of 50 nm. The dark red curve represents the cumulative frequency (%) of percolating clusters. Clusters achieved assuming long-range interaction between minerals (blue) and interpenetrating crystals (light red) are reported. Spanning clusters along the full length of the MCF are considered. …….. 134
Figure B.13: Frequency of percolating clusters (%) in function of cluster size, i.e. number of apatite platelets, for a mineral volume fraction of 37 percent (a, b), 42 percent (c, d), 47 percent (e,f) and 52 percent (g,h) in the longitudinal direction of the mineralized collagen fibril with diameter of 200 nm. The dark red curve represents the cumulative frequency (%) of percolating clusters. Clusters achieved assuming long-range interaction between minerals (blue) and interpenetrating crystals (light red) are reported. Spanning clusters along the full length of the MCF are considered. …… 135

List of Tables

Table 2.1: Literature survey of the mineralized collagen fibril (MCF) diameter …… 27
Table 2.2. Literature survey of dimensions of apatite crystals ……. 29
Table 2.3. Literature survey of the orientation of apatite crystals …… 31
Table 2.4. Literature survey of mineral volume fraction …… 33
Table 3.1. Range of values for the dimensions of the apatite platelets and collagen matrix …… 55
Table 3.2. Standard deviation of the Gaussian PDF representing the inclination of the apatite platelets matching the diffusion coefficient in agreement to Marinozzi et al., (2014b) …….. 64
Table 4.1. Pseudo-code for the generation of the initial apatite array …… 83
Table 4.2. Pseudo-code for Metropolis algorithm ……. 89

CHAPTER 1

Introduction

1.1 General context of the study

Nature has developed a wide range of materials with complex hierarchical structures spanning multiple length scales, from nano - to macro - scale. The generation of different structural levels provides the advantage to achieve a material that performs better than its individual components. Thus, nature applies the principle of hierarchical ordering in order to maximize functionality while minimizing weight and energy cost (Wegst et al., 2015).

One of the most impressive materials found in nature is bone which is characterized by a remarkable combination of stiffness for support and toughness for protection. Its hierarchical organization allows the coexistence of these properties that tend to have mutually exclusive relationship. The structural organization of bone rests on the basic building block at the nanoscale, mainly composed of type I collagen, apatite minerals and water.

The understanding of the structure of bone tissue is a topic in constant evolution. New insights were often obtained when new technologies were developed or when existing methods were adapted from a different scientific field (Liebi et al., 2015). Knowledge concerning the correlation between bone composition, structure and mechanical properties has expanded with the development of high resolution tomographic, spectroscopic and microscopic techniques.

Various techniques have been used to assess the arrangement and orientation of bone components at the nanoscale. X-ray based scattering techniques, such as small-angle X-ray scattering

(SAXS), are sensitive to the crystal structure and can provide insights about mineral platelet orientation and thickness (Shahar et al., 2018). Scattering techniques are powerful tools for studying the orientation of anisotropic building blocks. Nonetheless, it is possible to investigate small volumes of interest. It results also important to investigate samples which size can allow to achieve an overview related to the influence of the nanoscale structure over higher length scales (Liebi et al., 2015). In addition, small angle scattering of X-rays, X-ray diffraction, scanning and transmission electron microscopy remain limited to 2D specimens or isotropically oriented nanostructures (Georgiadis et al., 2016). Investigators continue to face resolution limits in observing bone samples at lower length scales. In fact, the resolution of the aforementioned techniques is well above what is needed to resolve the thickness of mineral platelets embedded in the collagen matrix. For instance, scarcely is known about the arrangement of mineral crystals in the orthogonal direction to the collagen fibril long axis.

Therefore, at the nanostructural level, actual imaging techniques provide a limited field of view and do not lead to a complete correlative study concerning the changes in the nanostructure over a macroscopic sample (Liebi et al., 2015). Due to the complex architecture of bone tissue, the current information concerning the details of the structure and organization of the main components of bone at the nanoscale is still elusive.

These constraints limit the investigation that associates structure to mechanical and metabolic functions. Moreover, the technical weaknesses delay studies that may provide insights at nanoscale related to the evolution of bone structural pathologies as osteoporosis.

To overcome the aforementioned limitations, an integrative research field based on computational modelling has developed. Advances in computational power are facilitating the development of new computational techniques, allowing to model and quantify the main nanoscale mechanisms that influence the properties of bone tissue.

A model is a cognitive construct that provides an idealized representation of a portion of nature and that can be used for descriptive and predictive purposes (Viceconti, 2012). Computational modelling can simulate physical, chemical, biological aspects of the real system and study their interactions in a cause-effect approach. By characterizing a system using numerous variables, the simulation can adjust these variables and predict the resulting effects on the system. In silico modelling has developed into a powerful engineering tool to analyse and extend experimental findings. Moreover, complex models have been developed to provide new insights on aspects that cannot be yet assessed experimentally.

The increased capability of computational tools leads to new insights into the organization of bone tissue. In addition, models offer the possibility to study not only structural aspects in physiological conditions, but also to investigate and predict structural changes due to bone disorders and their eventually treatment. Modelling can support the investigations of the correlations between bone architecture at the nanoscale and the mechanical functions. For instance, parametric studies may be performed to identify structural factors that can highly influence bone functionalities.

1.2 Objective of the Thesis

The main scope of the research reported in this Thesis is to develop 3D hierarchical models of bone nanostructure in order to enhance understanding of the spatial organization of the nanoscale main components. The general objectives consist in:

- Determining insights on the arrangement of the apatite crystals platelets within the mineralized collagen fibril using probabilistic computational methods.
- Individuating possible effects of the variation of the mineral content within the mineralized collagen fibril by means of computational models.

1.3 Overview of the Thesis

Chapter 2 contains a general introduction to Bone tissue. Then, the hierarchical level analysed in this Thesis, i.e. mineralized collagen fibril, is described in detail. An overview of the existing computational models of bone nanostructure proposed in literature is also provided.

In **Chapter 3** a geometrical model of a functional recurring unit of the mineralized collagen fibril is presented. The computational model investigates by means of probabilistic techniques the diffusion coefficient of water within the nanostructure. A comparison with experimental data associated with diffusivity allows to obtain information on the orientation of the apatite crystals within the mineralized collagen fibril. Moreover, also the influence of structural parameters of the mineralized collagen fibril on the water diffusion coefficient is studied.

In **Chapter 4** an extended model of the entire mineralized collagen fibril is developed. The effect of the variation of the mineral content on the architecture of the nanostructure is studied under the perspective of the percolation theory. The principles of the percolation theory are described. Then, implementation strategies of the algorithm are outlined. Subsequently the results for several degrees of mineralization and different diameters of the mineralized collagen fibril are presented.

In **Chapter 5** the main findings of the research presented in this thesis are outlined and future perspectives are discussed.

CHAPTER 2

Background: Bone structure and organization

Bone tissue is a complex mineralized connective tissue that displays a hierarchical structure, from nano - to micro - scale. Its properties at the nanoscale define the behaviour of the macroscale. In this Chapter, a general introduction is given on the structure and organization of bone tissue. First, a quick overview is provided for the architecture at all length scales. Next, a thorough discussion concerning bone nanostructure and available methods applied to analyse it are outlined.

2.1 Bone functions

Bone is a complex mineralized connective tissue with a varied arrangement of material structures at several length scales. Bone tissue has multiple functions in the organism, from mechanical support, protection, mineral homeostasis to haematopoiesis (Cowin, 2001). Mainly, it contributes to form the locomotor system. Its multiscale organization leads to the development of outstanding properties. For instance, the mechanical function encompasses load bearing activity, which requires remarkable strength and stiffness (Burr, 2019). In addition, it is also highly adapted to avoid fractures caused by repetitive physiological loading.

Bone has also a protective function towards internal organs and bone marrow. Furthermore, it is a hematopoietic organ and several trabecular regions within the iliac crest, vertebrae and proximal femur are sources of red blood cells (Burr, 2019).

Both cortical and cancellous bone are sites of long-term storage and rapid exchange of ions, i.e. 99 percent calcium, 88 percent phosphorus, 50 percent magnesium and 35 percent sodium, within the mineral phase (Olstza et al., 2007). Regions with extended cancellous regions are responsible for rapid turnover of bone tissue and play a role in the regulation of calcium balance.

An endocrine function has been observed in bone that helps to mediate phosphate and energy metabolism by secreting two hormones: fibroblast growth factor 23 and osteocalcin. In addition, in cooperation with other hormones, bone helps the development of processes in the bone marrow, brain, kidney, and pancreas that affect skeletal tissue mineralization, fat deposition, and glucose metabolism (Burr, 2019).

These fundamental functions are achieved from the organization of bone structure at several hierarchical levels, from nanometer- to millimeter-sized structures. The concept of multiscale hierarchical structure allows for the adaptation and optimization of a material form and structure at each level of hierarchy to meet specific functions (Launey et al., 2010). In healthy conditions, the structure allows the development of a remarkable combination of high stiffness and great toughness, light weight and high strength. According to Weiner et al. (1998), bone properties should be analysed considering the following hierarchical levels of organization: macroscale, mesoscale, microscale, sub-microscale, nanoscale (Figure 2.1). The macroscale represents the whole bone level. At the mesoscale, bone consists of two osseous tissue types: cortical and trabecular bone. In a cross section of a long bone, e.g. femur, it can be observed a dense cortical (compact) shell and a porous cancellous (trabecular) interior region (Rho et al., 1998). These two types are distinguishable at a microstructural

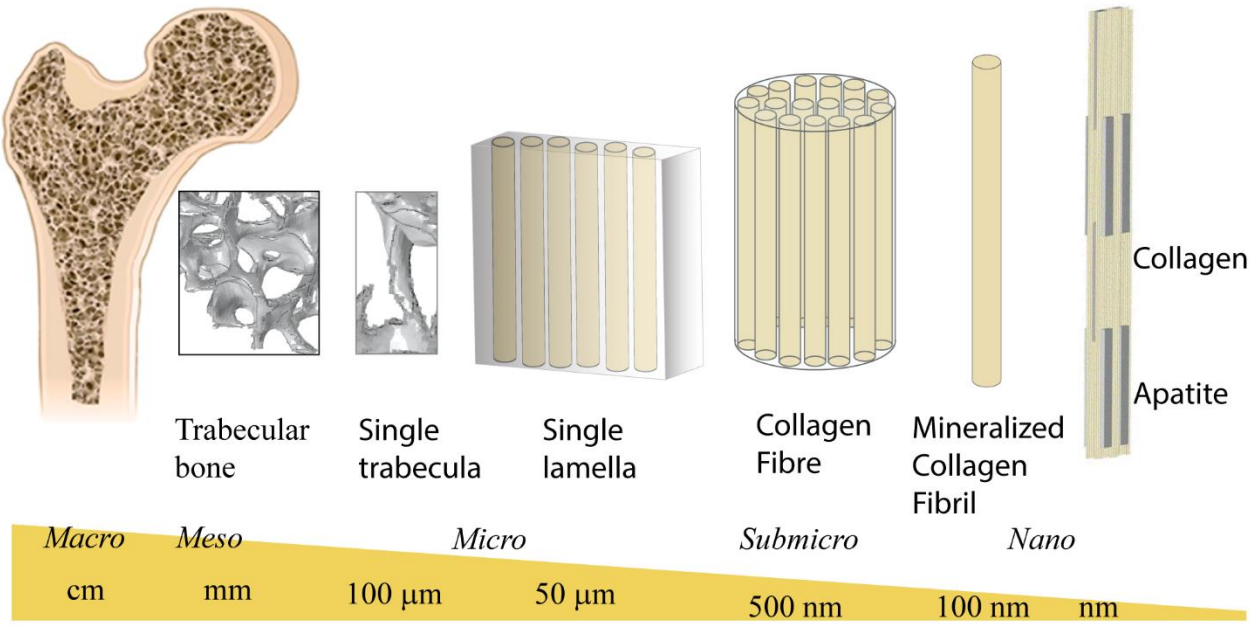

Figure 2.1: Schematic illustration of the hierarchical organization of trabecular bone tissue

level. The microstructure of cortical bone is characterized by osteons or Haversian systems that are composed of blood vessels surrounded by concentric layers of bone tissue (Georgiadis et al., 2015). Trabecular rods and plates can be considered as a foam-like network fully surrounded by bone marrow composing the cancellous compartment of bone (Fratzl et al., 2007). The typical thickness of the trabeculae is approximately 200 - 500 µm with an orientation that depends on the load distribution on the bone (Fratzl et al., 2007).

Both cortical and trabecular bone are composed of lamellae. Depending on the site and specific function addressed to a bone region, lamellae adopt several structural patterns (Reznikov et al., 2014). In trabecular bone an assemblage of slightly differently oriented arrays of lamellae can be found. Conversely, cortical tissue contains parallel or tilted arrays of lamellae.

At the sub-microscale, a single lamella is composed of mineralized collagen fibril bundles or fibres, with a diameter up to several micrometers (Buehler, 2006). Each collagen fibre is constituted in turn by mineralized collagen fibrils, composed of organic matrix of collagen, inorganic phase of mineral and water. Although there are different criteria for describing the hierarchical structures of bone tissues, the basic structural unit is the mineralized collagen fibril.

2.2 Bone composition

Approximately 65 percent of bone weight is composed of mineral, mainly apatite, while the organic component, mostly type I collagen contributes for 20 percent – 25 percent to its composition (Weiner et al., 1998). The remnant approximately 10 percent represents water that can be bound to the mineral-collagen composite or free (Cowin, 2001). Roughly 90 percent of the organic component is type I collagen, with smaller amounts of type III and V collagen (Fratzl, 2008). The remnant 10 percent consists of noncollagenous proteins (NCPs) that have an important role in regulating collagen formation, mineralization, cell attachment and microcrack resistance.

2.3 Nanoscale organization of bone

Significant variations between bone types are encountered at higher levels of bone structure. Conversely, the nanostructural level of organization lies at the foundation of all types of bone (Olstza et al., 2007). At the nanostructural level, the mineralized collagen fibril (MCF) is a characteristic recursive element. The physical and mechanical properties of the MCF influence the general behaviour of bone tissue. Therefore, knowledge of MCF characteristics help comprehend bone properties in healthy and pathological conditions, the effect of aging, physical activity and clinical treatment.

MCF is formed by a combination of collagen fibrils, apatite minerals, water and a small percentage of non-collagenous proteins and proteoglycans. It is still a matter of debate the structural organization, the physical and mechanical properties that lead to this nature - optimized material behaviour.

2.3.1 Collagen fibril

Type I collagen is a fibrous structural protein and it is also a nano - to micro - scale hierarchical material. Collagen molecules, secreted by osteoblasts, self-assemble into fibrils with a specific tertiary structure (Cowin, 2001). Type I collagen is composed of a triple helical polypeptide chain

molecule referred to as tropocollagen molecule. Each tropocollagen molecule consists of a spatial arrangement of three polypeptides, each of which contains one or more regions characterized by repeating amino acid motif (Gly-X-Y) where X and Y can be any amino acid (Fratzl, 2008). This motif allows the chains to form a right-handed triple-helical structure. The triple helical molecule is thus cylindrically shaped, with an approximately diameter of 1.23 nm and lengths of roughly 300 nm (Lees, 1987). Tropocollagen starts to assemble into larger structures using a staggered pattern in the axial direction by a periodic distance of about 67 nm, i.e. D-collagen periodicity (D_{period}). The Hodge-Petruska quarter-stagger scheme requires that adjacent lines of parallel tropocollagen molecules be displaced axially by the distance D_{period}. The staggering of molecules leads to gap zones with $\approx 0.6 \cdot D_{period}$ length and overlap zones with $\approx 0.4 \cdot D_{period}$ length, exhibiting a banded structure visible in transmission electron microscopy (TEM) (Wagermaier et al., 2015).

Staggered arrays of tropocollagen form fibrils. The mineral phase forms intra- and inter-fibrillar patterns as will be discussed in the next section. To continue the description of the hierarchical structure of collagen, several thousand (~4000) of collagen fibrils arrange together to form a collagen fiber (Buehler, 2008).

The 3D arrangement of tropocollagen molecules have been investigated by several authors. Lees et al., (1987) have developed a computational method based on experimental observations that describes the distribution of the organic phase within the MCF. The Authors proposed a packing model for the tropocollagen focusing on the equatorial spacing of molecules in the mineralized tissue. The interdistance between collagen varies depending on water content and mineralization degree. Typical values for lateral distances are in the range 0.6 – 1.2 nm for fully mineralized tissue (Jäger et al., 2000). For the equatorial plane, Lees et al. (1987) propose a quasi-hexagonal packing model with alternate rows in accordance also with the Hulmes-Miller model (Fratzl, 2008).

The collagen packing structure directly affects and it is influenced by the fibrillar organization and its components (Orgel et al., 2014). Orgel and co-workers, in recent times, have provided insights into the conformation of the collagen structures. Their study shows that the topology of the tropocollagen molecules is such that tropocollagen neighbours are arranged to form a supertwisted right-handed microfibril. However, the extent of this supertwist is extremely small, such that the longitudinal axis of the tropocollagen results approximately parallel to the c- axis of the MCF (Orgel et al., 2006).

Lateral and longitudinal aggregation of tropocollagen molecules allows the development of microscale structures. An important characteristic of the aggregation of tropocollagen molecules is

the presence of cross-linking that contributes to enhance mechanical properties of the MCF such as tensile strength, fracture toughness and viscoelasticity (Misof et al., 1997).

Theoretical and computational models suggest that this natural design of collagen fibrils maximizes the strength and provides large energy dissipation under mechanical deformation. X-ray diffraction techniques have shown that collagen fibrils are preferentially oriented with respect to the predominant stress direction in bone (Burr, 2019). Longitudinally oriented fibrils are found in regions of bone under tension. Conversely, transversely oriented fibrils are representative of zones under compression. Thus, collagen is oriented in directions that are dependent on the mechanical environment (Launey et al., 2010).

The dimensions of the MCF are still under investigation. The diameter is characterized by a wide interval of values, e.g. [50 – 200] nm, depending on the specie, anatomical site and water content. In Table 2.1 a literature survey of the MCF diameter is shown. The MCF length is approximately 1000 nm (Buehler, 2006; Wagermaier et al., 2015), although recent studies based on high resolution tomography have highlighted average lengths around 450 nm (Reznikov et al., 2018).

2.3.2 Apatite mineral

In biological systems apatite occurs as the principal inorganic constituent of normal and pathological calcifications. Several studies have analysed apatite biominerals with different approaches, focusing their attention on crystal structure (Posner et al., 1969), calcium phosphate precursors (Posner et al., 1969), their interaction with the organic matrix (Fielder et al., 2018; Nair et al., 2013) and biomimetic processing-oriented investigations (Nudelman et al., 2013).

Mineral in bone tissue consists of poorly crystalline apatite mineral $Ca_{10}(PO_4)_6(OH)_2$. From a crystal-chemical point of view, apatite is a calcium phosphate characterized by a Ca/P ratio ranging between 1.5 and 1.67. The mineral is largely impure containing constituents such as carbonate, citrate, magnesium, fluoride or strontium incorporated into the crystal lattice (Cowin, 2001). Crystal formation is triggered by collagen or other non-collagenous proteins which act as nucleation centres. After nucleation, the plate-like crystals become elongated but extremely thin (Fratzl et al., 2007, Rho et al., 1998). Bone mineral is based mainly on hydroxyapatite, but it also contains additional elements that replace either the calcium ions or the phosphate or hydroxyl groups; one of the most common such occurrences is the replacement of the phosphate group by carbonate (Fratzl et al., 2007).

Table 2.1. Literature survey of the mineralized collagen fibril (MCF) diameter

Species	Anatomical site	MCF diameter	Reference
Human	Bone	78 – 200 (nm)	Olszta et al. 2007
Human	Bone	100 nm (average value)	Georgiadis et al., 2016
Human	Bone	100 nm (average value)	Nikolov et al. 2008
Human	Bone	Values up to 200 nm	Jäger and Fratzl, 2000
Human	Bone Osteon	46-62 nm	Cassella et al., 1994
Human	Tendon	100-500 nm	Vesentini et al., 2013
Human	Patellar tendon	Up to 200 nm	Svensson et al., 2010
Human	Dentin	80-100 nm	Habelitz et al., 2002
Human	Trabecular	100 nm (average value)	Rubin, 2003
Human	Tibia	100 nm	Xu et al., 2020
Human	Mineralized collagen fibril	200 nm	Yuan et al., 2011
Bovine	Bone	100 - 200 nm	Gupta et al., 2006
Rat	Tendon	Up to 550 nm	Craig et al., 1984
Horse	Tendon	Up to 550 nm	Craig et al., 1984
Guinea Pig	Tendon	Up to 550 nm	Craig et al., 1984
Bovine	Cortical bone	135 ± 40 nm	Li et al., 2013
Rat	Tendon	50 - 200 nm	Wenger et al., 2007
Mouse	Tendon	132 – 200 nm	Derwin et al., 1999
Bovine	Vertebra	50 - 200 nm	Hassenkam et al., 2004
Zebrafish	Bone	145 nm	Cui et al., 2017

2.3.2.1 Mineral shape and size

The characterization of mineral crystals is of fundamental importance for the understanding of bone mineralization. Because of the small size of crystals, considerable efforts have been made to determine the size, shape and orientation of mineral crystals with respect to tropocollagen molecules (Fratzl et al., 1992). The morphology of apatite crystals was mainly investigated by means of Transmission Electron Microscopy (TEM), small-angle X-Ray scattering and atomic force microscopy (AFM). The majority of studies describe apatite minerals as plate-like in shape. However, initial TEM analyses have outlined also a needle-like shape. Several argumentations have been

specified concerning this aspect. The needle like shape could be due to artifacts of the TEM measurements (Fratzl et al., 2004) as well as the prevalence of more needle-like particles in bone tissues of certain species investigated, e.g. horses, mice, rats (Fratzl et al., 1992). Furthermore, a variation of the shape of apatite crystal with aging cannot be excluded (Fratzl et al., 2004).

The concept that apatite platelets are prevalently platelet-shaped is corroborated by the works of Weiner and Price (1986), Weiner and Traub (1986), Traub et al. (1989) Robinson et al. (1952). Furthermore, Eppell et al. (2001), used AFM methods and provide direct evidence that apatite crystals in bone tissue display a plate-like shape. Reznikov et al. (2018) have studied the crystal morphology by means of electron diffraction. Their data outlined that mineral particles can be found both as needle- and platelet- shaped. Recently, Xu et al. (2020) used X-Ray diffraction and revealed that apatite crystals in bone may form small stacks of 2 - 4 platelets, while in areas with higher density, larger stacks of roughly 8 platelets are observed.

The average size of the mineral crystals tends to span a wide range of values. However, from TEM and X-Ray diffractions studies there is a general agreement that the thickness of apatite platelets is in the range 2-5 nm. Conversely, considerable variations in the other two spatial dimensions, i.e. width and length appear to exist. The longitudinal dimension spans between 50 nm and 150 nm while the width can be characterized by values in the interval 7 nm – 80 nm (Rubin et al., 2003).

Several experimental techniques, which include X-ray diffraction, Fourier transform infrared technique, infrared spectrophotometry, small-angle X-ray scattering (SAXS), back scattering electron imaging, solid-state nuclear magnetic resonance, X-ray pole analysis, scanning electron microscopy, TEM and AFM have been used to investigate the morphology of apatite mineral. Each technique requires specific processing of tissue sample and, therefore it is subject to artifacts and different limitations (Rubin et al., 2003; Shahar et al., 2018). Overall, measurements are challenging due to the small size of crystals. In Table 2.2 the different range of values for mineral dimensions are reported.

There is considerable evidence in support to conclusion that biological factors are important in establishing size, shape and orientation of bone crystals. For instance, as bone ages, the apatite crystals may coalesce and form larger aggregates. Thus, the measured size of mineral crystals is dependent also on tissue age (Burr, 2019).

Table 2.2. Literature survey of dimensions of apatite crystals

Species	Anatomical site	Dimensions			Reference
		L (nm)	W (nm)	T (nm)	
Human (healthy male)	Femur Cortical tissue	40 -200	20-70	4.8 ± 0.9	McNally et al., 2012.
Human	Femur Cortical tissue	18.75 - 108.75	5.25 - 93.75	-	Weiner and Price, 1986
Human	Femur Cortical tissue	31.3	8.4	-	Voltolini et al., 2011
Human	Rib cortical tissue	30-45	30-45	2.5-5	Robinson et al., 1952
Human	Vertebra Trabecular tissue	-	-	3.3 ± 0.2	Rinnerthaler et al., 1999
Human	Femur trabecular tissue	57.0 ± 6.7	27.3 ± 3.5	-	Rubin et al., 2003
Human (fetal)	Femur Woven	18-30	10-20	-	Su et al., 2003
Macacques	Rib Cortical tissue	26.3 – 29.7	8.1 – 9.7	-	Voltolini et al., 2011
Bovine	Femur Cortical tissue	24.7	7.8	-	Voltolini et al., 2011
Bovine	Tibia, femur	3 -120	3 -120	< 2	Eppell et al., 2001
Bovine	Tibia, femur Cortical tissue	110 ± 61	72 ± 41	34 ± 29	Tong et al., 2003
Horse	Tendon	15-55	5-25	2-5	Nudelman et al., 2010
Rat	Ulna Tibia	15-75	10-45	2-5	Ziv et al., 1994
Rat	Femur Cortical tissue	33-34.5	15-16	2.6-2.8	Turunen et al., 2016
Turkey	Mineralized tendon	15-150	10-80	2 -5	Rubin et al., 2003
Turkey	Leg Tendon	40-170	30-45	4-6	Landis et al., 1993
Turkey	Tendon	10-100	10-100	2-3	Weiner and Traub 1991

2.3.2.2 Mineral orientation

In recent years, several methods have been used in order to investigate the orientation of apatite within the mineralized collagen fibril. Georgiadis et al. (2015) have provided an exhaustive review concerning the techniques that assess the organization of the mineralized collagen fibril. The authors divided the methods that can examine directly the orientation of bone ultrastructure without providing an image of it from the techniques that offer direct images of bone elements and, thus, orientation-specific information can be derived from post-processing images. For the first category, they considered polarized light microscopy, polarized Raman spectroscopy, polarized Fourier transform infrared spectroscopy, X-Ray diffraction techniques, electron-based techniques. Typically, the imaging-based techniques have a lower field of view than the orientation specific techniques. The most common techniques applied to bone ultrastructure are confocal laser scanning microscopy, second harmonic generation in multi-photon microscopy, X-ray based imaging, electron-based imaging (TEM, SEM) and AFM. These techniques offer also complementary information about the ultrastructure of bone, arrangement of minerals, size and shape of apatite crystals, structural details of collagen apatite interfaces and structural details of bone remodelling sites (Reznikov et al., 2018).

The quantitative assessment of the 3D organization of the ultrastructure is a fundamental objective to the understanding the structure and function of mineralized collagen fibrils. Specifically, from the numerous techniques cited above four methods can provide information about the mineralized collagen fibril, i.e. 3D SAXS, SEM, ptychographic CT and phase contrast nanotomography.

Rinnerthaler et al. (1999) have shown that scanning SAXS is suitable to detect orientation of the nanocomponents of bone tissue. Their investigations highlighted that both collagen and mineral crystals are predominantly aligned parallel to the trabeculae. The same organization is highlighted also by Seidel et al. (2011) and Liebi et al. (2015). They used a 3D SAXS method to reconstruct the orientation of mineral platelets with respect to higher hierarchical level in bone organization, i.e. trabeculae (Liebi et al., 2015) or osteonal bone (Seidel et al., 2011). Georgiadis et al. (2015) have

Table 2.3. Literature survey of the orientation of apatite crystals

Species	Anatomical site	Orientation	Reference
Human (healthy male)	Femur Cortical tissue	Maximum 36° with respect to fibril longitudinal axis	McNally et al., 2012.
Human	Vertebra Trabecular tissue	± 45° with respect to longitudinal direction of trabecula	Rinnerthaler et al., 1999 Jaschouz et al., 2003
Human	Femur Trabecular tissue	± 10° with respect to longitudinal direction of trabecula	Reznikov et al., 2015
Human	Transiliac bone Trabecular tissue	±30° with respect to the collagen long axis	Grünewald et al., 2020
Human	Tibia	±20° with respect to the collagen long axis	Xu et al., 2020
Sheep	Tibia, Femur Trabecular tissue	19°± 14° (tibia) 20° ± 14° (femur) with respect to long axis of osteocyte lacuna	Shah et al., 2016
Turkey	Leg Tendon	±20° with respect to the collagen long axis	Landis et al., 1993

proposed a 3D SAXS method which allows to derive the 3D orientation of bone ultrastructure. They confirmed that the ultrastructure orientation is closely related to the orientation of the trabecular microarchitecture.

Several studies (Landis et al., 1993; Xu et al., 2020) have outlined that the orientation of the crystallographic c-axis of minerals follows the longitudinal axis of collagen fibrils, confirmed also by electron diffraction (McNally et al., 2012). Recent advances in scanning SAXS and WAXS (Wide-angle x-ray scattering) techniques allowed to quantify the inclination range of apatite c-axis with respect to the longitudinal axis of the fibril. Recently, Grünewald et al. (2020) found a variation of the alignment difference across bone sample reaching up to 30 degrees. Experimental evidence and quantitative information of the alignment of apatite crystals along the longitudinal axis of the collagen are provided also by Xu et al. (2020) that identified an angular distribution of ± 20 degrees. In Table 2.3 an overview of the interval of mineral inclinations is given.

2.3.2.3 Mineral-collagen arrangement

AFM and SAXS investigations have shown that the mineral platelets in the mineralized collagen fibril are arranged in a staggered pattern along the longitudinal direction of the collagen fibril, with a periodicity of roughly 67 nm (Jäger et al., 2000). Nonetheless, in the radial direction, indicated also as equatorial plane by Lees et al. (1987), there is no accordance among investigators. Stock et al. (2015) proposed that apatite minerals form a circular pattern in the equatorial plane. Conversely, using combined SAXS and TEM techniques, Burger et al. (2008) indicated that the lateral packing of nanoscale calcium-phosphate crystals in collagen fibrils can be represented by irregular stacks of platelet-shaped crystals intercalated with organic layers of collagen molecules. Finally, Vercher-Martinez et al. (2015) suggested parallel layers in the normal plane to the longitudinal direction.

2.3.2.4 Mineral volume fraction

In the past decades, the mineral content within the MCF has been a matter of investigation. The degree of mineralization reported in literature varies among studies (Table 2.4). Initial investigations of Katz and Li (1973) indicate that the amount of mineral can reach up to 70 percent. Nikolov and Raabe (2008) calculated a maximum mineral volume fraction of 52 percent. Jäger et al. (2000) indicated a value of 42 percent as an average value for the degree of mineralization, in agreement with ash weight measurements of mineral content in bone (Abe et al., 1996). Liu et al. (2013) determined the amount of mineral content by means of steric models. Their results suggested that the maximum mineral content that can be accommodated within the collagen fibril is up to 53 percent. Spiesz et al. (2013) measured MCF mineralization in samples from the human femur using backscattered electron imaging. In bone structural units the mineral content was found in the interval 25 percent – 55 percent with a mean value of 38 percent.

There is a positive correlation between tissue mineralization and stiffness, but also an inverse relation between degree of mineralization and toughness. As the mineral content in bone increases, the tissue becomes stiffer and more brittle. Thus, in this case, the tissue deforms less under load and

Table 2.4. Literature survey of mineral volume fraction

Anatomical site	Techniques	Mineral volume fraction (%)	Reference
Long bone	Estimation from analytical model	50	Currey, 1969
Bone	Estimation from analytical model	Average value 43 Upper limit 56	Jäger and Fratzl, 2000
Bone	Estimation from analytical model	45	Ji and Gao, 2006
Bone	Estimation from analytical model	Lower limit 32 Upper limit 52	Nikolov et al., 2008
Bone	Estimation from analytical model	Upper limit 53	Liu et al. 2012
Bone	Estimation from analytical model	Lower limit 7 Upper limit 30	Vercher-Martinez et al. 2015
Human femur	Backscattered electron imaging	Lower limit 25 Upper limit 55	Spiesz et al. 2013

the cracks will propagate with less energy than in less mineralized bone (Burr, 2019). At the nanostructure level, the tensile strain is distributed through an elongation of collagen fibrils and shear deformation of the mineral matrix. This behaviour protects apatite crystals, that are brittle and increase the load-carrying capacity (Gupta et al., 2006; Gao et al., 2003).

2.3.2.5 Amorphous calcium phosphate layer

Recent studies highlight the existence of a hydrated amorphous layer covering the nanocrystals of apatite. The current view agrees with an additional non apatitic environment encapsulating the apatite mineral in a core-shell structure. Experimental evidence of this hydrated amorphous calcium phosphate layer has been provided by several techniques, such as solid-state nuclear magnetic resonance, infrared spectroscopy, high resolution TEM and diffraction.

The amorphous calcium phosphate layer is a matter of debate. Firstly, the amorphous-to-apatite transformation still needs to be understood. Subsequently, the functionality of the amorphous calcium phosphate domain should be assessed. In the last direction have moved Wang et al. (2013). They show that the amorphous calcium phosphate layer that covers the nanoplatelets is involved in the arrangement of the apatite crystal within the mineralized collagen fibril by orienting them. It was demonstrated that the amorphous calcium phosphate layer has an important structural role. Their results suggest that the amorphous calcium phosphate layer provides a favourable chemical environment for ion exchange and may drive the interaction between mineral platelets.

A comprehensive picture of the amorphous calcium phosphate layer- mineral core interactions is therefore a challenging task to achieve. A NMR spectroscopy based study has highlighted the presence of a disordered surface layer with a thickness estimated to be roughly 10 percent of each linear crystal dimension (Jäger et al., 2006). An absolute value, i.e. 0.8 nm, has been introduced by von Euw et al. (2018) for a platelet thickness of 4 nm, determined with a combination of SS-NMR techniques. Bertolotti et al. (2020) further clarify the issue using a combination of SAXS and synchrotron wide angle X-ray total scattering (WAXTS). The results of SAXS and WAXTS analyses are combined to allocate the amorphous content around the apatite core and provide different models of the coexistence between the amorphous component and the apatite. Overall, the results are consistent with a core-crown like structure, envisioning an alternative spatial interconnection between the apatite core and its amorphous surface layer.

Nonetheless, the role of the apatite core is critical in the manifestation of some phenomena, e.g. crystallization process, interactions with cells and extracellular components. Studies developed on synthetic analogues of biological apatite have outlined that the hydrated layer is relatively instable compared to the apatitic core. Moreover, the apatite domain develops at the expense of the hydrated layer (Combes et al., 2016).

2.3.3 Water

As the third main component of bone nanostructure, water is studied extensively (Cowin, 2001, Lemaire et al., 2015; Marinozzi et al., 2014a; 2014b). Water is responsible for diffusion of nutrients, metabolic exchange and ion transport between different regions of bone and contributes to the overall toughness of bone. Cowin et al. (2001) have indicated that water occupies different porosity levels of bone tissue. It is commonly accepted that bone presents four levels of porosity,

which are nested hierarchically one inside another: collagen-apatite (10 nm), canalicular (100 nm), lacunar (up to 8 μm), vascular (50 μm), and the intertrabecular porosity (up to 1 mm) (Cowin et al., 1999). At the nanoscale porosity, initial studies have indicated that water is present as bound water. Burr (2019) divides the water compartment at the collagen-apatite level into three subcompartments. Loosely bound water is found at the interface of collagen-mineral and contributes to the load transfer between mineral and organic matrix. Tightly bound water is individuated within the tropocollagen molecules and enhance elastic and viscoelastic properties of collagen. Structural water is found between the crystal lattice and plays a role in the aggregation of minerals.

Recent studies have introduced the hypothesis that free water may also exist at the nanostructure level. Marinozzi and co-workers (Marinozzi et al., 2014a; 2014b) performed experimental analysis of diffusion within a single trabecula that led to new insights for bone tissue characterization up to the length scale of its principal constituents, i.e. collagen matrix and apatite mineral. An air-dried single trabecula from human femur head was completely immersed in water. The hygroexpansion of the trabecula sample appeared sensitive essentially to the water transport at the collagen – apatite length scale.

In the same direction focused the attention Lemaire et al. (2015) in a molecular dynamics study that investigates a possible flow within the collagen – apatite network. Their results show that water diffusivity is pore-size dependent, decreasing with pore dimension. Flow of water was observed also when the confinement effect is significant, i.e. for a condition characterized by small pore size, e.g. 2 nm.

2.3.4 Non-collagenous protein

The non-collagenous protein (NCP) constitutes the remaining 10 percent of the organic phase in bone nanostructure. Proteoglycans and proteins like osteopontin, osteocalcin, osteonectin, phosphoproteins, bone sialoproteins are thought to play crucial roles in bone formation. The NCPs control mineral crystal nucleation and also regulate its growth, size, orientation and morphology. In addition, NCPs may allow the relative sliding of mineral crystals and play an important role in plasticity, toughening and energy dissipation of bone. However, little information is known about the precise locations and specific functions of each NCP (Reznikov et al., 2014).

2.4 Models of the mineralized collagen fibril

The MCF is the primary building block of bone structure and its architecture, physical and mechanical characteristics are essential for determining structure – property relations and understanding bone behaviour. To investigate the nanostructure of bone experimental studies, e.g. X-ray diffraction (Jaschouz et al., 2003) or micro-mechanical devices (Eppell et al., 2001) have been used. In addition, a fundamental understanding of bone properties may be achieved by employing computational techniques to analyse bone properties at nanoscale. In this section a survey of the existing models proposed in literature is provided. In previous reviews of Hamed et al. (2012) and Sabet et al. (2015), computational models have been classified as mechanical models (Jäger et al. 2000), computational models using Finite element method (FEM) (Liu et al., 2012; Hambli et al., 2012, Yuan et al., 2011) and molecular dynamics models (Buehler et al., 2006; Fielder, 2018, Nair et al., 2013). The main objective of the aforementioned studies is understanding the deformation mechanism and the mechanical properties of bone at nanoscale.

2.4.1 Mechanical models

Hodge and Petruska (1963) proposed from observation in the electron microscope by negative contrast method a quarter-stagger array of tropocollagen molecules. They observed an end-to-end overlap of roughly $0.4 \cdot D_{period}$ length. It follows that in the hydrated structure of tropocollagen molecules there should be holes of about $0.6 \cdot D_{period}$ length. The authors assumed that the holes are contiguous and aligned to form transverse channels and extend for unknown distance across the fibril. Good evidence was found for this hypothesis, as confirmed by Yamauchi et al. (1989). The presence of holes has important implications in relation to mineralization. The quarter stagger packing allows the development in the hole region of appropriate conditions for the nucleation of crystallites (Glimcher 1959). Thus, the nucleation groups occur at or near the ends of tropocollagen molecules together with others brought into proximity with the former as a result of the quarter-stagger packing arrangement of tropocollagen.

Wagner and Weiner (1998) focused on translating Hodge and Petruska 2D model into three dimensions, and then figuring out how the crystals are organized with respect to the collagen

framework. In Weiner and Traub (1992), the authors demonstrate the platelet-like geometry and provided a structural model of the mineralized collagen fibril. In fact, based on TEM observation (Weiner et al., 1991), a major part of crystals is found within collagen fibrils. In an imaginary plane parallel to the long axis of tropocollagen molecules, the latter are all parallel with their ends separated by holes. The neighbouring tropocollagen molecules are staggered in the longitudinal direction by the D_{period} of roughly 67 nm. In the equatorial plane, i.e. orthogonal to the longitudinal axis, no offset is present and the tropocollagen molecules are aligned as well as holes. The alignment of holes form channels where apatite platelets are present (Weiner et al., 1992; 1998).

Landis and co-workers had developed a model based on the 3-D TEM tomography (Landis et al., 1993). The irregular shaped mineral nanocrystals grow preferentially in length along the collagen long axes. Minerals may extend to different lengths over various zones of the fibril and some crystals appear to extend over adjacent gap and overlap zones. They individuated mineral lengths in the range from 40 to 170 nm, and width in the interval from 30 to 45 nm. Conversely, the thickness of the mineral apatite was found very uniform of approximately 4-6 nm. It was also observed that minerals lie nearly parallel (within ±20°) to one another and to the collagen long axis. The authors provided an illustration of the MCF with the intent to demonstrate shape, size, location, alignment and orientation of mineral in the collagen layers. The collagen model follows the model proposed by Hodge and Petruska. When packing the collagen molecules in three dimensions the hole and overlap zones are aligned thereby creating extensive channels throughout the assemblage. Irregularly shaped, large and small minerals are first accommodated in the gap zones and subsequently in the overlap regions, with preferential growth along the c-axis following the direction of the collagen longitudinal axis. In a study on mineral crystals in embryonic chick bones, Landis et al. (1993) suggested that the mineral sheets may fuse to form a continuous mineral organization.

Jäger and Fratzl (2000) have also developed a model of a staggered arrangement of mineral platelets in the collagen matrix to form the mineralized collagen fibril. The authors based their model on the Hodge and Petruska scheme (Hodge and Petruska, 1969). They attempt to accommodate mineral platelets within the collagen fibril by taking into account a series of constraints concerning the hydration aspect of collagen molecules. Based on Lees (1987) observation, the lateral spacing of collagen molecules decreases on drying and mineralization. The Authors calculated an average volume fraction of mineral of roughly 0.43, while the upper limit is assessed to be around 0.56. They proposed several possible models for the deposition of bone minerals. Whether the minerals are considered only in the gap regions or in the overlap regions, the volume fractions that are created result greater that the possible values calculated according to the steric constraints observed from

TEM, X-ray or neuron scattering techniques. Thus, they proposed a configuration where the crystals are arranged longitudinally in a staggered manner with a periodic length of 67 nm.

As outlined by Cowin (2001), bone at the nanoscale is a two-phase composite. Models that study the elastic properties of the ensemble organic and inorganic constituents have been developed. In several models (Gao et al., 2003; Gupta et al., 2005) the rule of mixture has been applied in order to analyse mechanical properties of the nanocomposite. In an early attempt, Currey (1969) has assumed that mineral crystals fuse end-to-end and form mineral fibers that reinforce the collagen matrix. To estimate the modulus of elasticity, the superposition of the two constituents has been considered. These assumptions lead to a good estimation of the longitudinal elastic modulus, while the transverse modulus was minor than the modulus achieved from experimental evidence (Currey, 1969).

Gao and colleagues (Gao et al., 2003) used the arrangement proposed by Jäger and Fratzl in order to investigate the mechanical behaviour of bone at nanoscale. The authors considered that under an applied tensile stress the apatite minerals carry the tensile load while the collagen matrix transfers the load between apatite crystals via shear. They suggested that below a critical length scale, the brittle mineral apatite becomes insensitive to crack like flaws. Their study outlined that the critical length scale for apatite is in the order of few nanometers. They also investigated stiffness, toughness and strength of the structure in order to further investigate the methods of optimization designed by nature. They showed influence of the size and geometry of apatite minerals on the strength.

Wang and Qian (2006) developed a two-dimensional shear-lag model to predict stress concentration around an initial crack in mineral collagen matrix. In this study the initial crack is assumed to exist in the mineral phase which is sandwiched between two collagen layers. They provided qualitative information for predicting the relationship between spatial and material properties of bone components and crack development. They reported that the stress pattern depends on the mechanical properties of collagen and apatite and could determine coalescence and scattering of nano cracks around the initial crack.

In conclusion, these studies provided remarkable insights into material properties and fracture behaviour of bone at the nanoscale. However, the mechanical models proposed an idealised two-dimensional model of the collagen – mineral nanocomposite, avoiding therefore to tackle with the 3D arrangement of collagen molecules and apatite crystals. Subsequently, computational models were developed in order to overcome part of the limitations emerged with the mechanical models. Computational models represent a powerful and versatile approach to successfully analyse complex

geometries and material properties constitutive laws. It is worth pointing out that despite the remarkable advances in technology, there still remains open issues that implicitly lead to limitations also for computational models, e.g. arrangement of mineral within the collagen fibril, the dimensions and characteristics of apatite crystals.

2.4.2 Finite element models

Finite element models have been investigating the mechanical behaviour of the mineral collagen nanocomposite. The model proposed by Jäger and Fratzl have been in most of the cases the starting point for further analysis using FE methods to assess the mechanical behaviour of bone at nanoscale. For instance, Siegmund et al. (2010) used FEM model to study the influence of collagen cross-linking on the stiffness of the MCF. They considered two types of cross-links, enzymatic and non-enzymatic, and showed that the latter increase stiffness and decrease toughness of bone, while the former has only minimal effects on the mechanical properties of MCF.

Barkaoui and colleagues (Hambli et al., 2011; Barkaoui et al., 2015; 2016) developed a 3D nanoscale model of the MCF and investigate by means of Finite Element method the effect of material and structural factors, i.e. collagen cross-links, on the fracture behaviour. They considered a periodic repetitive region of five tropocollagen molecules (composing a microfibril) which are offset in the longitudinal direction one another with periodicity of 67 nm. The tropocollagen molecules are embedded into a homogeneous mineral matrix. Their outcomes indicate that the number of cross-links, the mineral density and the Young's modulus of the mineral phase have noticeable influence on the strength of the MCF.

Recently, Barkaoui et al. (2016) estimated the elastic properties of bone at the nanoscale, individuating three hierarchical levels at this length scale. Namely, they considered three different repetitive structural units: at the first level, i.e. mineralized collagen microfibril, collagen molecules are arranged in a pentameric structure where mineral crystals grow in specific sites. The second scale level is determined by the mineralized collagen fibril composed of an organization of inter-digitating microfibrils. The third level is constituted by the mineralized collagen fibre which is formed by the binding of fibrils. The elastic properties are estimated by a combination of neural networks computations and finite element models. Their results were accordingly with values present in Literature and, therefore, highlighted that the novel computational method allows to deal with good accuracy a complex multiscale problem.

Vercher et al. (2014) provide estimation of the 3D stiffness matrices and elastic constants at the mineralized collagen fibril scale using FE methods. The model is based on a unit cell of the MCF, composed of a collagen matrix and apatite minerals arranged in a staggered manner in the axial direction of the fibril and in parallel layers in transverse direction. The minerals are assumed to be embedded in the collagen matrix. In Vercher Martinez et al. (2015), the authors enhanced their 3D geometrical model. They considered several degrees of mineralization allowing the development of mineral platelets in axial and transverse direction, through the variation of the lateral space between platelets. They highlighted that the platelets interdistance as well as the mineral overlapping is crucial for the mechanical behaviour of the MCF.

Yuan et al. (2010) investigate the relationship between elastic properties and structure of a MCF model. They developed detailed 2D and 3D FE models and compared the outcomes with experimental data obtained by synchrotron X-ray diffraction. The model of the nanocrystal-reinforced composite follows the staggered pattern in the axial direction suggested by Jäger and Fratzl (2000). Several representative volume elements have been investigated by varying the distances between neighbouring platelets. In the radial direction of the fibril, they considered a concentric arrangement of mineral platelets. Besides, the collagen matrix is represented as a continuous phase. It should be noticed that the work of Yuan et al. (2010) provides a discussion concerning the water effect within the MCF. They simplify their model by assuming that water phase and collagen phase are combined together into a single matrix collagen phase and the Young's modulus of this phase is taken as that of wet collagen matrix. They highlight that the bound water within the MCF may have structural functions while the free water at this length scale may migrate and change its distribution within the MCF, consequently introducing non-uniform properties into the collagen phase.

Liu et al. (2013) applied new nanostructural information concerning apatite arrangement in the collagen fibril to estimate the mechanical behaviour of partially mineralized tissue and to interpret how the effective connection of tendon to bone occurs. They considered different sequences of mineralization, to evaluate the arrangement patterns proposed in Literature, ranging from nucleation in gap regions, as it occurs during bone development up to nucleation initiating outside the fibril, as it occurs along the insertion. They quantified how the combination of intrafibrillar and extrafibrillar apatite stiffens the collagen and how the sequence of mineralization affects the mechanical behaviour. Models began with unmineralized collagen fibrils, followed by prescribed apatite accumulation into gap regions, onto the exterior of collagen fibrils and within overlap regions. They used these models to generate bounds for the fibril Young's modulus. These constraints were then applied to estimates the mechanical behaviour of collagen fibres. The FEM analysis was subsequently developed on a

rectangular section containing a hexagonal array of fibrils. The sequences of mineralization most frequently suggested in literature may allow to develop a collagen nanostructure optimized to arrange mineral crystals in such manner to minimize stiffening.

In the works of Bar-On et al. (2011; 2013; 2018), the structure of the MCF includes layers of apatite platelets and collagen molecules in which two adjacent layers are axially staggered by 67 nm (Landis et al, 1993; Jäger et al., 2000). In low-mineralized fibrils the platelets are short and non-overlapping, but these become longer and overlapping as the mineral content of the fibril increases. During mineralization, the axial spacing between the fibrils is filled by mineral nano-platelets, which gradually spread outside – coating the molecules themselves. The MCF structure is simplified here by considering a staggered array of apatite platelets embedded in a homogeneous collagen matrix, ignoring therefore, the molecular structure. Variations in the stiffness of staggered biological arrays were analysed as a function of mineral structural properties. The degree of overlapping between the platelets is found to significantly affect the stiffness of the array.

The several FEM studies investigate the elastic behaviour of the MCF. It should be noticed that different structural arrangements have been taken into account. Namely, several models have considered collagen array of aligned long cylinders embedded in a mineral foam representing the inorganic phase. Conversely, other models have focused on a network of apatite platelets embedded in a collagenous foam. To date, FEM models that implemented the matrix of staggered platelets embedded in an array of staggered tropocollagen molecules has not been developed yet.

2.4.3 Molecular dynamics studies

Several atomistic level simulations have studied the deformation mechanism of the collagen molecules, as well as collagen-mineral systems using molecular dynamics simulations. Buehler and co-workers (Buehler et al., 2008) modelled, firstly tropocollagen molecules using atomistic simulations and linked chemical properties of individual tropocollagen molecules to the mechanical response of the fibrils. To understand mechanics of collagen, the interplay between the staggered arrangement of tropocollagen fibrils and the intermolecular chemical interactions has to be considered. Successive studies (Depalle et al., 2016) have taken into account also the mineral phase within the collagen fibril. The authors developed a model of the MCF conserving the 3D structure and entanglement of the molecules. They investigated the deformation mechanism that govern the

mechanical behaviour of MCF under large deformations. They explored several values of mineral content within the MCF and found that MCF reaches its optimal properties in terms of toughness and strength for a mineral density around 30 percent.

Nair et al. (2013) performed atomistic simulations of a 3D molecular structure of the mineralized collagen fibril. They investigated the mechanical properties and fracture resistance under tensile loading at various mineral densities.

Dubey et al. (2009) analysed the interfacial interactions between idealized tropocollagen molecules and minerals of apatite. Different arrangements of tropocollagen molecules and apatite, i.e. tropocollagen molecules either parallel or perpendicular to the surface of apatite minerals have been considered in the 3D molecular dynamics simulations. Furthermore, they analysed different scenarios related to the absence and presence of water at this structural level. Their analyses point out that a hydrated environment optimizes the mechanical strength in the nanoscale structural configuration of apatite and collagen.

Furthermore, Fielder and Nair (2018) expand the characterization of the mechanical properties of the mineralized collagen fibril by introducing the effects of variation and distribution of water and mineral content in fibril gap and overlap regions. The authors used the model proposed by Jäger and Fratzl (2000). Therefore, they investigate how the deformation mechanism is influenced by different mineralization and hydration levels. Their results indicate that an increase of the water content leads to a decrement of Young's modulus of the mineralized collagen fibril.

These studies investigate the interface between organic and inorganic components of the mineralized collagen fibril. They represent an attempt to overcome coarse grained models that simplified the structure of bone and failed to capture atomic scale mechanisms. These models considered the geometric characteristics of the MCF, driven by the concept that mineralization occurs in the gap regions of the collagen fibril. However, also molecular dynamics studies present some limitations. For instance, the models reported in this survey did not consider electrostatic interactions among the principal components of the MCF. Another observation to be highlighted is the high computational cost of molecular dynamics studies that impedes to extend this method to higher structural scale. For the moment, molecular dynamics was applied to repetitive unit cells of collagen – apatite matrix.

A review of representative models of bone at nanoscale was presented in this section. Different studies have considered idealized models of nanostructure. In conclusion, computational methods investigated the mechanical properties of bone at the nanoscale in function of the mineral volume

fraction, collagen-apatite arrangement and the presence of further complexities of the structure, e.g. water molecules, collagen cross-linking. It is worth pointing out that the arrangement and the size of apatite platelets is still an open issue, which makes extremely challenging to implement the appropriate features in computational models. It was highlighted that more experimental studies are required to elucidate aspects of apatite – collagen arrangement and their interactions. New insights may be used to validate the already developed studies and to create more accurate new 3D models of bone nanostructure.

CHAPTER 3

3D Model of Water Diffusion within the Human Mineralized Collagen Fibril

Bone tissue at nanoscale is a composite mainly made of apatite crystals, collagen molecules and water. This work is aimed to study the diffusion within bone nanostructure by means of Monte-Carlo simulations. To this purpose, an idealized geometric model of the apatite-collagen structure was developed. Due to the small dimensions of apatite crystals, literature presented mostly qualitative studies concerning the mineral inclination with respect to the microstructure, i.e. single trabecula. In this study, an assessment of the influence of platelets orientation on the diffusion coefficient of water is performed. To represent the hindrance of the impermeable apatite crystals on the water diffusion process, the diffusion coefficient was scaled with the tortuosity, the constrictivity and the porosity factors of the structure. The diffusion phenomenon was investigated in the three main directions of the single trabecula and the results highlight an anisotropic medium at the nanoscale. A good agreement with previous experimental results computed by means of a genetic algorithm was found.

The contents of this Chapter are extended from the following publications:

- Bini F., **Pica A.**, Marinozzi A., Marinozzi F. A 3D Model of the effect of tortuosity and constrictivity on the diffusion in mineralized collagen fibril. Scientific Reports vol. 9: 1, Article number 2658 (2019)
- Bini F., **Pica A.**, Marinozzi A., Marinozzi F. 3D Model of Diffusion within the Collagen-Apatite Porosity: an insight to the Nanostructure of Human Trabecular Bone Tissue. PLoS ONE 12(12): e0189041 (2017)

3.1 INTRODUCTION

3.1.1 State of art of water diffusion studies within the mineralized collagen fibril

Fluid flow is essential for bone vitality. Fundamental requisites of any living tissue are an adequate supply of nutrients for anabolic activity and a mechanism for removal of waste products resulting from catabolic activities. In particular, for bone tissue, molecular transport is necessary to be ensured in order to maintain an adequate supply of growth factors, mineral ions and other solutes employed in the mechanisms of remodelling, adaptation and repair. In bone, the metabolic traffic and interchange of signalling molecules, physiological solutes and fluids are strongly dependent on the transport pathways comprising, at the smallest hierarchical structural level, the interconnected pores within the apatite – collagen matrix (Cowin, 2001). The role of the fluid phase in bone tissue has been thoroughly analysed, especially at the lacunar-canalicular porosity levels (Cowin et al., 1999; Fritton et al., 2009; Cardoso et al., 2013). Nonetheless, relatively little is known about the properties of the spaces and channel walls through which fluid flows at the nanoscale level of bone tissue. Despite the paucity of experimental information, some studies have postulated the mechanism of flow, its role in physiological processes and in the context of bone processes of growth, remodelling and adaptation.

As the third major component of bone, water has been studied extensively. Water can be found in bound or free states (Cowin, 2001). In fact, the water in the collagen matrix was classified in 5 regimes characterized by increasing water concentration: from 0-0.010 g/g in Regime I to concentration higher than 0.5 g/g in Regime V. Regimes I and II identifies hydrogen bound water forming bridges within the tropocollagen molecules. Bound water has important functions at the structural level of both collagen matrix and apatite mineral (Burr, 2019). Regime V is characterized by free water between tropocollagen molecules. During collagen mineralization, water of Regime V is substituted by apatite crystals (Lees et al., 1989).

Several studies have postulated that at the nanoscale level, the water is bound to ionic crystals (Fernandez-Seara et al., 2005; Cardoso et al., 2013) and has an important function in structuring and orienting apatite minerals (Wilson et al., 2006; Wang et al., 2013). Moreover, bound water in the collagen network is determinant for the viscoelasticity of the organic matrix (Buehler et al., 2008).

Conversely, the free water at this length scale is often omitted in bone fluid flow investigations (Cowin et al., 2001). Overall, a small amount of studies investigated the water

dynamics in bone matrix. In the work of Fernandez-Seara et al., (2002), water diffusion in the mineralized matrix of bone was studied by proton nuclear magnetic resonance spectroscopy and imaging by measuring the diffusion fluxes of tissue water in cortical bone specimens of rabbit tibiae. Water distribution in human cortical bone was measured by means of nuclear magnetic resonance in the study of Ni et al. (2006).

Marinozzi and co-workers (Marinozzi et al. 2014a; 2014b) investigated experimentally water diffusion within human trabecular bone specimen that has led to new insights for bone tissue characterization up to the length scale of its principal components, i.e. collagen and apatite mineral. Their studies were based on the measurement of hygroexpansion of a single dehydrated trabecula from human femur head consequent to water sorption. The trabeculae were obtained from specimens of cancellous bone with moderate coxo-arthritis. Subsequently each air-dried single trabecula was completely immersed in water and the displacements along the three main axes (Length L, Width W and Thickness T) of the plate-like trabecula were measured by means of a high accuracy dilatometer. Analysis of the swelling over time along the three main axes of the plate - like trabecula allowed to achieve information about the water diffusion from external surfaces to the internal structure of the specimen.

Subsequently, a 3D analytical model (Marinozzi et al. 2014b) of the water uptake was developed and it was used to predict the diffusion coefficients along the three axes of plate-like trabeculae (Length L, Width W and Thickness T) by means of a genetic algorithm. Three different values of the diffusion coefficient along the main axes of a human trabecula were obtained i.e., [$D_L = 1.03 \cdot 10^{-9}$, $D_W = 1.26 \cdot 10^{-10}$, $D_T = 1.16 \cdot 10^{-11}$ ($m^2 \cdot s^{-1}$)]. The major diffusivity was in the longitudinal direction, while minor values, with one and two orders of magnitude than D_L, corresponded to D_W and respectively D_T.

In addition to experimental studies, the computational model of Lemaire et al. (2015) should be mentioned. The authors investigated by means of molecular dynamics simulations the possibility to obtain a fluid flow at bone nanoscale. Their main results indicate at the level of porosity corresponding to the collagen - apatite matrix that there are suitable conditions for the presence of free water.

3.1.2 State of art of diffusion coefficient assessment methods

The application of porous media theories to biological tissues has led to significant advances in the analysis of the structural characteristics of the medium (Marinozzi et al., 2011; 2014b; Pham et al., 2015) and in the investigation of physiological processes, e.g. intercellular signaling (Gatti et al., 2017), diffusion of nutrients.

Transport properties through composite media depend on the arrangement of their constituents, shape and inclination. The diffusion coefficient within a porous medium takes into account the decrease of the volume available to fluid transport due to the presence of the impermeable medium and, therefore, it is lower than the corresponding diffusivity in a homogenous medium.

General relations describing the dependence of transport properties, e.g. diffusion coefficient, on the structural features of the media are widely studied in literature. Predictions of the effective diffusivity in function of the structural nature of porous media were developed in the fields of chemistry, geological sciences, engineering and physics for a wide range of important applications: catalysis, separation and filtration, cement chemistry, oil recovery and migration of soil pollutants. For any of these processes there is a need to predict the effect of the structure topology on the fluid flow. The approaches implemented in these sectors has been subsequently applied also in the biological field to investigate the diffusion process in soft tissues like brain (Hrabe et al. 2004; Nicholson, 2001; Meriaux et al., 2018), muscles (Carneiro et al., 2018) or in hard mineralized tissues (Lemaire et al., 2015). Different processes involve diffusion of substances through a heterogenous biological medium, such as intracellular signalling, volume transmission and drug delivery (Nicholson et al., 2000).

Overall, the assessment of the diffusion coefficient can be based on empirical correlations with pore structure or on theoretical models with idealized geometry. According to the study of Van Brakel et al. (1974) the influence of the structure is taken into account by means of three factors: the void space inside the porous medium, i.e. porosity, the path length that the particle has to travel in order to cross the medium, i.e. tortuosity, and the reduction of the effective flow due to the changes on the cross section of the pores, i.e. constrictivity.

Although standard methods, such as gas adsorption, mercury porosimetry or inverse size chromatography, have been already developed for information about porosity and surface area, there is a need to define parameters that describe the complexity of most porous networks.

The tortuous factor (τ) is a quantitative measure of the reduction of diffusive flux caused by the sinuous path imposed by the obstacles compared to the straightest path in an unrestricted medium, in the direction of the flow (Ghanbarian et al., 2012). The complex nature of porous medium creates difficulties in order to quantify the tortuosity. Different approaches for estimating this geometric factor have been developed: diffusion experiments (Marinozzi et al., 2014a), ultrasonic reflectivity methods (Moussatov et al., 2001), NMR measurements (Rottreau et al., 2017), analytical models (Matyka et al., 2008; Yun et al., 2006; Stenzel et al., 2016) or 3D image analysis (Wu et al., 2006). Unfortunately, it has been proved very challenging to establish any straightforward relation between the structure of the porous network and the coefficients of the diffusion process. The principal difficulty is that although the existence of tortuosity and constrictivity factors in the assessment of diffusivity is recognized, any direct, general method to extract them from experimental investigations was not provided.

Therefore, numerical models have been implemented to obtain a more explicit expression for geometric tortuosity. Overall, there are two methods for the calculation of geometric tortuosity presented in literature. An approach is based on the development of a model that reproduces in a detailed manner a region of the porous structure and then attempts to determine how this model will contribute to the increment of the local path length of the diffusing particle when compared with a homogeneous medium. Different paths are implemented with the aim to achieve a mean value of tortuosity (Yun et al., 2005). A second method tries to avoid the problems of implementing single paths by mimicking the diffusion process itself, e.g. random walk approach (Jin et al., 2008).

The first models concerning tortuosity factor are based on highly idealized structure of porous medium. The models are developed as a bundle of sinuous parallel capillaries (Epstein 1988) with pores of constant cross section distributed along the bonds of regular lattice (Friedman and Seaton, 1995). Hrabe et al., (2004) highlighted the difficulty to assess the effect of various local geometries on the diffusion process. They developed a geometrical model of the extracellular space of the brain and determined firstly the tortuosity by means of a volume averaging procedure and subsequently the diffusion in this complex environment. Nicholson et al. (2000) applied the homogenization theory on a 2D lattice model that represents repeating obstacles in the form of cellular elements. The diffusion takes into account the tortuosity factor, defined in a geometric manner. Matyka et al. (2008) proposed a tortuosity-porosity relationship using a model characterized by overlapping squares that attempt to mimic the porous medium. Randomly packed spherical particles were used by Sobieski et al. (2012) to determine the tortuosity applying discrete element method.

As a concluding remark concerning tortuosity, in the scenario of anisotropic organization of components, the tortuosity is influenced by shape, arrangement and inclinations of the obstacles.

The constrictivity (δ) is a dimensionless factor and it assesses the impact of the variation of pores cross section on the mass transport (Van Brakel et al., 1974). It becomes important only if the size of the solute is comparable to the dimensions of the pores (Boving et al., 2001). It contributes to a transport resistance and is inverse proportional to the cross section of the bottleneck. In the past there was no technique to determine directly the constrictivity factor from the random porous network. Analytical expressions for the bottleneck effect were developed, mostly for simple geometries. In his study, Petersen (1958) analysed the quantitative effect of periodic pore constrictions on the effective diffusivity. The model accounted is a hyperbola of revolution giving a periodic pore constriction along the pore length. Postulating pore constrictions, Petersen (1958) achieved a more reliable explanation of the reduced values of the diffusion coefficient with respect to the diffusivity in a homogenous medium than attempting to attribute them to the tortuosity factor alone (Petersen, 1958). It should be mentioned that Michaels (1959) calculated the diffusion coefficient modelling the porous medium as parallel capillaries and thus, taking into account the variation of the pore cross section. Its model with regular cross sections of the pores found a good agreement also with the solution proposed by Petersen (1958).

It still represents a challenging objective to experimentally assess the constrictivity factor. The most frequent method relies on mercury intrusion porosimetry (Takahashi et al. 2009; Fu et al., 2015; Wigger et al., 2018). The classical mercury intrusion porosimetry obtained the constrictivity by measuring the differential pore volume, which is filled with mercury for an incremental increase of intrusion pressure. This technique is subject to measurements artifacts since during migration of mercury through the pore paths, the bulges of large pores are filled after passing through narrow pores. As illustrated by Munch and Holzer (2008) this effect is suppressed in simulation of mercury intrusion porosimetry and continuous pore size distribution methods which are implemented on 3D imaging data of the porous network. In fact, nowadays, the improvements in 3D imaging, e.g. nanotomography, X-ray tomography, and image analysis, i.e. graph analysis, transport simulations, may allow to quantitatively describe the constrictivity of the microstructure of porous medium. The efforts carried out in this direction (Munch et al., 2008; Holzer et al., 2013) were able to provide information at the micro-scale level, but methodologies concerning an experimental assessment of constrictivity for nanoporous media have not been mentioned. Furthermore, image analysis on bone tissue which could provide a quantification of the topological features, i.e. tortuosity and the constrictivity, directly from tomographic 3D reconstruction is still absent.

3.1.3. Introduction to Monte Carlo Technique

Information concerning bone nanostructure are achieved from experimental measurements, that become challenging at this length scale and from numerical studies, that complement the experimental knowledge. In this study, the Monte Carlo technique is adopted to determine the diffusion coefficient of water assuming a variation of the geometrical features of the MCF unit cell, i.e. size and orientation of apatite platelets.

Monte Carlo methods form the largest and most important class of simulation techniques that are applied successfully to solve a vast number of scientific problems. The algorithms developed with this method allow to obtain numerical results based on random sampling of variables. Monte Carlo methods start with the generation of a large pool of potential values of the parameters of interest. The parameter values can be obtained by characterizing the experiment in a probabilistic manner, generating a set of random realizations and averaging over the outputs in order to achieve an estimation of the desired quantity.

The origin of the Monte Carlo method can be associated with Buffon's experiment to calculate the value of π (Leclerc, 1733). In the last decades of the nineteenth century several scientists attempted to generate random numbers to verify complicated statistical procedures. Another statistical simulation procedure that it is worth mentioning is the one developed by Gosset ("Student") where he investigated the distribution of the t-statistic. However, the formulation of the Monte Carlo method as it is known nowadays is attributed to von Neumann, Ulam and Metropolis (Metropolis et al., 1949) in the 1940s. They implemented the method to solve neutron diffusion through computer-based statistical sampling (Luengo et al., 2020). The novel contribution of von Neumann and Ulam was to suggest that certain mathematical problems could be treated by finding a probabilistic analogue which is then solved by a stochastic sampling experiment. The sampling experiments involve the generation of random numbers followed by a limited number of mathematical operations which are often the same at each step (Allen, 1989).

The literature on Monte Carlo methods is vast and few examples are indicated in the next lines, with the intent to illustrate the potentiality of the method, rather than trying to provide an exhaustive review. Monte Carlo algorithms were used to obtain approximate solutions for optimization and numerical integration problems, to determine equilibrium properties of a system, particle filters for tracking applications (Dant et al., 2013; Carles et al., 2019). Monte Carlo algorithms were applied also to wireless communication, signal processing, parameter estimation and model

selection. In particular, Monte Carlo framework is used to sample parameter values for simulation experiments. One of the most important aspects of numerical simulation concerns the computational demand, especially when the number of parameters increases. Using Monte Carlo method to sample parameter values, rather than iterate through their values exhaustively allow to make feasible simulations of complex systems (Leigh et al., 2015).

Monte Carlo methods are simulation-based techniques that are extensively used nowadays to perform approximate estimations when analytical estimators cannot be computed, as it happens in many real-world applications. The basic building blocks of Monte Carlo techniques are the Metropolis algorithm and the Gibbs sampler. The Metropolis algorithm consists in drawing the particle configurations uniformly at random and allow the generation of a new configuration of the system if an acceptance rule is verified. The Gibbs sampler considers an arbitrary selection of parameters (indices) to be sampled and uses all the drawn samples to compute the approximate estimator of the quantity of interest. The study presented in this Chapter uses the Gibbs sampler approach. More complex algorithms using Monte Carlo methods have been developed, e.g. data augmentation algorithm, slice sampling, adaptive Markov Chain Monte Carlo, importance sampling. A comprehensive review of Monte Carlo methods was developed by Luengo et al., (2020).

Monte Carlo methods are based on random numbers and the development of random number generators is also a challenging task. The random extractions performed in this study are achieved with a random number generator that applies cellular automata to generate high-quality random numbers that passes stringent random tests (Mathematica 10, Wolfram, Oxfordshire, UK). This generator uses a particular five-neighbour rule, so each new cell depends on five nonadjacent cells from the previous step. For a given cellular automaton, an element (or cell) at a given position in the new state vector is determined by neighbouring cells of that cell in the old state vector. A subset of cells in the state vectors is then output as random bits from which the pseudorandom numbers are generated.

3.1.4 Aim of the study

The study presented in this Chapter is intended to achieve information about the dynamics of fluid transport within the collagen-apatite porosity. The work aims to create a bridge between the diffusion studies at the molecular level (Lemaire et al., 2015) and the lacunar - canalicular scale (Cowin et al., 1999). The main scope is to develop a 3D geometric model of bone nanostructure and to analyse in detail the influence of the apatite arrangement, and also the effect of tortuosity and constrictivity on the mass transport properties at the nanoscale. The analytical model is applied to an idealized geometry of the MCF building block (Hodge and Petruska, 1963; Jäger et al., 2000).

The geometrical parameters associated with apatite mineral organization are set in order to analyse four different mineralization percentage: low (7 percent), lower intermediate (32 percent), upper intermediate (42 percent) and high (52 percent) according to Vercher-Martinez et al. (2015), Jäger et al. (2000) and Nikolov et al. (2008) respectively.

In this manner a prediction of the water effective diffusivity at the MCF nanoscale level is provided. The results are then compared with the available data obtained from the genetic algorithm developed by Marinozzi et al. (2014b).

3.2 METHODS

3.2.1 Geometric model

A 3-D model of the embedded apatite crystals within the collagen fibril has been developed in CAD environment (Autodesk AutoCAD 2016, San Rafael, CA) according to the model proposed by Hodge et al. (1963) and Jäger et al. (2000). Given the periodicity of the collagen-apatite matrix, the analysis is based on a 3-D unit cell of the MCF, which components are represented as follows (Figure 3.1):

(a) Collagen: Type I collagen molecules self-assemble into triple helical tropocollagen molecules, which are approximated by cylinders with 300 nm length. According to the experimental observations of Lees et al. (1987), it was made the hypothesis that

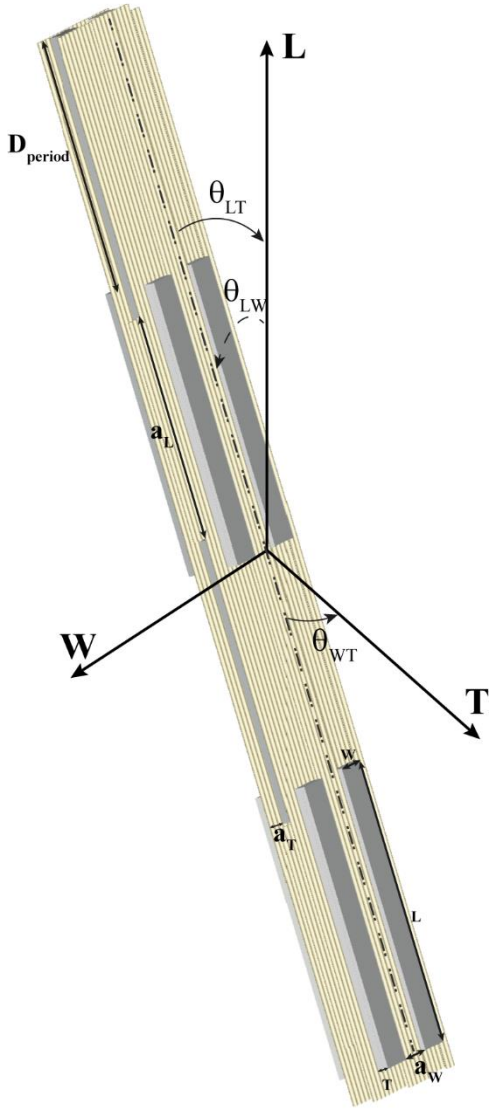

Figure 3.1: Schematic representation of the mineralized collagen fibril composed of tropocollagen molecules (light yellow region) and apatite platelets (grey region). Four unit cells of bone nanostructure are illustrated in order to represent the spatial arrangement of the apatite mineral embedded in the organic matrix of collagen. Each unit cell is constituted by three apatite platelets disposed in a staggered configuration in the longitudinal direction. The inclination of mineral with respect to the longitudinal axis **L** is identified by the angle θ_{LT} in the LT plane, and by θ_{LW} in the LW plane. In the WT plane, the inclination, θ_{WT}, is considered with respect to the width axis **W**. There are also indicated the variables that characterize the geometric parameters of the platelet (L, W, T) the distance between the platelets (a_L, a_W and a_T) and the period length (D_{period}) between adjacent mineral platelets in the longitudinal direction.

the collagen diameter (d) may be characterized by values spanning from 1.1 nm to 1.4 nm, while the distance between adjacent fibrils (a_c) is in the range from 1 to 1.5 nm (Fratzl et al., 2004). Adjacent collagen molecules are staggered in the longitudinal direction of the fibril by a periodic distance, D_{period} = 67 nm, generating a characteristic pattern of gap zones 40 nm long and overlap zones 27 nm long within the fibril. In a cross section of the fibril, tropocollagen molecules are arranged in a quasi-hexagonal array (Lees et al., 1987).

(b) Apatite mineral: are assumed to be plate-like shaped (Weiner et al., 1992) and distributed in a staggered arrangement in the longitudinal direction of the collagen fibril and in parallel layers in the transverse directions of the fibril **(**Jäger et al. 2000; Martinez et al., 2015**)**.

The present work reports the analysis for four different degrees of mineralization (i.e., V_{f_A} = 0.07, V_{f_A} = 0.32, V_{f_A} = 0.42 and V_{f_A} = 0.52). Dimensions of the apatite platelets have represented an important issue in developing the present numerical study since quantitative information about geometric parameters of the mineral crystals still represents a matter of debate. To date, experimental characterization at the nanoscale for low mineralized bone structure has not been undertaken. Therefore, the analysis to partially mineralized tissue is extended by adopting the value for the low volume fraction condition, i.e. V_{f_A} = 0.07, considered in the computational studies of Vercher-Martinez et al. (2015). The lower intermediate condition of mineral volume fraction, i.e. V_{f_A} = 0.32, is adapted from Jäger et al. (2000). Similarly, the upper intermediate degree of mineralization, i.e. V_{f_A} = 0.42 is determined from Nikolov et al. (2008). The high degree of mineralization, i.e. V_{f_A} = 0.52 (Jäger et al., 2000; Nikolov et al. 2008) is analysed in order to achieve information also for hypermineralized conditions, that may occur during aging (Burr, 2002) or in pathological cases of osteoporosis (McNamara et al., 2005).

For each model, which is characterized by a constant apatite volume fraction, all the geometrical parameters involved in the characterization of the unit cell have values that span across the extensive range indicated in literature (Table 3.1). These values were achieved by means of random extractions from Gaussian probability distribution functions (PDFs) in the ranges indicated in literature (Launey et al., 2010; Olstza et al., 2010; Fratzl et al., 2001; Rubin et al., 2003; Landis et al., 1993; Hassenkam et al., 2004). In the width and thickness directions, distances between neighbouring apatite platelets (a_W and a_T respectively) are of the same order as crystal thickness as achieved from TEM observations by Landis et al. (1993). In the longitudinal direction, the distance

Table 3.1. Range of values for the dimensions of the apatite platelets and collagen matrix

Parameter	Value (nm)	Reference
L	(70 - 130)	Hassenkham et al., 2004
W	(10 - 80)	Rubin et al., 2003
T	(2.5 - 5)	Rubin et al., 2003
$\mathbf{a_L}$	(4 - 64)	Rubin et al., 2003
$\mathbf{a_W}$	(5 - 20)	Landis et al., 1993
$\mathbf{a_T}$	(2 – 3.5)	Landis et al., 1993
d	(1.1 – 1.4)	Launey et al., 2010
$\mathbf{a_c}$	(1 - 1.5)	Fratzl et al., 2004

between two consecutive crystals, i.e. a_L, is set in order to satisfy the following condition (Jäger et al., 2000):

$$\left(\frac{L+a_L}{2}\right) = D_{period} \tag{3.1}$$

where L is the length of the apatite mineral and D_{period} is the length of the axial collagen period, i.e. D_{period} = 67 nm.

The mineral volume fraction is achieved applying the following equation (Vercher-Martinez et al., 2015):

$$V_{f_A} = \frac{L \cdot W \cdot T}{(L+a_L)\cdot(W+a_W)\cdot(T+a_T)} \tag{3.2}$$

where L, W, T are the length, width and thickness of the mineral platelet, a_L, a_W and a_T are the distances between the platelets in the longitudinal, width and thickness direction.

Each variable is extracted randomly from the corresponding Gaussian PDF. For each extracted set of values that characterizes the mineral platelets of the unit cell, the mineral volume fraction (VF) is calculated applying the Eq. 3.2. If the calculated value of mineral VF is not within the range (V_{f_A} ± 0.0005), where V_{f_A} represents the mineral VF investigated, the values of the geometric parameters are discarded and another extraction from the corresponding Gaussian PDF is performed. In order to perform the assessment of the water diffusion coefficient by means of the Monte Carlo technique, 5000 samples were considered for the geometrical parameters of the unit cell.

The development of the computational model required a local coordinate system aligned with the apatite platelet and a global coordinate system (CS_T) aligned with the axes of the single trabecula. According to Liebi et al. (2015), it is assumed that the mineral platelets and the collagen fibril composing a functional unit cell maintain their reciprocal parallelism independently of the cell inclination with respect to CS_T. We also consider that the orientation of the unit cell, i.e. the tern (θ_{LT}, θ_{WT}, θ_{LW}), is on average parallel to the axes of CS_T.

The inclination of mineral with respect to the longitudinal axis L is identified by the angle θ_{LW} in the LW plane and θ_{LT} in the LT plane. In the WT plane, the inclination, specified by θ_{WT}, is considered with respect to the W axis. Uncorrelated determinations of the three variables (θ_{LW}, θ_{LT}, θ_{WT}) are obtained by random extraction from Gaussian PDFs, identified by mean zero degrees and variable values of standard deviation (σ) in the range [0°; 20°] (Reznikov et al., 2015; Landis et al., 1993). In order to obtain a finite angle domain, the numerical simulations were performed considering truncated Gaussian distributions in the interval [-2σ; +2σ].

3.2.2. Diffusion coefficient

The mineralized collagen fibril is characterized as a composite porous material. Thus, the diffusion coefficient (D) is achieved introducing the tortuosity (τ), constrictivity (δ) and porosity factors (φ) (Shen et al., 2007; Van Brakel et al., 1974):

$$\boldsymbol{D}\left(\boldsymbol{\theta_{LT}},\boldsymbol{\theta_{LW}},\boldsymbol{\theta_{WT}},\boldsymbol{L},\boldsymbol{W},\boldsymbol{T},\boldsymbol{a_L},\boldsymbol{a_W},\boldsymbol{a_T}\right)=\boldsymbol{D_0}\cdot\frac{\boldsymbol{\delta}\left(\boldsymbol{\theta_{LT}},\boldsymbol{\theta_{LW}},\boldsymbol{\theta_{WT}},\boldsymbol{L},\boldsymbol{W},\boldsymbol{T},\boldsymbol{a_L},\boldsymbol{a_W},\boldsymbol{a_T}\right)\cdot\boldsymbol{\varphi}\left(\boldsymbol{L},\boldsymbol{W},\boldsymbol{T},\boldsymbol{a_L},\boldsymbol{a_W},\boldsymbol{a_T}\right)}{\boldsymbol{\tau}\left(\boldsymbol{\theta_{LT}},\boldsymbol{\theta_{LW}},\boldsymbol{\theta_{WT}},\boldsymbol{L},\boldsymbol{W},\boldsymbol{T},\boldsymbol{a_L},\boldsymbol{a_W},\boldsymbol{a_T}\right)} \tag{3.3}$$

where φ is the porosity of the medium, δ is the constrictivity factor and τ is the tortuosity factor.

The diffusion coefficient is significantly lower than free water diffusion coefficient (D_0), because of the hindering geometry and porosity of the collagen – apatite structure. The value of the self-diffusion coefficient of water at 27°C is $D_0 = 2.66 \cdot 10^{-9}\ m^2 \cdot s^{-1}$, estimated by means of molecular dynamics simulations in the study of Chiavazzo et al. (2014).

3.2.3 Tortuosity

The tortuosity factor (τ) is defined as the square ratio between the effective path length (ℓ_i) of the sinuous streamline and the Euclidean straight path, (ℓ_{i_E}) in the direction of flow, between the path extremes (Ghanbarian et al., 2013; Shen et al., 2007; Yun et al., 2006), i.e.:

$$\tau = \left(\frac{\ell_i}{\ell_{i\_E}}\right)^2 \tag{3.4}$$

The tortuosity is influenced by the arrangement of the collagen-apatite matrix and flow direction. The definition of tortuosity is adapted to the collagen-apatite network model. The implementation of the equation system that calculates the path lengths ℓ_i necessary to achieve the tortuosity value assumes that a concentration gradient exists along one of the three axes of the CS_T at a time and the pore space allows the crossing of a single molecule of water at a time. The assessment of the tortuosity was performed by analysing separately the contribution of the mineral and collagen matrix, respectively. The overall value of tortuosity (τ), introduced in Eq. (3.3), is obtained by combining both tortuosities, as indicated in Eq. (3.5):

$$\boldsymbol{\tau = \tau_{Apatite} \cdot \tau_{Collagen}} \tag{3.5}$$

where $\tau_{Apatite}$ is the tortuosity calculated in the mineral matrix and $\tau_{Collagen}$ is the tortuosity calculated in the collagen matrix.

3.2.3.1 Determination of tortuosity in the mineral matrix

For each inclination of the functional unit cell, the tortuosity is obtained applying Eq. (3.4). The tortuosity in the mineral matrix is determined with a geometrical approach (see Figure 5 in Bini et al., 2017; and Figures 2-4 in Bini et al., 2019). Taking into account the direction of the concentration gradient, the algorithm considers probable flow paths inside the unit cell in all the three main planes, i.e. LT, LW and WT. The effective path length is defined considering that between the platelets, the streamlines are parallel to the diffusion gradient, while close to the apatite crystals, the trajectories consisted of straight lines touching and passing by the mineral platelets. The path length

is calculated by means of geometrical considerations taking into account the apatite size and inclination (θ_{LT}, θ_{WT}, θ_{LW}). The resulting trajectories lengths (ℓ_i) are achieved through the equations S1-S36 reported in Bini et al. (2019). The Euclidean distance is defined as the straight line, parallel to the direction of the flow, that connects the path extremes, in absence of any obstacles, i.e. apatite minerals. Supplementary equations S1-S36 in Bini et al. (2019) assess also the straight-line distance (ℓ_{i_E}).

For each configuration of the unit cell, multiples streamlines are considered in order to reach the extremities of the unit cell. Therefore, the average of all values of tortuosity relative to a specific orientation are calculated as follows (3.6):

$$\boldsymbol{\tau_{Apatite}} = \frac{1}{\boldsymbol{N}} \sum_{\boldsymbol{i}} \boldsymbol{\tau}_{\boldsymbol{i}} \tag{3.6}$$

where N is the total number of flow paths relative to a specific orientation of the unit cell and τ_i is the tortuosity for the i^{th} streamline (Yun et al., 2006). The value obtained from Eq. (3.6) is then used in Eq. (3.5).

3.2.3.2 Determination of tortuosity in the collagen matrix

The tortuosity within the collagen matrix is calculated through Eq. (3.4) and considers that the cross-sections of the fibrils with respect to the axes of coordinate systems are elliptical as the collagen follows the mineral inclination. Therefore, the water molecule, given the densely packed structure of collagen, performs elliptical trajectories whose length (ℓ_i) is equal to the semi-perimeter of the ellipse, while the Euclidean distance (ℓ_{i_E}) corresponds to the major axis of the ellipse.

Let the ellipse be expressed as a parametric curve, i.e. $\left\{\boldsymbol{x}(\boldsymbol{t}) = \boldsymbol{a} \cdot \cos(\boldsymbol{t}), \boldsymbol{y}(\boldsymbol{t}) = \boldsymbol{b} \cdot \sin(\boldsymbol{t})\right\}$, its semi-perimeter can be calculated through the elliptic integral of second kind (Abramowitz et al., 1972):

$$\boldsymbol{L}(\boldsymbol{t}) = \int_{\boldsymbol{t}_{\min}}^{\boldsymbol{t}_{\max}} \sqrt{\boldsymbol{x}'(\boldsymbol{t})^2 + \boldsymbol{y}'(\boldsymbol{t})^2}\, \boldsymbol{dt} \tag{3.7}$$

where **a** is the semi-major axis of the ellipse, **b** is the semi-minor axis of the ellipse and $\mathbf{t_{min}}$, $\mathbf{t_{max}}$ are the extreme angles of the arc considered. The minor semi-axis of the ellipse is equal to the radius of

the tropocollagen molecule, while the major semi-axis depends on the inclination (θ_{LT}, θ_{WT}, θ_{LW}) of the apatite with respect to the CS_T.

For a flow parallel to the longitudinal direction in the LT plane (Eq 3.8) and LW plane (Eq. 3.9), the semi-major axis of the ellipse is obtained as follows:

$$\boldsymbol{a} = \frac{\boldsymbol{d}}{2 \cdot \cos(\boldsymbol{\theta_{LW}}) \cdot \sin(\boldsymbol{\theta_{LT}})} \tag{3.8}$$

$$\boldsymbol{a} = \frac{\boldsymbol{d}}{2 \cdot \sin(\boldsymbol{\theta_{LW}}) \cdot \cos(\boldsymbol{\theta_{LT}})} \tag{3.9}$$

For a flow parallel to the width direction in the LW plane (Eq. 3.10) and WT plane (Eq. 3.11), the semi-major axis of the ellipse, is calculated as follows:

$$\boldsymbol{a} = \frac{\boldsymbol{d}}{2 \cdot \cos(\boldsymbol{\theta_{LW}}) \cdot \cos(\boldsymbol{\theta_{LT}})} \tag{3.10}$$

$$\boldsymbol{a} = \frac{\boldsymbol{d}}{2 \cdot \cos(\boldsymbol{\theta_{LW}}) \cdot \cos(\boldsymbol{\theta_{LT}})} \tag{3.11}$$

For a flow parallel to the thickness direction in the LT plane (Eq. 3.12) and WT plane (Eq. 3.13), the semi-major axis of the ellipse, is calculated as follows:

$$\boldsymbol{a} = \frac{\boldsymbol{d}}{2 \cdot \cos(\boldsymbol{\theta_{LW}}) \cdot \cos(\boldsymbol{\theta_{LT}})} \tag{3.12}$$

$$\boldsymbol{a} = \frac{\boldsymbol{d}}{2 \cdot \cos(\boldsymbol{\theta_{LW}}) \cdot \cos(\boldsymbol{\theta_{LT}})} \tag{3.13}$$

In the case of the collagen matrix, the Euclidean distance, l_{i_E}, is represented by the major axis of the ellipse.

3.2.4 Constrictivity

The constrictivity $\delta \in [0, 1]$ represents the hindrance to which the fluid is subject travelling through pores of varying cross section (Van Brakel et al., 1974; Stenzel et al., 2016). It becomes important only if the size of the solute, i.e. water molecule, is comparable to the dimensions of the pores. Several studies (Curie et al., 1960; Takahashi et al., 2009) evaluate δ as a function of the ratio of the maximum and minimum cross section for different pore size structures:

$$\delta = \frac{\sqrt{\max \textbf{\textit{cross}}\ \text{sec}\textbf{\textit{tion}} \cdot \min \textbf{\textit{cross}}\ \text{sec}\textbf{\textit{tion}}}}{\textbf{\textit{mean cross}}\ \text{sec}\textbf{\textit{tion}}} \tag{3.14}$$

Variations of the width of the passageway in the collagen-mineral matrix are due to the distance between the collagen molecules and the spacing between collagen and apatite (see Figure 5 in Bini et al., 2019). These distances are influenced by the dimensions of the matrix and the inclination with respect to the CS_T.

The relations that enable to achieve the constrictivity in each plane by means of equation (3.14) are reported below.

In the WT plane the minimum and maximum cross section are assessed as follows:

$$\min \textbf{\textit{cross}}\ \text{sec}\textbf{\textit{tion}} = \frac{\boldsymbol{a_c}}{\cos\left(\boldsymbol{\theta_{LW}}\right)} \tag{3.15}$$

$$\max \textbf{\textit{cross}}\ \text{sec}\textbf{\textit{tion}} = \frac{\boldsymbol{a_T - d}}{2 \cdot \cos\left(\boldsymbol{\theta_{LW}}\right) \cdot \cos\left(\boldsymbol{\theta_{LT}}\right)} \tag{3.16}$$

In the LT plane the minimum and maximum cross section are calculated from the relations:

$$\min \textbf{\textit{cross}}\ \text{sec}\textbf{\textit{tion}} = \frac{\boldsymbol{a_c}}{\cos\left(\boldsymbol{\theta_{LW}}\right)} \tag{3.17}$$

$$\max \textbf{\textit{cross}}\ \text{sec}\textbf{\textit{tion}} = \frac{\boldsymbol{a_T - d}}{2 \cdot \cos\left(\boldsymbol{\theta_{LW}}\right) \cdot \cos\left(\boldsymbol{\theta_{LT}}\right)} \tag{3.18}$$

In the LW plane the minimum and maximum cross section are determined as follows:

$$\min \textbf{\textit{cross}}\ \text{sec}\textbf{\textit{tion}} = \frac{\boldsymbol{a_c}}{\cos\left(\boldsymbol{\theta_{LW}}\right)} \tag{3.19}$$

$$\max \boldsymbol{cross}\ \text{sec}\boldsymbol{tion} = \frac{\boldsymbol{a_W} - \boldsymbol{n}\cdot(\boldsymbol{d}+\boldsymbol{a_c})}{\cos(\boldsymbol{\theta_{LW}})\cdot\cos(\boldsymbol{\theta_{LT}})} \tag{3.20}$$

where **n** is equal to the number of collagen fibrils between the apatite platelets in the width direction.

3.2.5 Porosity

The porosity is considered independent from the inclination of the functional unit cell and is calculated by equation (3.21) (Vercher-Martinez et al., 2015):

$$\varphi = 1 - V_f \tag{3.21}$$

where V_f is the volume fraction of the unit cell and is expressed by Eq. (3.22):

$$\boldsymbol{V_f} = \boldsymbol{V_{f_A}} + \boldsymbol{V_{f_{collagen}}} = \frac{\boldsymbol{LWT}}{(\boldsymbol{L}+\boldsymbol{a_L})\cdot(\boldsymbol{W}+\boldsymbol{a_W})\cdot(\boldsymbol{T}+\boldsymbol{a_T})} + \frac{\boldsymbol{n_c}\boldsymbol{\pi}\cdot(0.5\boldsymbol{d})^2\cdot(\boldsymbol{L}+\boldsymbol{a_L}-0.6\boldsymbol{D})}{(\boldsymbol{L}+\boldsymbol{a_L})\cdot(\boldsymbol{W}+\boldsymbol{a_W})\cdot(\boldsymbol{T}+\boldsymbol{a_T})} \tag{3.22}$$

where n_c is equal to the number of collagen fibrils, d is the diameter of the collagen fibrils and D is the axial period of the collagen fibrils, respectively.

3.2.6 Determination of the diffusion coefficients

For each plane (i.e., LW, LT, WT), the diffusion along the two main orthogonal directions that characterize the plane is investigated. The structural factors, i.e. tortuosity and constrictivity, and the diffusion coefficients along the main axes of the trabecula, i.e. L, W and T, are predicted by means of Monte Carlo method (Mathematica 10, Wolfram, Oxfordshire, UK). The algorithm implemented for a concentration gradient along one of the axes of the trabecula can be summarized as follows:

(a) Random extraction of the standard deviations (σ_{LT}, σ_{LW}, σ_{WT}) that characterize the Gaussian PDFs;

(b) Fixed the value for σ_{LT}, σ_{LW} and σ_{WT}, respectively, random extraction of the apatite inclination tern ($\theta_{LW,}$ θ_{LT}, θ_{WT}) from the corresponding Gaussian PDFs

(c) Random extraction of the geometric parameters of the apatite matrix, i.e. L, W, T, a_T, a_W, and the collagen fibrils, i.e. d, a_c, from the corresponding Gaussian PDFs. The

parameters concerning the mineral matrix have to satisfy the value of the mineral volume fraction imposed. Otherwise, random extractions are carried until this condition is satisfied.

(d) Fixed the inclination tern ($\theta_{LW,}$ θ_{LT}, θ_{WT}), calculation of the tortuosity in function of the parameters previously set, following the procedure illustrated in the subsection "Tortuosity" is performed.

(e) Fixed the inclination tern ($\theta_{LW,}$ θ_{LT}, θ_{WT}), calculation of the constrictivity characteristic of the collagen matrix, following the procedure illustrated in the subsection "Constrictivity" is performed.

(f) Calculation of the diffusion coefficient by means of Eq. (3.3).

(g) Repeating all previous steps until completing N realizations, where N = 5000 is the imposed number of samples for the apatite platelets size and inclination, respectively.

(h) Repeating all the previous step up to the imposed number of Gaussian PDF considered for the apatite inclination, i.e. M= 5000 different Gaussian PDFs.

The output of the Monte Carlo simulations provides the tortuosity, constrictivity and diffusion coefficient for different configuration of mineral platelets along the orthogonal directions of the main planes of the coordinate system (i.e. LW, LT, and WT plane). For a fixed concentration gradient, the geometrical approach implemented for the assessment of the constrictivity and tortuosity allows to achieve information about the previous two structural factors and the effective diffusion coefficient from two planes. Therefore, an average between the two values resulting from the two different planes and competing to a specific apatite platelet configuration is performed. Subsequently, the mean of means of the constrictivity, tortuosity and effective diffusion coefficient respectively, corresponding to each Gaussian PDF considered for the mineral inclinations is calculated.

3.2.7 Statistical analysis

It was performed a nonlinear fit on the mean of means of the diffusivity corresponding to each diffusion gradient in function of the tortuosity and constrictivity factors, respectively. It was also reported a confidence interval of 95 percent that provides the interval for predicting the diffusivity

mean of means at fixed values of the predictors, i.e. mean of means of tortuosity and mean of means of constrictivity. It is calculated as follows:

$$\boldsymbol{D_{fitting}} \pm \boldsymbol{k} \cdot \sqrt{\boldsymbol{\sigma}^2 + \sum} \tag{3.23}$$

where $\mathbf{D_{fitting}}$ is the fitting value of the diffusivity mean of means, $\mathbf{k}$ = 1.96044 is the coverage factor, $\boldsymbol{\sigma}^2$ is the estimated error variance and $\boldsymbol{\Sigma}$ is the estimated covariance matrix for the parameters. The estimated error variance is calculated as:

$$\boldsymbol{\sigma}^2 = \frac{\sum_{\boldsymbol{i}} (\boldsymbol{D_i} - \boldsymbol{D_{fitting}})^2}{\boldsymbol{N} - 1} \tag{3.24}$$

The estimated covariance matrix is obtained as:

$$\Sigma = \hat{\boldsymbol{\sigma}}^2 \cdot \left(\boldsymbol{X}^{\boldsymbol{T}} \cdot \boldsymbol{W} \cdot \boldsymbol{X} \right)^{-1} \tag{3.25}$$

where $\hat{\boldsymbol{\sigma}}^2$ is the variance estimate, $\mathbf{X}$ is the design matrix and $\mathbf{W}$ is the diagonal matrix of weights.

3.3 RESULTS

The computational simulations of the diffusion phenomenon within a repeating unit cell of bone nanostructure have the aim to analyse the influence of the structural characteristics on the diffusion coefficient of water. The diffusivity is predicted by assuming a concentration gradient parallel to the three axes, i.e. L, W, T, of a global coordinate system (CS_T) fixed to the main axes of the trabecula.

The diffusion coefficient of water is determined in function of the apatite platelets orientation, the tortuous factor of the structure and the variation of the available passageway between tropocollagen molecules, i.e. constrictivity. Subsequently, the values of the diffusivity are represented in function of the tortuosity and the constrictivity calculated for flows parallel to the Longitudinal (Figure 3.2), Width (Figure 3.3) and Thickness (Figure 3.4) directions for the four degrees of mineralization considered, i.e. V_{f_A} = 0.07, V_{f_A} = 0.32, V_{f_A} = 0.42 and V_{f_A} = 0.52. The colour gradient illustrates the standard deviation of the Gaussian PDF that characterizes the apatite inclination with respect to the main axes of the coordinate system.

Table 3.2. Standard deviation of the Gaussian PDF representing the inclination of the apatite platelets matching the diffusion coefficient in agreement to Marinozzi et al., (2014b)

Diffusion coefficient	V_{f_A}= 0.32		
	σ_{LW}	σ_{LT}	σ_{WT}
D_L	8.6°	10.7°	8.5°
D_W	11.2°	13.8°	14.4°
D_T	8.3°	10.5°	12.5°

The diffusion coefficient D_L is represented in function of the standard deviation σ_{LT} related to the Gaussian PDF of the mineral inclination θ_{LT}. The diffusivity D_W is represented in function of the standard deviation σ_{LW} while D_T is represented in function of σ_{LT}. Here are reported the diffusion coefficients in function of the standard deviation of the inclination from which it was observed major influence. Other plots of the diffusivity are reported in Appendix A, i.e. D_L in function of the standard deviation σ_{LW}, D_W and D_T in function of the standard deviation σ_{WT}.

In line with the outcomes of Depalle et al. (2016) and Jäger et al. (2000), the lower intermediate mineral VF is assumed to represent a normal degree of mineralization. Therefore, a comparison between the coefficients obtained by means of Monte-Carlo method for the lower intermediate mineral VF and the genetic algorithm (Table 3.2) is performed. In this manner, it is possible to achieve an optimal arrangement of the mineral - collagen model that better mimics the experimental results (Marinozzi et al., 2014b).

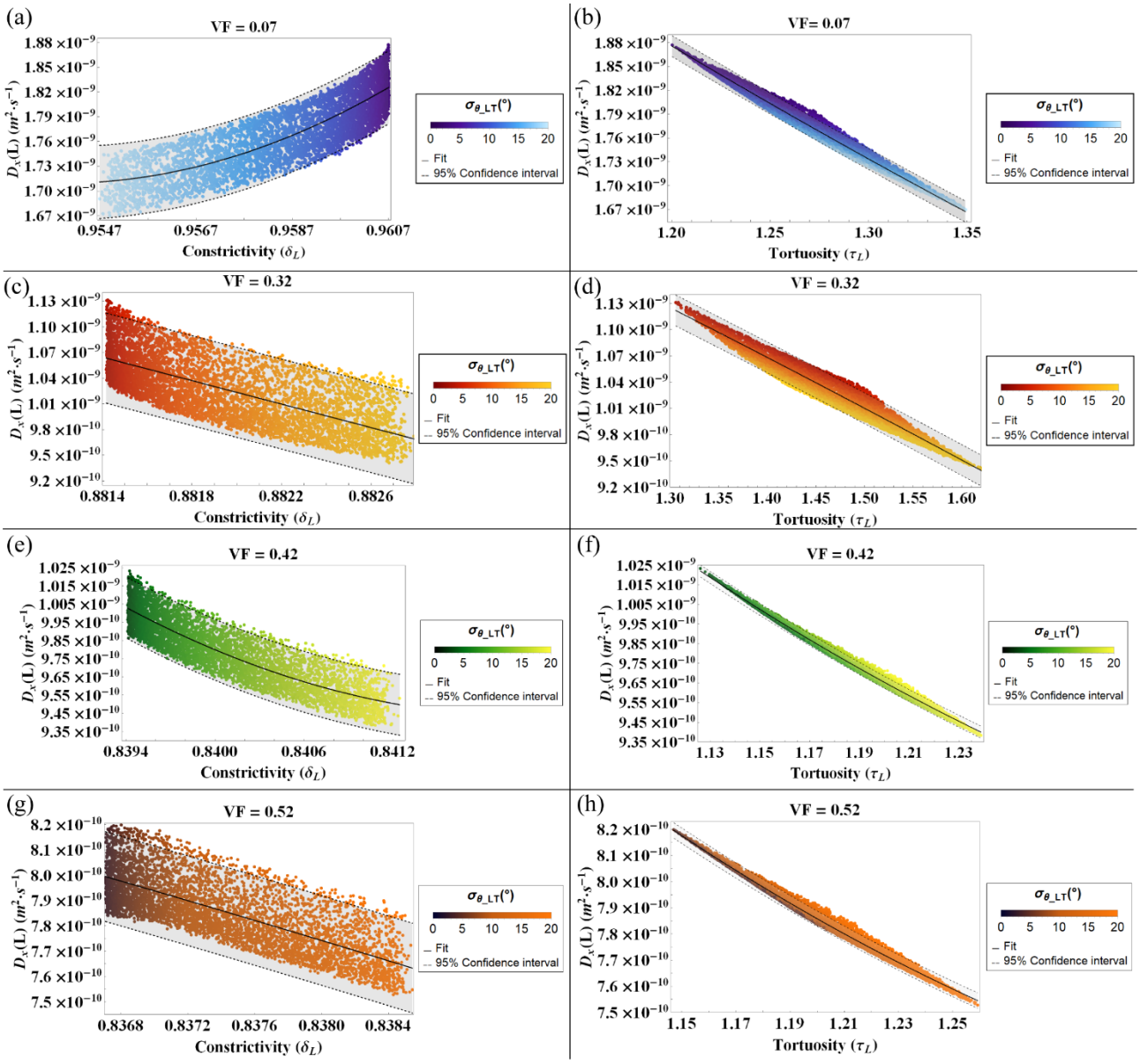

Figure 3.2: Diffusion coefficient (D_L) for a flow parallel to the longitudinal axis (L) represented in function of the constrictivity (a, c, e, g) and tortuosity factors (b, d, f, h) for different mineralization degrees, i.e. V_{f_A} = 0.07 (a, b), V_{f_A} = 0.32 (c, d), V_{f_A} = 0.42 (e, f) and V_{f_A} = 0.52 (g, h). The colour gradient indicates the standard deviation (σ_{LT}) of the Gaussian PDF that characterizes the inclination of the apatite minerals in the LT plane. The grey bands show the Confidence Interval at 95 percent.

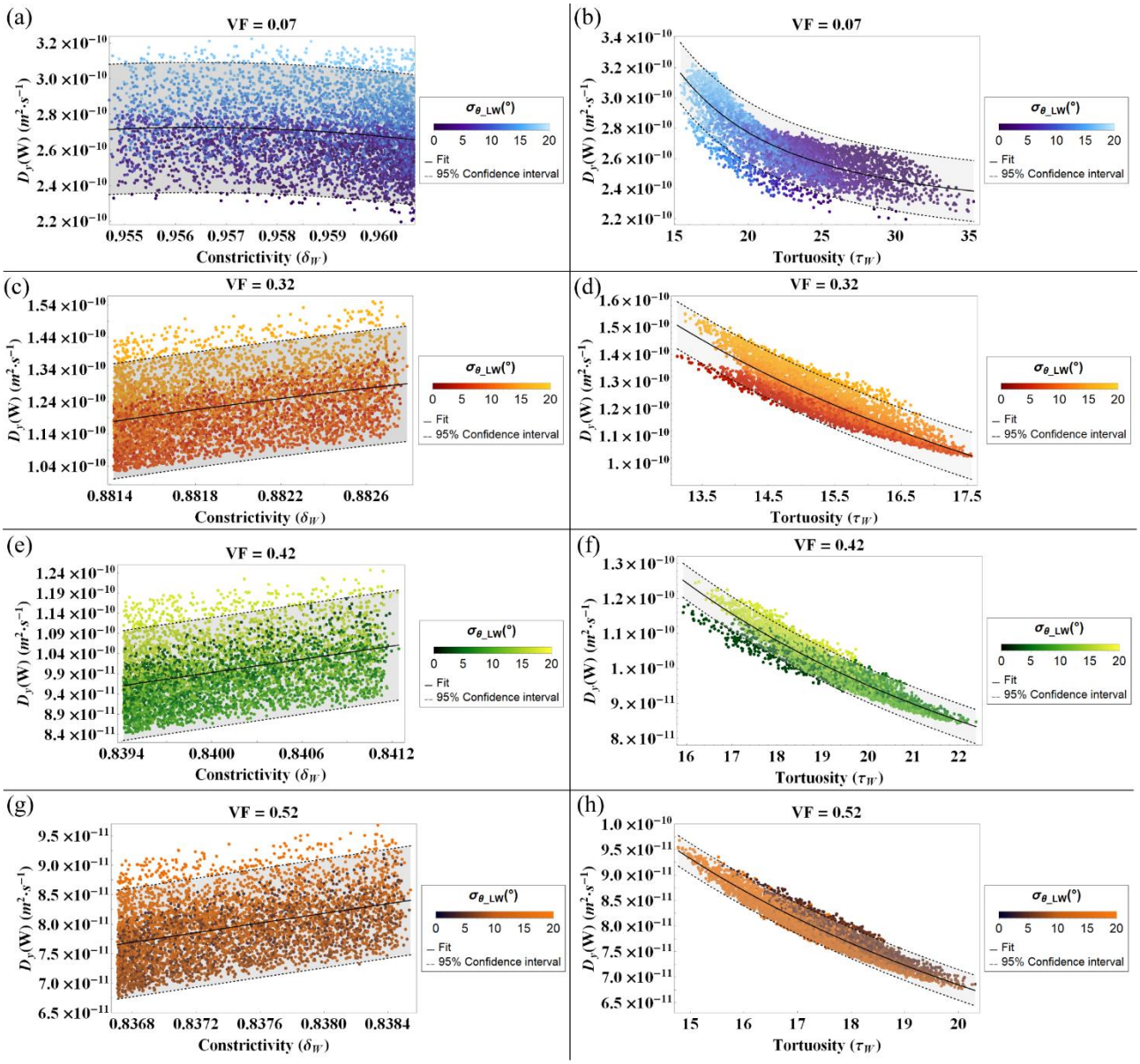

Figure 3.3: Diffusion coefficient (D_W) for a flow parallel to the width direction (W) represented in function of the constrictivity (a, c, e, g) and tortuosity factors (b, d, f, h) for different mineralization degrees, i.e. V_{f_A} = 0.07 (a, b), V_{f_A} = 0.32 (c, d), V_{f_A} = 0.42 (e, f) and V_{f_A} = 0.52 (g, h). The colour gradient indicates the standard deviation (σ_{LW}) of the Gaussian PDF that characterizes the inclination of the apatite minerals in the LW plane. The grey bands show the Confidence Interval at 95 percent.

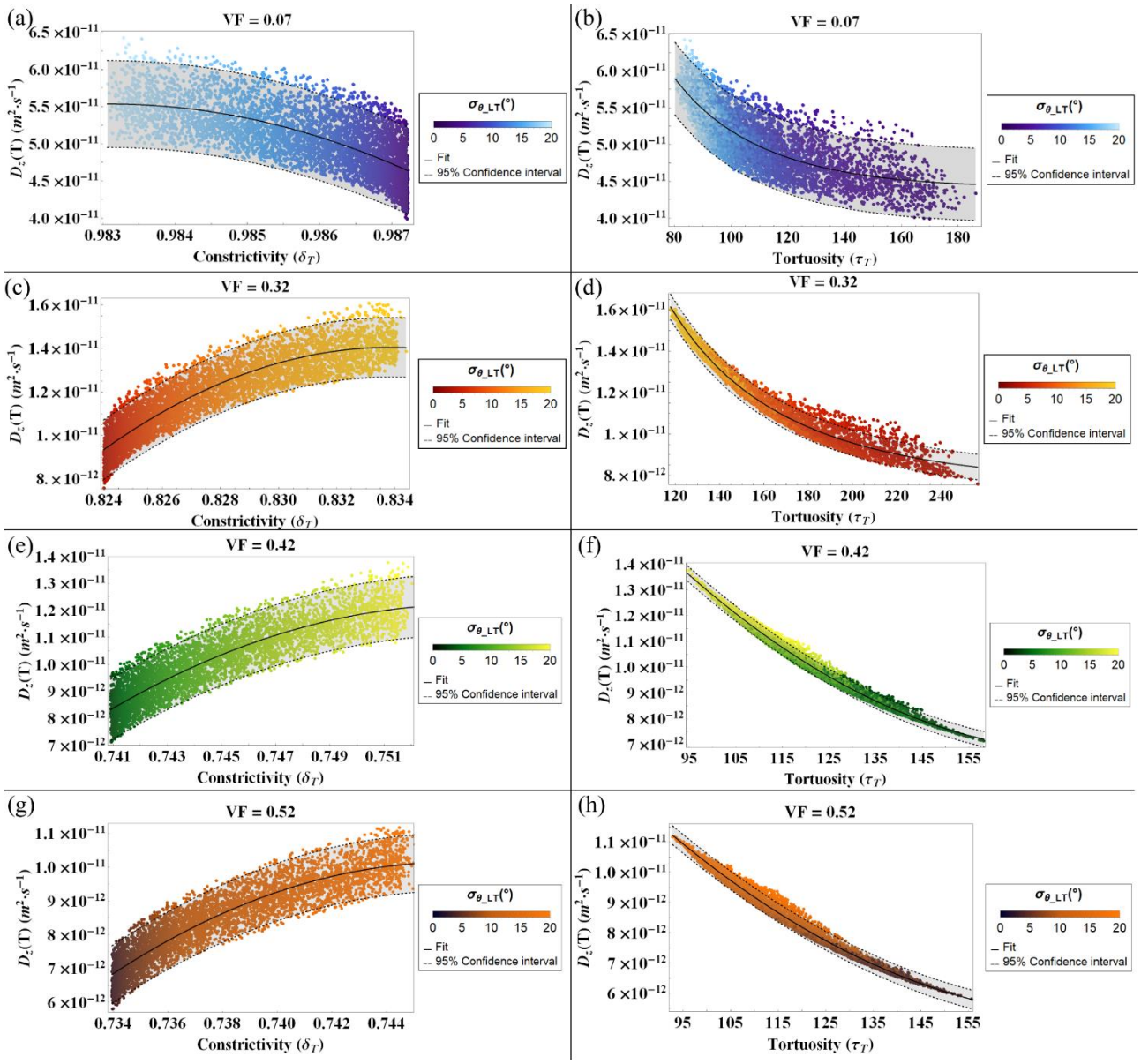

Figure 3.4: Diffusion coefficient (D_T) for a flow parallel to the thickness direction (T) represented in function of the constrictivity (a, c, e, g) and tortuosity factors (b, d, f, h) for different mineralization degrees, i.e. V_{f_A} = 0.07 (a, b), V_{f_A} = 0.32 (c, d), V_{f_A} = 0.42 (e, f) and V_{f_A} = 0.52 (g, h). The colour gradient indicates the standard deviation (σ_{LT}) of the Gaussian PDF that characterizes the inclination of the apatite minerals in the LT plane. The grey bands show the Confidence Interval at 95 percent.

3.4 DISCUSSIONS

Water plays a fundamental role concerning the provision of nutrients and the interaction between mineral and proteins constituents (Wang et al., 2013), enhancing the strength of the mineral phase within MCF. An impairment of the diffusion process may affect also the bone remodelling process (Lemaire et al., 2004) since the mass transport contributes actively to the signalling functions that are involved in the tissue growth.

In this Chapter, the structural factors that influence the diffusion process have been analysed. Firstly, it is analysed the dependence of the tortuosity and constrictivity on the organization of the mineral crystals within the mineralized collagen fibril and the mineral aspect ratio that characterizes each degree of mineralization. Subsequently, the effect of the geometric factors, i.e. tortuosity and constrictivity on the diffusion coefficient of water is highlighted for different mineral volume fractions.

The investigation of water diffusion within bone nanostructure is an issue of interest for experimental (Marinozzi et al., 2014a; 2014b) and also for numerical studies (Lemaire et al., 2015). Both approaches have highlighted pronounced anisotropy within the MCF. In fact, the analysis of Marinozzi et al. (2014b) revealed that the diffusion coefficient along the longitudinal axis of the trabecula (D_L) is greater with one order of magnitude than the coefficient along the width direction (D_W) and with two orders of magnitude than the coefficient in the thickness direction (D_T). The findings of the 3D model presented in this Chapter are in agreement with previous studies (Marinozzi et al., 2014b; Pham et al., 2015) and provide further insights with regard to the relationship between structure and mass transport properties.

Overall, the values of tortuosity, constrictivity and, subsequently diffusivity are influenced by the degree of mineralization. It should be mentioned that the order of magnitude of the ratio between the diffusion coefficients achieved with the Monte Carlo technique is in agreement with the experimental study of Marinozzi et al. (2014a; 2014b).

Specifically, the low apatite volume fraction, i.e. $V_{f\_A} = 0.07$, is characterized by slightly higher values of the diffusion coefficient in comparison to the diffusivity obtained from experimental investigations. In addition, the lower intermediate degree of mineralization, $V_{f\_A} = 0.32$, provides outcomes in line with the study of Marinozzi et al. (2014b). For hypermineralization conditions, i.e. $V_{f\_A} = 0.42$ and $V_{f\_A} = 0.52$, the effect of the tortuosity and constrictivity for all the principal flow

directions corresponds to a decrease of the diffusion coefficient with respect to the values achieved previously by Marinozzi et al. (2014b).

Figures 3.2 -3.4 illustrate the dependence of the diffusion coefficient on the constrictivity and tortuosity factors. The colour gradient provides information related to the effect of apatite inclinations with respect to the main axes of the coordinate system on the mass transport properties. In line with its definition (Equation 3.14), the constrictivity may achieve values in the interval 0-1, where the maximum value indicates a constant cross section of the passageway of water particles.

Conversely, following Equation 3.4, the tortuosity assumes values greater than 1. It can be deduced that the presence of mineral increases the path length of the water molecule with respect to the shortest distance between the path extremities in a homogeneous medium (Shen et al., 2007). Figures 3.2-3.4 show that for a fixed mineral volume fraction the variations of the tortuosity and constrictivity are due to variations of the apatite orientation with respect to the CS_T.

For a parallel flow to the longitudinal direction (Figure 3.2), the arrangement of the apatite crystals does not represent a significative obstacle to the water diffusion and therefore the tortuosity assumes values close to the unity, for all degrees of mineralization considered. However, for high mineralized conditions, there is a slightly decrement of the tortuosity since the packing of the apatite platelets for high VF avoids the water molecule to perform tortuous paths. Small variations, at the third decimal place, are noticed also for the constrictivity. From the analysis of the apatite crystals orientation, it can be highlighted that quasi aligned platelets to the longitudinal axis of the MCF, i.e. σ_{LT} lower than 10 degrees, are characterized by higher diffusivity values and subsequently lower tortuosity and constrictivity values.

A parallel flow to the width direction (Figure 3.3) is characterized by an increased value of tortuosity of an approximatively one order of magnitude with respect to the tortuosity in the longitudinal direction. Changes in the constrictivity values occur only at the third decimal place, suggesting a small influence on the diffusion coefficient. From Figure 3.3 it can be noticed that a relationship between the constrictivity values and inclination of the mineral in the LW plane cannot be established. Conversely, increased values of tortuosity, for a determined mineral VF led to decreased values of the diffusivity D_W. Overall, the diffusion coefficient D_W increases for mineral platelets characterized by Gaussian PDFs with higher standard deviations.

The tortuosity determined for flow in T direction (Figure 3.4) increases noticeably since the arrangement of the mineral is more complex. For higher standard deviation of the Gaussian PDFs that describe the inclination of platelet in LT plane the tortuosity increases and therefore the diffusion

coefficient achieves lower values. Conversely, for the constrictivity higher values are obtained for increased standard deviation of the apatite inclination.

Overall, the tortuosity exhibits a remarkable variation for the different flow directions analysed. Comparing with the values achieved in the longitudinal direction, this structural factor increases with an order of magnitude when considering flow paths in the width direction and with two orders of magnitude when the streamlines are developed in the thickness direction. The constrictivity does not show important variations in function of the concentration gradient and in function of the mineral platelets inclination. Therefore, it emerges that the tortuosity is highly influenced by the anisotropy of the medium and it is the main parameter controlling the effective diffusion coefficient.

The outcomes discussed provide further insights into the architecture of bone nanostructure. This study provides quantitative information about the orientation of the mineral with respect to the axes of the CS_T. Moreover, the agreement with the diffusivity values achieved from experimental investigations by Marinozzi et al. (2014b) confirms the suitability of the model developed. The variations of the mineral content are achieved assuming higher dimensions of platelets and lower distances between apatite crystals for increasing mineral VF. According to Literature, the major variation is applied to the mineral width, while the crystal thickness has minimal increments. The results show that hypermineralized conditions of the nanostructure are characterized by lower diffusion coefficients. This outcome is also in agreement with the investigations of Roschger et al., (2008) that highlight that in osteoporotic cases, water is replaced by an increment of the mineral density.

However, some limitations of the model should be mentioned. The study is based on a unit cell of the mineralized collagen fibril, while a major number of crystals should be assembled to better mimic the tissue structure. Moreover, the model adopted a fixed value for the apatite periodicity in the longitudinal direction, i.e. 67 nm. It should be investigated a realistic range of values of this parameter since it also influences tissue mass properties.

Despite these limitations, the model provides good predictions for the diffusivity and it can be a support for predictive studies of bone properties at nanoscale.

CHAPTER 4

Percolation in a 3D Model of the Human Mineralized Collagen Fibril

The aim of this study is to investigate the structural behaviour of bone nanostructure adopting the continuum percolation theory. The latter provides insights into the variation of the mineral framework within the mineralized collagen fibril as the degree of mineralization varies. Monte Carlo technique is implemented to assess the 3D model of the apatite platelets. The outcomes highlight that spanning networks of connected apatite crystals are more likely to develop in hypermineralized conditions. Percolating structures modify their structural properties and may develop structural instability.

4.1 INTRODUCTION

4.1.1 Problem contextualization

Hierarchical structure of bone contributes actively to the multiple functions of the tissue as well as to its capability of adaptation, growth and repair. The highly organized embedded nanometric building blocks of collagen molecules and apatite crystals lead to enhanced features of the mineralized collagen fibril (MCF) with respect to the characteristics of the single constituents. The collagen component provides elasticity to the structure, while the apatite minerals leads to an increment of the MCF stiffness. Various combinations of these constituents may amplify or counterbalance their individual effects.

The MCF mineralization is a fundamental process in biology and influences the mechanical behaviour of bone (Wagermaier et al., 2015). In fact, without a precise regulation and control performed by the organic molecules and bone cells, i.e. osteoblasts and osteoclasts, pathological mineralization can easily occur, leading to a hypomineralized tissue, as it occurs in the case of osteomalacia or to a hypermineralized tissue, as it is the case of osteoporosis. It is confirmed that collagen molecules play an active role in mineralization by controlling the growth pathways of the apatite crystals (Liebe et al., 2015; Nudelman et al., 2013; Xu et al., 2020). In addition, the dynamic equilibrium between bone formation and bone resorption is ensured by the activity of osteoblasts and osteoclasts, respectively.

Information in literature concerning bone crystal growth is still limited. Following nucleation, apatite crystals grow through many processes dominated by nanoparticles attachment or addition of monomeric chemical species on existing crystals (Wang et al., 2017). Experimental studies (Wang et al., 2017) suggest that nanocrystals attachment through collision and coalescence events are prevalent.

Experimental studies of Currey (1969) highlighted a steep variation in the mechanical properties of the MCF depending on its mineral content. This sudden change becomes a critical issue since it represents an unusual behaviour in material composites (Currey, 1969). The Author proposed that as the mineral content increases in MCF, apatite crystals join end to end. A similar increment in mineral length may lead to an increment of stiffness in bone.

Apatite crystals fusion has been suggested also by Landis et al. (1993). Such an array of mineral could conceivably be extremely relevant for biomechanical properties since the arrangement of mineral in this manner could influence stress, shear, fracture strength and other features of MCF.

The presence of arrays of apatite platelets fused together remains intriguing since visualizing apatite platelets within the MCF is still challenging. Although improvements toward the visualization techniques have been made (Reznikov et al., 2018; Xu et al., 2020), no general consensus has been reached regarding the morphology and arrangement of bone mineral.

The study presented in this Chapter represents an attempt to analyse the mineral network within the MCF under the perspective of the percolation theory. Percolation is a simple fundamental model in statistical mechanics and presents an interesting paradigm to investigate scenarios of MCF mineralization.

4.1.2 Percolation theory

Percolation phenomena are associated with the effects of local and global connectivity in systems composed of elementary particles that are distributed randomly (Torquato, 2002). The percolation theory investigates the appearance, evolution and properties of connected elements (Baalberg, 2016). These phenomena exhibit phase transitions signalled by the onset of a long range (infinite) connected component. A cluster is defined as a connected group of elements. The percolation transition of the system is the point, called percolation threshold, at which the first cluster that crosses the system from one side to another appears, i.e. the onset of long-range connectivity (Torquato, 2002). The most studied manifestations of percolation phenomena are those in proximity to the emergence of global connectivity, i.e. close to the percolation threshold.

The term “Percolation” was first introduced by Broadbent and Hammersley (1957) that investigate the passage of fluid through a network of channels in a porous medium, with some channels blocked at random. In this scenario, the connectivity pathway is obtained by considering the unblocked channels. The Authors demonstrated that there will be no fluid flow if the fraction of open channels p_{ch} is smaller than a threshold. For increasing p_{ch} values, the flow rate will increase monotonically until it achieves the maximum value, i.e. 1.

Percolation phenomena can be identified in a wide variety of applications, among others transport and mechanical properties of composites and porous media, spread of diseases and fires,

gelation, conductor-insulator transition, fracture processes in heterogeneous rock formation, glass transition and star formation in galaxies (Torquato, 2002). The exponential interest of specialists in percolation structures is explained by the importance of the study of critical phenomena. The onset of percolation behaviour cardinally modifies the material: it occurs a structural phase transition, the object symmetry and other parameters vary, thus leading to changes in the mechanical, physical and chemical characteristics of the structure. For instance, the emergence of connected clusters may modify the conductivity processes, the kinetics of chemical reactions or the mechanical toughness (Herega, 2015). Thus, in percolation studies the formation of a cluster system and its impact on the structure are both investigated simultaneously.

Two main theoretical formalisms have been developed to study cluster formation and percolation, namely discrete and continuum. The initial works concerning percolation phenomena applied and consolidated the concepts associated with the discretisation of space in lattice models (Stauffer and Aharony, 1985). The main difference between lattice and continuum percolation is that in continuum percolation the analysis is performed on real objects that have variable sizes and shapes and are randomly distributed in space, while in lattices we are dealing with abstract mathematical objects such as dots and line segments in a priori defined locations.

4.1.2.1 Discrete percolation

In the discrete percolation approach, each site on a lattice is occupied with probability *p* and unoccupied with probability *1-p* according to some random process. Similarly, for bond percolation on a lattice, each bond is occupied (open) with probability *p* and unoccupied (closed) with probability *1-p* (Torquato, 2002; Newman and Ziff, 2001). Clusters are occupied sites or bonds that are connected by having pairs of occupied sites (bonds) when the latter are neighbours. The system shows a phase transition at a finite value of *p*, which on a regular lattice is characterized by the formation of a cluster that spans the system from one side to another. This condition represents a percolating system. The percolation threshold depends on the space dimension, lattice structure and interactions between elements. Graphical representation of site and bond percolation on a square lattice are given in Figure 4.1, below and above percolation threshold, assumed as $p_c=1/2$.

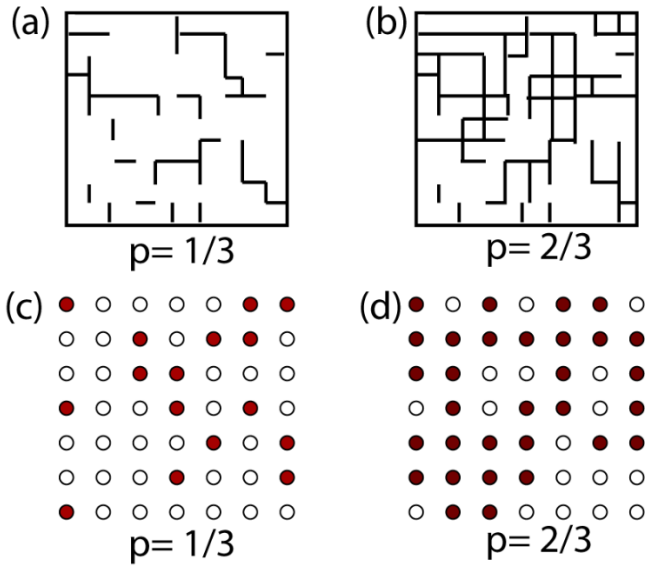

Figure 4.1: Bond networks on a square lattice below (a) and above (b) the percolation threshold. In (c) and (d) site networks on a square lattice below and above the percolation threshold, respectively.

Site and bond percolation have been used in studies concerning fluid passage through rocks composite materials, polymers, porous media (Torquato, 2002). However, the lattice models are much easier to simulate, due to the ordered nature of their underlying structures (Rintoul and Torquato, 1997).

4.1.2.2 Continuum percolation

Continuum percolation is a more realistic model of percolation process that occurs in real heterogeneous materials. It investigates systems in which no discretization of sites is performed. In continuum percolation, the system is composed of objects that are randomly placed in space that may be of various sizes and shapes and, if non spherical may have a distribution of their orientations (Torquato, 2002). Initially the studies analysed 2D models, while in recent times the percolation approach has been applied also to 3D models.

The main classes of continuum modelling are:

- ***Soft-core models***: the particles are modelled as completely interpenetrating objects. Two particles are considered connected when they overlap. In this type of model, 2D

geometric objects as squares (Baker et al., 2002), ellipses (Pike and Seager, 1974), circles (Lee and Torquato, 1988) or sticks (Zeng et al., 2011) are analysed. In recent times, 3D models have been proposed investigating systems of cuboids (Lin et al., 2018), cylinders (Finner et al., 2018), ellipsoids (Garboczi et al., 1995).

- ***Hard-core models***: the particles may be in contact with each other, but they do not merge. In this case, touching particles form a connected network. Generally, 3D geometries of cubes (Pike and Seager, 1974), cylinders (Gu et al., 2016), ellipsoids (Garboczi et al., 1995) have been developed under this assumption.

- ***Hard-core with soft-shell models***: it is assumed that particles are constituted by hard core surrounded by soft shell. In this scenario, interpenetration is allowed only between the soft shells, while the hard cores are impenetrable. Frequently, studies considering spheres (Torquato, 2002) and spherocylinders (Berhan and Sastry, 2007; Mathew et al., 2012; Schilling et al., 2015) have been developed.

In the formalism of the continuum percolation, the behaviour of the system is discussed in terms of object density (Torquato, 2002). The volume fraction of one of the phases that composes the system finds correspondence in the occupation probability defined in the discrete percolation. Consequently, the percolation threshold represents the critical volume fraction at which a spanning cluster appears.

Continuum percolation studies have become increasingly frequent in literature since they create a bridge between the mathematical approach and properties of discrete percolation and realistic models of heterogeneous materials, namely porous media, composite materials or colloids (Rintoul and Torquato, 1997). Continuum percolation is used to describe phenomena in physics, chemistry, biology, communication and traffic networks. It was applied to systems at different length scales, from the elementary particles to cosmological systems. Typical applications encompass the study of electrical properties in porous media, semi- and super- conductors, nanotubes in composites, analysis of chemical and biological networks, bioinformatics and ecological systems. Analysis associated with rheological properties, such as permeability, viscosity and related phenomena, i.e. diffusion, drainage, have also been considered. Continuum percolation was applied also for the study of elastic, dielectric and magnetic properties.

Computer simulations of systems that undergo percolating behaviour is mainly a two-step process. First, random distributions of particles, e.g. spheres, ellipsoids, rods, have to be generated in

a simulation domain, e.g. cubic box. Subsequently, a connectedness criterion has to be established, depending on the physical or mathematical context. For instance, two elements are assumed to be connected if they overlap (when considering 2D studies), interpenetrate (when considering 3D studies) or if they have a contact point in the case of models with non-overlapping particles. Second, each configuration is tested for the presence of a system-spanning cluster and then an average over a sufficiently large number of realizations is performed.

The system of particles can be realized by means of random sequential addition process or Metropolis algorithm. The random sequential addition process consists in randomly, irreversibly and sequentially adding objects into a volume. In the simplest approach, the particles are treated as fully penetrable (Lin et al., 2018), while other studies (Schilling et al., 2015), in association also with the physical background, developed a more realistic implementation by considering also the impenetrable core of the particles. In the last scenario, the random insertion is modified by rejecting any trial insertions that cause an overlap or intrusion with particles already placed in the simulation box. It is worth pointing out that the random sequential addition process for fully non-penetrable particles is characterized by a relevant limitation as outlined by Miller (2009). Although the random sequential addition process appears to be a random process, the allowable positions for particles added later in the simulation box are increasingly limited. The density above which new particles cannot be inserted is below that of dense structure obtained by random packing via Metropolis algorithm since the particles inserted earlier have created unemployable space (Miller, 2009; Sherwood, 1997). Therefore, the random sequential addition method does not capture all properties of the system because it does not produce configurations that have no hard-core overlap with equal probability.

A method to overcome the aforementioned issue is to create the particle configurations by using the Metropolis algorithm (Metropolis et al., 1953), in which the particles start in an arbitrary, regular configuration and then are subjected to random displacements, each accepted if the overlapping criteria are satisfied.

The assessment of percolation threshold depends on the connectivity conditions considered, as well as the geometrical characteristics of the objects, i.e. aspect ratio, volume size of the simulation domain.

Among methodological articles that studied different aspects of the continuum percolation theory, it is worth mentioning Lee and Torquato (1988), Mathew et al. (2012) and Schilling et al. (2015). Lee and Torquato (1988) have developed one of the first computer simulation for continuum percolation 2D models. The Authors set their model as constituted of disks of diameter σ and

encompassed by a perfectly penetrable concentric shell of thickness λ. The extreme limits of λ, i.e. $\lambda = 0$ and $\lambda = \sigma$ correspond to totally impenetrable and fully penetrable disks, respectively. The study aimed to determine the percolation threshold of the 2D system of particles as well as other characteristics of the formed clusters, e.g. mean cluster size and pair-connectedness function. Mathew et al. (2012) and Schilling et al. (2015) have performed MC simulations on the percolation behaviour of hard core -soft shell ellipsoids and spherocylinders, respectively, in 3D continuum systems. Their simulations provided insights concerning the influence of 3D objects aspect ratio on the percolation threshold.

There is a small amount of studies in literature that consider the percolation theory in association with phenomena in biological tissues. For instance, Genin et al. (2009) justify the results of an investigation developed at the attachment of tendon to bone in rats by introducing the concept of percolation threshold. The outcomes of the finite element model suggest that increase in mineral accumulation within collagen fibres can provide significant stiffening of the partially mineralized fibres, but only for concentrations of mineral above a ‘‘percolation threshold’’ corresponding to the formation of a mechanically continuous mineral network within each collagen fibre (Genin et al., 2009). In line with the study of Genin et al. (2009), Liu and co-workers (2013) estimate the mechanical behaviour of partially mineralized collagen fibrils, that occurs at the tendon to bone insertion. They considered several sequences of apatite arrangement at the collagen fibril scale and assessed the mineral - dependent tissue mechanics. They highlight that the stiffening of the tissue exhibits a percolation-like behaviour.

The aforementioned methodological aspects lead to the conclusion that the discrete percolation approach cannot represent in an appropriate manner real systems. Moreover, also the development of soft-core models applying the continuum percolation may not reflect adequately heterogenous and complex boundary conditions. To move towards a more accurate representation of real materials, some studies have developed 3D models composed of hard-core with soft shell particles. However, these analyses still represent an idealized system since some simplifying assumptions have been introduced. For instance, the particles aspect ratio is kept constant for all particles in the simulation box, while in real systems a size distribution associated with particles is observed. Furthermore, in other investigations has not been taken into account the variation of the particle orientation, which is also noticed in real systems.

4.1.3 Aim of the study

In this study, the complexity of the MCF is reduced by considering an idealised continuum 3D model of apatite crystals within the MCF. However, several aspects of the real structure of bone tissue at nanoscale have been maintained. As it was mentioned in the previous section, most 3D continuum percolation studies consider constant dimensions of the particles within the simulation box. Conversely, in this study it is assumed a variable geometric size for the apatite crystals, in agreement with experimental observations (Rubin et al., 2003). Moreover, differently from percolation models available in literature that consider cubic simulation box, in this model it is considered a cylindrical box that better mimics the shape of the real MCF.

The representation of the underlying atomic structure is beyond the scope of this work. The orientation of the apatite mineral in the range ± 20 degree with respect to the longitudinal axis of the collagen fibril corresponds to the initial conditions of the percolation theory. The latter analyses the cluster formation in systems composed of disordered objects (Torquato, 2002). Conversely, the tropocollagen molecules compose an ordered matrix (Orgel et al., 2006), parallel to the MCF long axis. Considering the arrangement within the MCF, the objective of this study is to estimate the feasibility that the apatite minerals could be characterized by a percolation-like behaviour. Moreover, the water component is omitted in this investigation, since the predominant factor on the mechanical and structural behaviour of MCF is the mineral content, rather than water (Fielder et al., 2019).

4.2 METHODS

4.2.1 Initial configuration of mineral within the MCF

The MCF is represented by a cylindrical volume, which length L_{MCF} and diameter D_{MCF} are in agreement with experimental data concerning the morphological characterization of the fibril (Wagermaier et al., 2015; Buehler, 2006). In human bone tissue, collagen fibrils typically have a diameter between 50 nm and 200 nm (Wagermaier et al., 2015) and a length in the order of 1000 nm (Buehler, 2006). In this study, the continuum percolation theory was applied to MCF models characterized by two different values of D_{MCF}, namely 50 nm and 200 nm.

The mineral shape observed from experimental studies (Rubin et al., 2003) is that of thin elongated platelets. The organization of these crystals is usually illustrated in literature according to the model of 3D deck of cards arrangement in which the platelets lie almost parallel throughout the collagen fibril (Fratzl et al., 2004). According to (Hodge and Petruska, 1963; Jäger et al., 2000) the mineral arrangement has a staggered structure in the longitudinal direction of the collagen fibril and parallel layers in the equatorial plane of the MCF.

Initially a starting configuration of apatite platelets within the MCF was developed. Specifically, the centroids of the apatite platelets are placed in correspondence of the sites of a staggered prismatic lattice within the cylinder of volume V_{MCF} (Figure 4.2). The length, width and thickness axes of the crystals are initially perfectly aligned with the axes L, W and T of a global coordinate system (CS). The equatorial plane of the MCF is identified by W and T axes.

The geometry of the staggered prismatic lattice was developed following the model of apatite organization proposed by Jäger et al. (2000). The staggered pattern is obtained by considering a periodic length (D_{period}) of 67 nm between adjacent sites in longitudinal direction. In the equatorial plane, the lattice sites are created in order to allow the insertion also of the platelets with the highest VF, according to the range available in Literature for mineral crystal dimensions (Rubin et al., 2003).

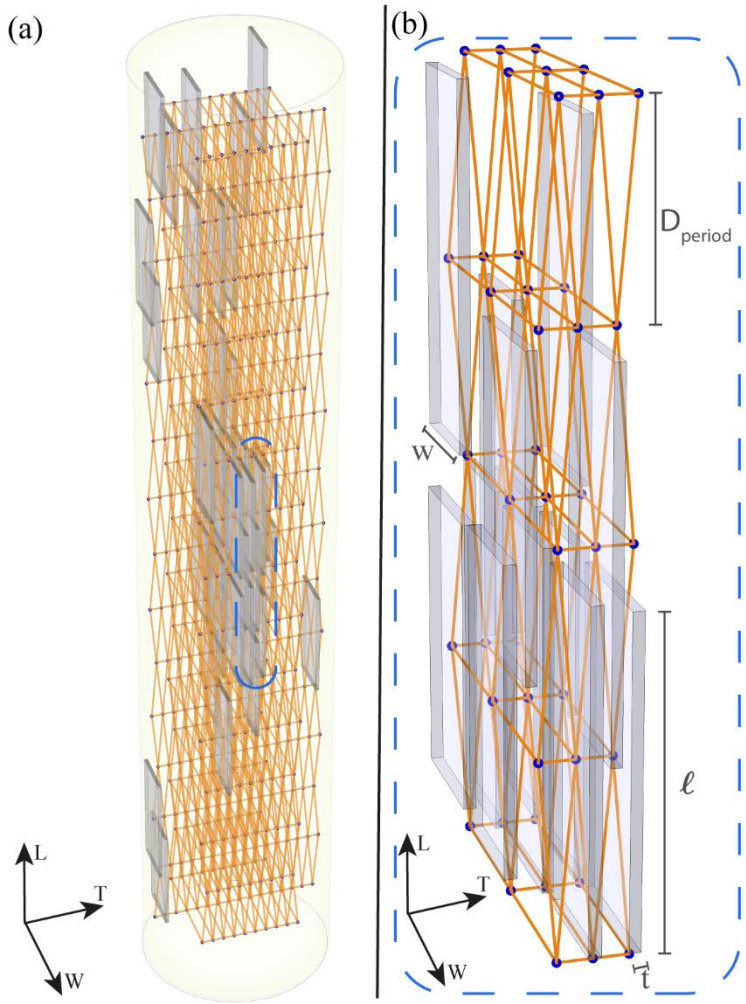

Figure 4.2: (a) Representation of the staggered prismatic lattice (orange) used for the generation of the starting configuration for the 3D apatite model (grey). The centroids (blue dots) of apatite platelets are placed in correspondence of the lattice sites (b). The configuration of mineral platelets is initialized by occupying the lattice sites randomly.

It is assumed that the maximum number of aligned platelets with the coordinate system that may be incorporated in the MCF in the width direction is three. Similarly, in the T direction the number of platelets that is considered in the MCF diameter of 50 nm and 200 nm is maximum 8 and 32 respectively. Thus, it was made the assumption that the distance between the lattice sites in the width direction is 14 nm and 55 nm for the MCF diameter of 50 nm and 200 nm, respectively. Analogously, it is considered a distance of 5.4 nm and 5.9 nm between the lattice nodes in the thickness direction for the MCF with 50 nm and 200 nm diameter, respectively.

Thus, according to the geometric conditions previously mentioned, the total number of sites is 136 for the MCF with 50 nm diameter and 526 for the MCF with 200 nm diameter. The configuration of apatite platelet is initialized by occupying the lattice sites randomly. The apatite minerals are represented as parallelepipeds with variable geometric dimensions. The sizes of the platelets are obtained by means of random extraction from Gaussian Probability Density Functions, following the ranges reported in Literature (Wagermaier et al., 2015; Rubin et al., 2003; Weiner et al., 1986). For each MCF diameter, it was performed an analysis of ten different mineral volume fractions (VF): from low (7 percent) to high (52 percent) mineralization degrees with steps of 5 percent. The mineral VF is calculated according to Eq. (4.1):

$$VF = \frac{\ell \cdot w \cdot t}{(\ell + a_L) \cdot (w + a_W)(t + a_T)} \tag{4.1}$$

where ℓ, w, t are the length, width and thickness of the apatite platelet, a_L, a_W and a_T are the distances between the platelets in the longitudinal, width and thickness direction.

The algorithm that generates the array of mineral platelets with a specific VF is developed in order to verify whether the extracted dimensions of the platelets fit the geometrical constraints of the lattice sites and do not occupy more space than that reserved to a single node. If the platelet that is generated has higher size than the allowed space, the dimensions are rejected and a new random extraction from the Gaussian Probability Density Functions is performed for all variables. The algorithm ends when all lattice nodes are occupied with apatite platelets characterized by a specific VF. In Table 4.1 a concise pseudo-code of the algorithm associated with the generation of the initial configuration is reported.

Table 4.1. Pseudo-code for the generation of the initial apatite array

Algorithm 1

Input: mean and standard deviation of Gaussian Probability Density Functions for platelets dimensions (ℓ, w, t)

Mineral volume fraction (VF_t)

Number of platelets in the MCF

Geometric dimensions of the lattice sites

While there are lattice sites unoccupied **do**

1. Random extraction of the index of the lattice site to be occupied
2. Random extraction of w, t, ℓ value from Gaussian Probability Density Functions
3. Calculation of platelets interdistance a_L, a_W, a_T

   $a_L = 2D_{period} - \ell$

   $a_W = w_{sites} - w$

   $a_T = t_{sites} - t$
4. Assessment of mineral volume fraction (vf) (Eq. 4.1)
5. **If** $a_W < 0$ **or** $a_T < 0$, **then** Go to step 2
6. **If** $vf < (VF_t - 0.0005)$ **or** $vf > (VF_t + 0.0005)$, **then** Go to step 2
7. **Save** the dimensions of the new platelet

end

Output: array of the geometrical dimensions of the apatite platelets and their position in the lattice grid.

4.2.2 Generating configurations

For each value of mineral VF that characterizes the MCF of 50 nm and 200 nm, the Metropolis algorithm (Torquato, 2002) has been utilised to generate configurations of the mineral phase. The initial configurations described in the previous section represent the starting point of the algorithm. The gist of the algorithm consists in the construction of a new configuration from the given realization. Following the implementation described by Torquato (2002) for a given configuration, each mineral is moved by displacing it along each axis by random amounts chosen from a uniform distribution in the interval [-τ; τ], where τ is the maximum step size. Subsequently, the platelet is reoriented by rotating it around each axis by amounts extracted from a Gaussian probability distribution function with mean 0 degrees and standard deviation θ, where θ is the maximum inclination size. The new perturbed position of the platelet is accepted if it does not cause an interpenetration superior than 10 percent of apatite platelet volume or if it does not go outside the tolerance cylinder. It is introduced a tolerance cylinder with dimensions 5 percent greater than the MCF cylinder in order to allow also the peripheral platelets to achieve an inclination in agreement with the range available in Literature (Georgiadis et al., 2016; Bini et al., 2017; Bini et al., 2019; Xu et al., 2020), i.e. around ± 20 degrees. Otherwise, the move is rejected and the actual position of the apatite is maintained. All platelets are in turn moved according to these criteria. One Monte Carlo cycle, or realization, involves trial translation and rotation around the three axes of the coordinate system for all mineral platelets within the MCF model.

An important methodological aspect that should be noticed is that the displacement and orientation parameters influence the performance of the algorithm. In this study, the acceptance ratio method has been implemented (Hebbeker et al., 2016). The acceptance ratio (AR) is determined by the ratio between the number of translated and rotated apatite platelets (n_{TR}) and the number of total platelets (n_{HA}) within the MCF for a given configuration:

$$AR = \frac{n_{TR}}{n_{HA}} \tag{4.2}$$

It consists in adaptively changing the parameters associated with the displacement τ and orientation θ at every Monte Carlo cycle. Small perturbations imply large correlations between old and new configurations and a high acceptance ratio. Conversely, large perturbations lead to overlapping apatite platelets that reduce the acceptance ratio and deteriorate the usefulness of the

simulation. Traditionally, the perturbations are tuned in order to achieve a specific acceptance ratio. A common rule of thumb is to choose the magnitude of the maximum translational and rotational perturbations, i.e. τ and θ respectively, such that the acceptance ratio is in the range of 20 percent to 50 percent, even though there is no theoretical foundation for this rule (Frenkel et al., 2002). In fact, empirical studies on different systems have found optimal acceptance ratio ranging from 5 percent to 70 percent (Hebbeker et al., 2016).

In this study, the magnitudes of the maximum translational and rotational perturbations, i.e. τ and θ respectively, are adjusted at every Monte Carlo cycle in order to maintain the acceptance ratio of trial moves and rotations close to 50 percent (Torquato, 2002). If at the end of a Monte Carlo cycle the acceptance ratio is greater than 50 percent, the values of τ and θ are incremented by 10 percent of their actual value. Conversely, if the acceptance ratio is inferior or equal to 50 percent, the values of τ and θ are decreased by 10 percent of their actual value. The new values of τ and θ are used in the successive Monte Carlo cycle.

Another aspect that it is worth commenting is the percentage of interpenetration between two apatite platelets. As mentioned in the Introduction of this Chapter, few data concerning the growth and fusion of apatite crystals are available. Initially, a test study was performed in order to analyse the influence of this parameter on the configurations developed. Two different values for the interpenetration between mineral platelets, namely 5 percent and 10 percent of the apatite volume were considered. The test was performed for MCF with a diameter of 50 nm and with high degree of mineralization, i.e. 42 percent.

It was observed that after a high number of displacements and rotations, the acceptance ratio reaches the constant value of 50 percent for the case with an interpenetration between platelets up to 5 percent of the apatite volume (Figure 4.3 a). In terms of displacements, this acceptance ratio led to decreasing the maximum translational perturbation, i.e. τ, at every Monte Carlo cycle (Figure 4.3 c). Thus, successive configurations were highly correlated and the Metropolis algorithm became inefficient. This outcome finds a justification in the small percentage of platelets interpenetration allowed. The majority of apatite platelets reach the maximum percentage of intruded volume after a relatively reduced number of Monte Carlo cycles. The successive attempts of translational and rotational perturbations are rejected since the interpenetration condition is not satisfied. Consequently, the number of rotated and translated platelets is inferior to 50 percent and this leads to a decrease of the maximum displacement τ. Therefore, ever smaller maximum displacements values will rarely produce acceptable perturbations that may increase the acceptance ratio.

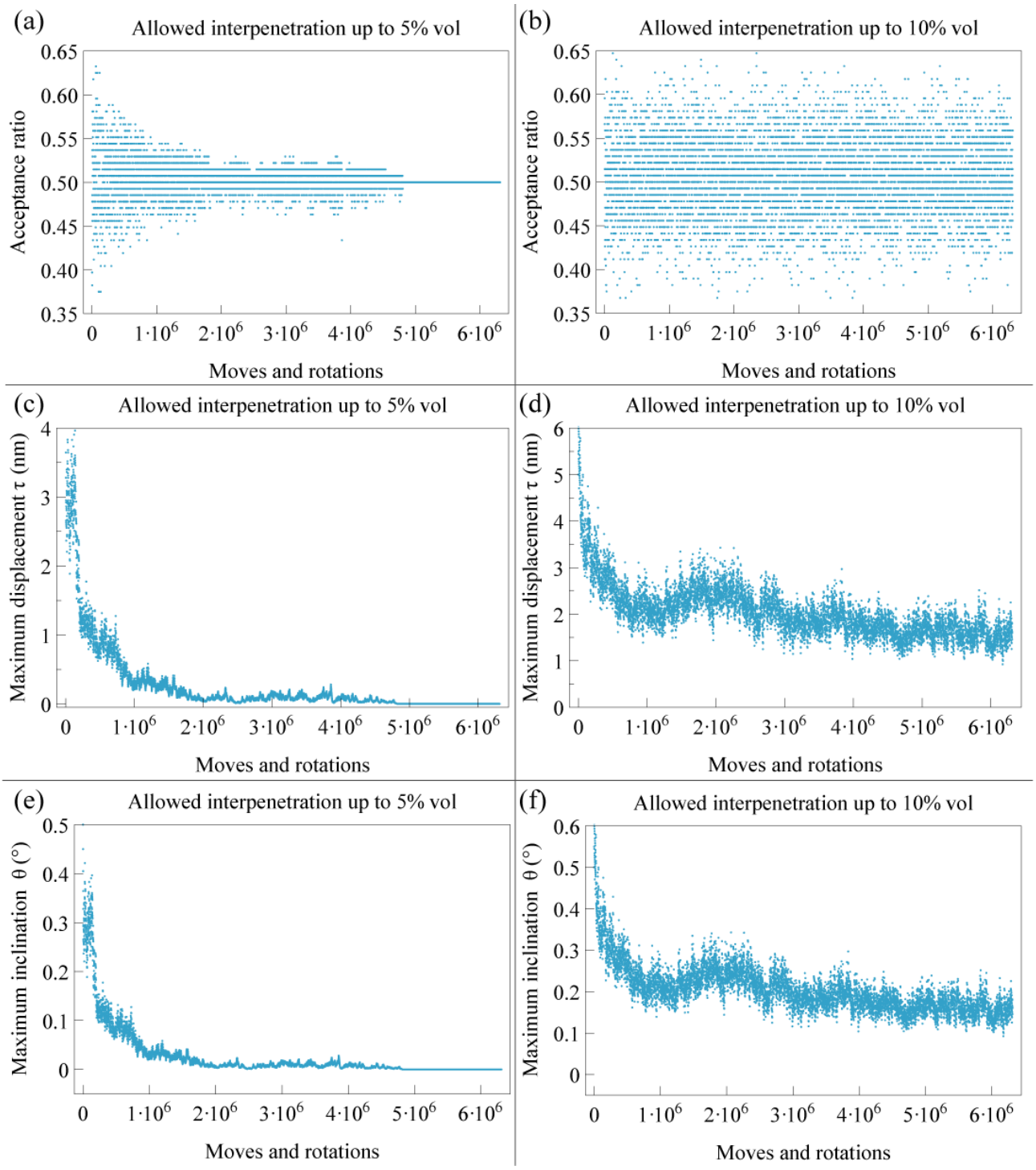

Figure 4.3: Comparison of acceptance ratio of perturbed platelets, maximum displacement and inclination factors between configurations realized with two interpenetration conditions of mineral platelets, i.e. allowed interpenetration up to 5 percent (a, c, e) and up to 10 percent (b, d, f) of platelet volume.

Conversely, the intrusion up to 10 percent of apatite volume showed a dynamic trend for the acceptance ratio (Figure 4.3 b, d,f). Although decreasing displacements can be seen in correspondence of the maximum number of Monte Carlo cycles, its value does not lead to inefficient configurations.

The selection of this parameter value is one of the main assumptions considered in this study. The first value considered, i.e. an interpenetration condition up to 5 percent of platelet volume is based on a statistical approach, but it leads to an instability of the Metropolis algorithm as discussed previously. The test study showed that the algorithm becomes stable for an interpenetration condition of up to 10 percent of the apatite volume. Further studies concerning an increased percentage of interpenetrating volume have not been performed since the aim of the present investigation is to analyse the structure in the early stage of apatite fusion (Landis et al., 1993).

4.2.2.1 Detection of interpenetrating platelets

An algorithm for the detection of interpenetrating platelets was implemented by adapting the geometrical method of Lin et al. (2018). The algorithm can be summarised by the following steps:

(a) Consider that a platelet A_i is randomly displaced and oriented within the MCF and its centroid is identified by the coordinates (w_{i_c}, t_{i_c}, ℓ_{i_c}). To speed up the algorithm, an exploring volume centred in correspondence of the A_i platelet centroid and aligned with the CS is considered following the suggestion of Newman and Ziff (2001). The dimension of the exploring volume along the W axis is equal to the MCF diameter, along T axis is ten times the average thickness of apatite platelets, i.e. $T_{average}$ = 3.5 nm (Wagermaier et al., 2015; Rubin et al., 2003), and along L axis is equal to 30 percent of the MCF length. Thus, the interpenetration detection algorithm is applied to the platelets whose centroids belong to the exploring volume.

(b) The identification of the nearest point (p_j) of each platelet within the exploring volume (e.g. platelet A_j) to the centroid of the platelet A_i is performed. The point p_j is obtained by means of a gradient based method that minimizes the Euclidean norm between the two points:

$$d_n = Min\sqrt{\left(w_{i\_c} - w_j\right)^2 + \left(t_{i\_c} - t_j\right)^2 + \left(\ell_{i\_c} - \ell_j\right)^2} \tag{4.3}$$

where (w_j, t_j, ℓ_j) are the coordinates of the nearest point of the platelet A_j to the centroid of the platelet A_i.

(c) The projection of the distance between the centroid of the platelet A_i and the point p_j identified at step (b) along the three axes of the CS is calculated:

$$\Delta d_W = \left| w_{c\_i} - w_{p_j} \right| \tag{4.4}$$

$$\Delta d_T = \left| t_{c\_i} - t_{p_j} \right| \tag{4.5}$$

$$\Delta d_L = \left| \ell_{c\_i} - \ell_{p_j} \right| \tag{4.6}$$

(d) If the following conditions are simultaneously meet, an interpenetration between A_i and A_j occurs for more than 10 percent of A_i volume and the move is rejected:

$$\begin{cases} \Delta d_W < \dfrac{w}{2} - 10\% w \\ \Delta d_T < \dfrac{t}{2} - 10\% t \\ \Delta d_L < \dfrac{\ell}{2} - 10\% \ell \end{cases} \tag{4.7}$$

(e) Platelets can interpenetrate when two conditions of relation (4.7) are verified. For these scenarios, the spatial positions of vertices of platelets A_i and A_j are analysed. It is assumed that the edges of platelet A_j that interpenetrate the platelet A_i could not cross the whole crystal thickness. Therefore, the move is rejected if one of conditions 4.8 - 4.13 are met. Assuming that vertex m indicates a vertex of the lower base of the platelets and vertex n indicates a vertex of the upper base of the platelets, the relations 4.8 – 4.9 are expressed as follows:

$$\begin{cases} \text{t component of Vertex m of platelet } A_j < \text{ t component of Vertex m of platelet } A_i \\ \text{t component of Vertex n of platelet } A_j > \text{ t component of Vertex n of platelet } A_i \end{cases} \tag{4.8}$$

$$\begin{cases} \text{t component of Vertex m of platelet } A_j > \text{ t component of Vertex m of platelet } A_i \\ \text{t component of Vertex n of platelet } A_j < \text{ t component of Vertex n of platelet } A_i \end{cases} \tag{4.9}$$

$$\text{Number of Vertices of } A_i \text{ lower base that are internal to platelet } A_j > 2 \tag{4.10}$$

$$\text{Number of Vertices of } A_i \text{ upper base that are internal to platelet } A_j > 2 \tag{4.11}$$

$$\text{Number of Vertices of } A_j \text{ lower base that are internal to platelet } A_i > 2 \tag{4.12}$$

$$\text{Number of Vertices of } A_j \text{ upper base that are internal to platelet } A_i > 2 \tag{4.13}$$

(f) If none of the above conditions is verified, the attempted move and rotation are accepted.

An outline of the algorithm is given in Table 4.2.

Table 4.2. Pseudo-code for Metropolis algorithm

Algorithm 2

Input: initial maximum displacement (τ) and inclination (θ) along the three axes L, W, T
Number of platelets in the MCF
Number of Monte Carlo cycles

While the number of iterations is smaller than the number of Monte Carlo cycles **do**

While there are platelets within the MCF not considered, **do**

Assume that the platelet *i* is under investigation
Find platelets near platelet *i*
Random extraction of the displacement along the three axes L, W, T
Random extraction of the inclination with respect to the three axes, i.e. θ_{LT}, θ_{WT}, θ_{LW}
Check for interpenetration situations following steps (c)-(f) in Section 4.2.2.1
If the platelet *i* in the new position intrude another platelet for more than 10 percent of the apatite crystal volume, reject the move
else, accept the move
end if
Save the new MCF configuration

end

Determine acceptance ratio (AR)

If AR ≤ 0.5, **then** $\tau = \tau - 0.1 \cdot \tau$; $\theta = \theta - 0.1 \cdot \theta$,
else $\tau = \tau + 0.1 \cdot \tau$; $\theta = \theta + 0.1 \cdot \theta$
end if

end

Output: configurations of the apatite platelets within the MCF.

4.2.3 Equilibrium

Equilibrium is monitored by computing average measures as Radial Distribution Function (RDF) and the nematic order parameter (S). After the equilibration, other perturbations have been performed to sample the probability that the system contains long-range connected networks.

4.2.3.1 Radial distribution function

The radial distribution function $g_2(r)$ is a powerful tool used to analyse the complex 3D distribution of the apatite platelets position. The RDF is obtained as a normalization of the local density of platelets at a given distance r from a given reference platelet to the overall mineral crystal density in the volume. This measurement is widely used to characterize packing structure and reveals information about their organization.

The platelets density (ρ) in the cylindric volume is obtained from Eq. 4.14 as the ratio between the number of platelets in the MCF, i.e. n_{HA}, and the MCF volume, i.e. V_{MCF}.

$$\rho = \frac{n_{HA}}{V_{MCF}} \tag{4.14}$$

The local density is determined considering the number of platelets in concentric shells with finite thickness Δr that are at a distance comprises between $(r - \frac{\Delta r}{2}, r + \frac{\Delta r}{2})$ from the reference platelet divided by the shell volume. The cylindrical geometry of the MCF has been taken into account by considering concentric spherical shells in the equatorial plane and elliptic shells in the longitudinal direction (Figure 4.4).

In the equatorial plane, the volume of the spherical shell of thickness Δr is obtained as follows:

$$V_{shell\ EQ}(r, \Delta r) = \frac{4}{3}\pi \left[\left(r + \frac{\Delta r}{2} \right)^3 - \left(r - \frac{\Delta r}{2} \right)^3 \right] \tag{4.15}$$

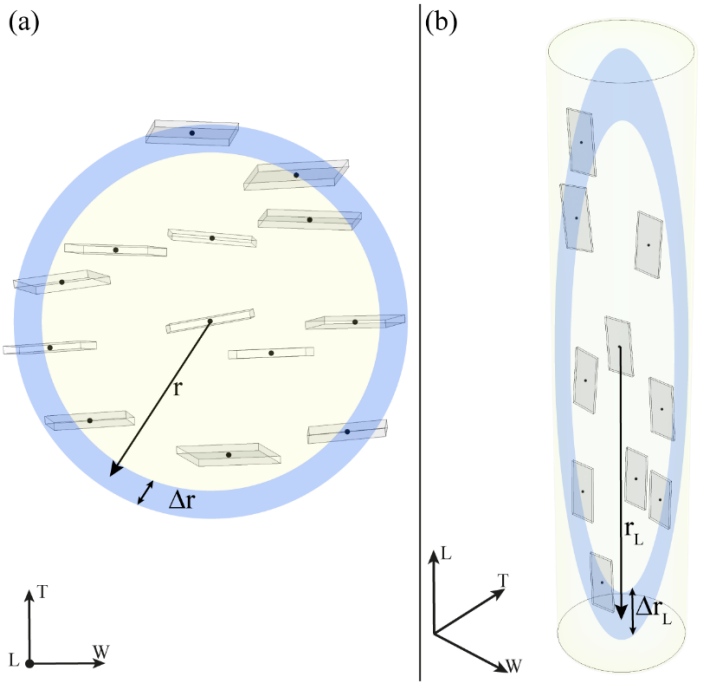

Figure 4.4: Spherical (a) and ellipsoidal (b) shells used in the algorithm of the radial distribution function in the equatorial plane and longitudinal direction, respectively. The black points represent the centroids of the platelets (grey) at equilibrium within the MCF with a diameter of 200 nm. The distance r represents the distance from the reference platelet, while Δr is the shell thickness.

In the longitudinal direction an elliptic shell with thickness Δr_W in W direction, Δr_T in T direction and Δr_L in L direction is considered. The shell volume is achieved as:

$$V_{shell\,L}(r) = \frac{4}{3}\pi\left[\left(r_W + \frac{\Delta r_W}{2}\right)\cdot\left(r_T + \frac{\Delta r_T}{2}\right)\cdot\left(r_L + \frac{\Delta r_L}{2}\right) - \left(r_W - \frac{\Delta r_W}{2}\right)\cdot\left(r_T - \frac{\Delta r_T}{2}\right)\cdot\left(r_L - \frac{\Delta r_L}{2}\right)\right] \tag{4.16}$$

The largest shell radius is limited in the equatorial plane to half MCF diameter and in the longitudinal direction to half MCF length. For a given mineral VF, the distance between the centroids of all pair of mineral platelets from all of the generated configurations is computed. The finite volume of the system leads to an artificially decay to 0 of the RDF for large radii (Figure 4.5). To avoid this effect, periodic boundary conditions are implemented in the three spatial directions, so that the simulation volume is surrounded by images of itself (Torquato et al., 2002).

The pairwise separations are then sorted into a histogram in which each bin has width Δr.

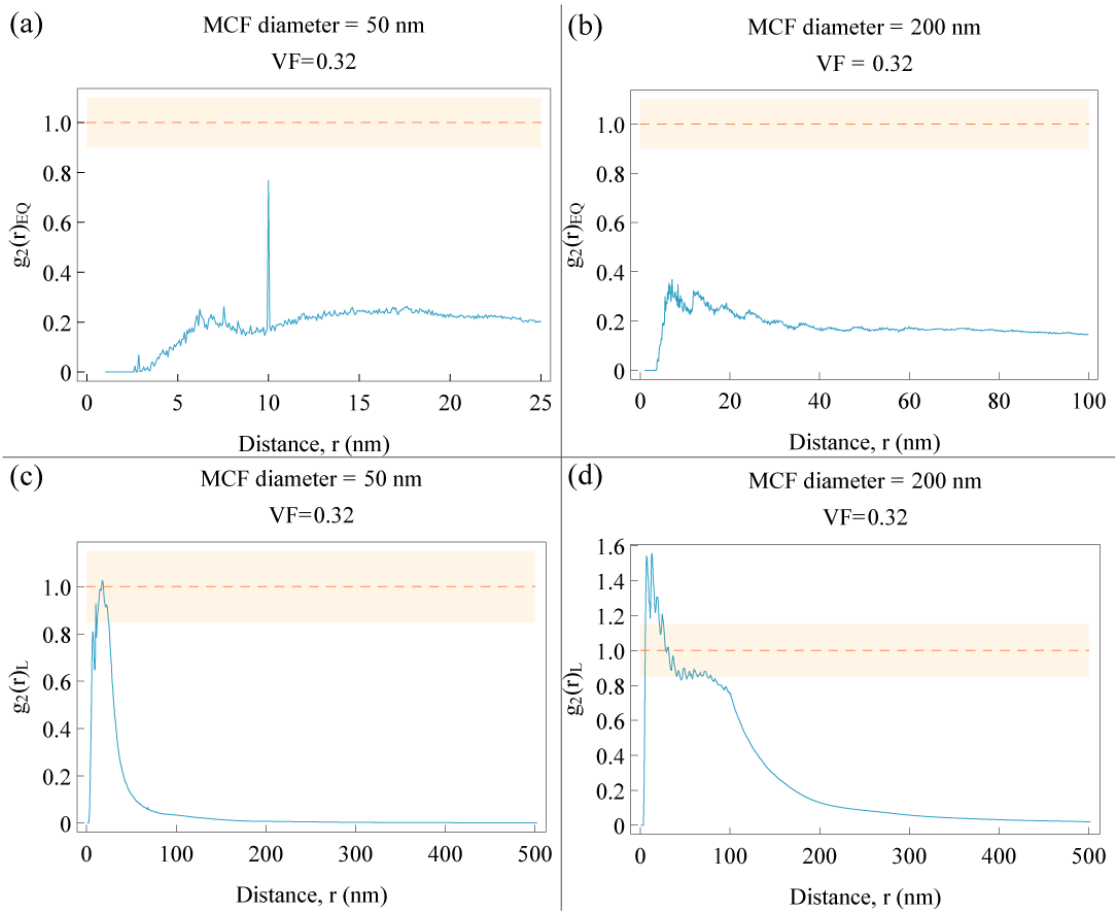

Figure 4.5: Typical plot highlighting the artificial decay of the Radial distribution function $g_2(r)$ for large interplatelets distance r in the equatorial plane (a, b) and in longitudinal direction (c, d) due to the boundaries of the finite sample volume. The RDF is computed for an equilibrium configuration of platelets at 32 percent mineral VF within the MCF characterized by a diameter of 50 nm (a, c) and 200 nm (b, d), without taking into account periodic boundaries conditions.

The average number of platelets, i.e. n(r), whose distance from a given reference platelet lies in the interval $(r - \frac{\Delta r}{2}, r + \frac{\Delta r}{2})$ is given by:

$$n(r) = \frac{n_k(r)}{M \cdot n_{HA}} \tag{4.17}$$

where $n_k(r)$ represents the number of platelets contained in the bin k of the histogram corresponding to the distance r and M is the total number of configurations.

Therefore, the RDF for a particular value of r is obtained from Eq. (4.18):

$$g_2(r, \Delta r) = \frac{1}{\rho} \cdot \frac{n(r)}{V_{shell}(r)} \tag{4.18}$$

The RDF is a normalized density of the platelets relative to the average density of the system under investigation. An RDF value of unity describes that the density at a radial distance r is equal to the average density of the system.

The RDF is a local measure of how close the particle arrangement is to a distribution where all particle locations are equally like (Younge et al., 2004). The condition of RDF equal to 1 implies that the probability of finding a particle in the shell $V(r+\Delta r)$ is the same as would be obtained if the particles would be uniformly distributed (Younge et al., 2004).

Therefore, RDF is expected to reach constant values at the equilibrium. For instance, in Figures 4.6 and 4.7 the RDF plots for a mineral VF of 7 percent, 32 percent, 42 percent and 52 percent within the MCF of 50 nm and 200 nm diameter, respectively are depicted. It should be noticed that the apatite configurations with increased mineral volume fractions have radial distribution functions characterized by increasingly pronounced deviations from $g_2(r) = 1$ at smaller distances. The larger peak is due to the contribution of platelets in contact and this observation justifies the increment of the peak height with mineral VF. In fact, a platelet in a low VF condition relatively rarely interacts with another particle in the system. Thus, the distribution of minerals could be considered nearly uniform and justifies the observed trend for RDF (Figures 4.6 - 4.7). The oscillatory behaviour for high VF implies an alternation between high and low probability of finding platelets at a certain distance r.

However, for all mineral VF, the system has reached the equilibrium when the $g_2(r)$, for large distances approaches 1 (Torquato, 2002), specifically it is in a range (0.9;1.1). This condition is identified after roughly $2.1 \cdot 10^6$ moves and rotations.

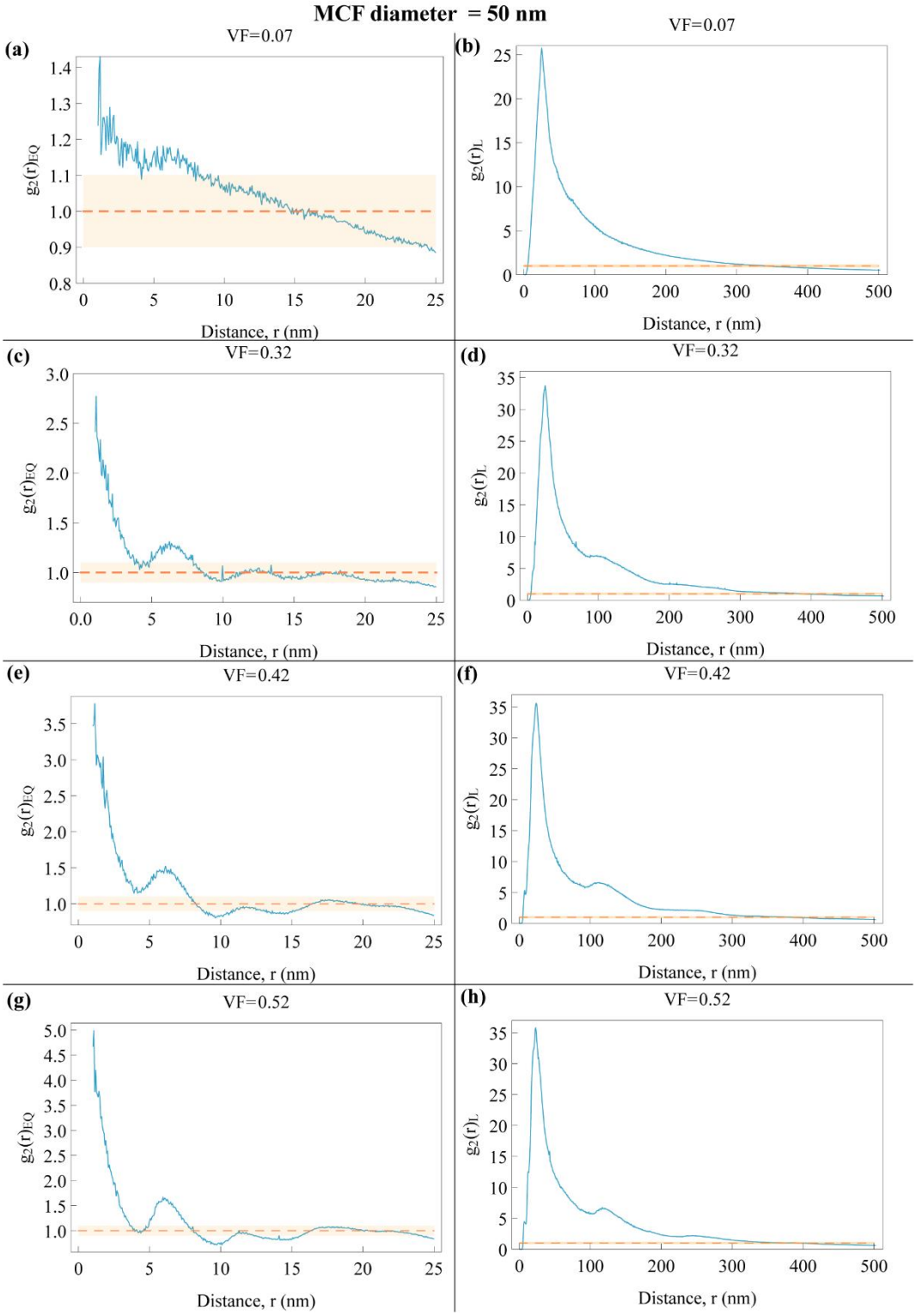

Figure 4.6: Radial distribution function $g_2(r)$ in function of interplatelets distance r in the equatorial plane (a, c, e, g) and in longitudinal direction (b, d, f, h) for an equilibrium configuration of platelets at 7 percent (a, b), 32 percent (c, d), 42 percent (e, f) and 52 percent (g, h) of mineral VF within the MCF characterized by a diameter of 50 nm.

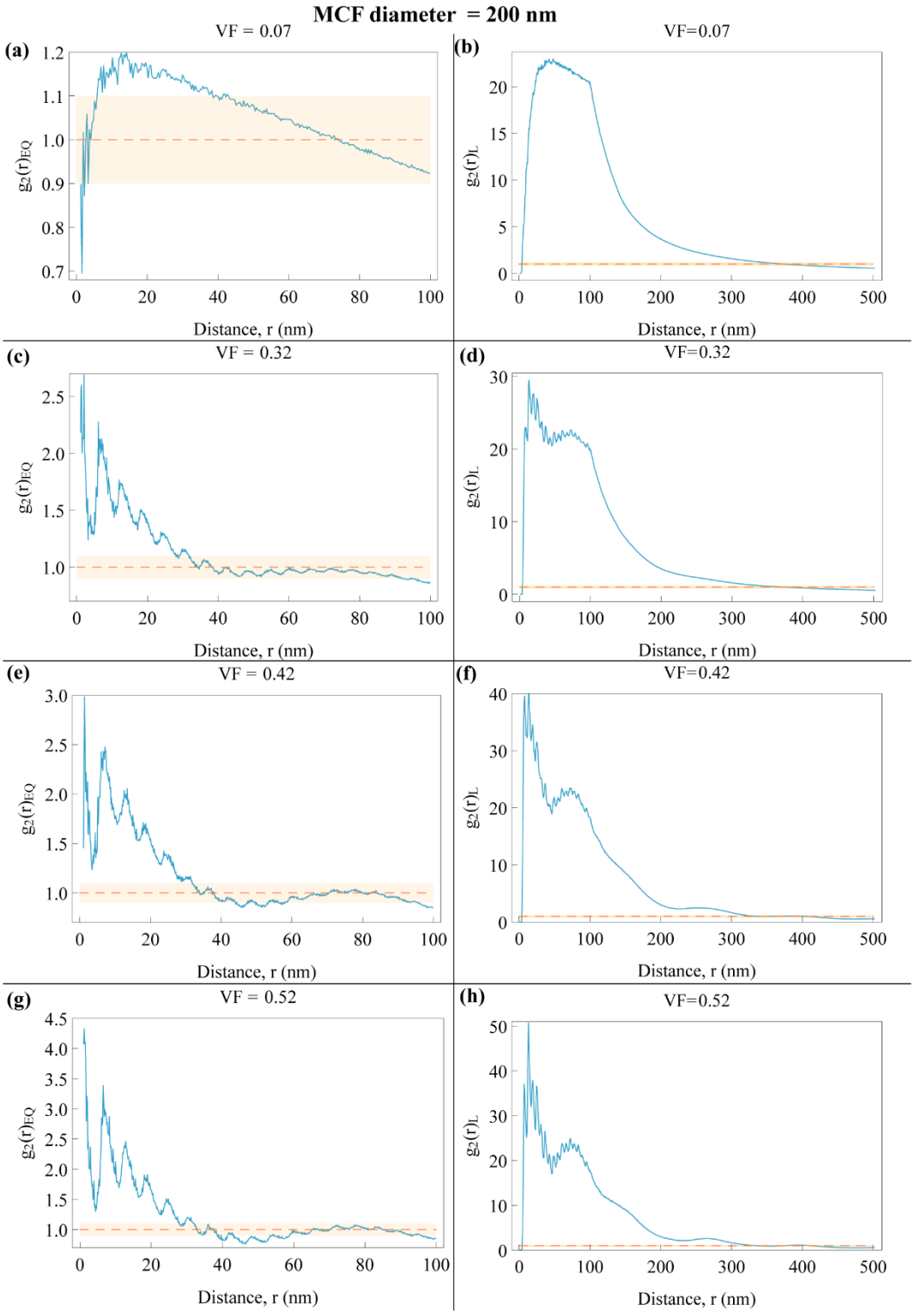

Figure 4.7: Radial distribution function $g_2(r)$ in function of interplatelets distance r in the equatorial plane (a, c, e, g) and in longitudinal direction (b, d, f, h) for an equilibrium configuration of platelets at 7 percent (a, b), 32 percent (c, d), 42 percent (e, f) and 52 percent (g, h) of mineral VF within the MCF characterized by a diameter of 200 nm.

4.2.3.2 Nematic order parameter

For a given realization, the nematic order parameter S is obtained as the maximum eigenvalue of the tensor Q defined as follows (De Gennes, 1993):

$$\boldsymbol{Q} = \frac{1}{n_{HA}} \cdot \sum \frac{3}{2} \cdot u_{\alpha} \cdot u_{\beta} - \frac{1}{2}\boldsymbol{I} \tag{4.19}$$

where n_{HA} is the number of platelets within the fibril, u_{α} u_{β} are the component of the unit vector u parallel to the longitudinal axis of the platelet, with α and β = L, W, T are indices referring to the absolute coordinate system and I is the identity matrix.

The nematic order parameter provides information about the alignment of apatite platelets. In a fully aligned configuration S is unity, while in an isotropic case S is zero. In this case, after roughly $2.1 \cdot 10^6$ moves and rotations, i.e. the equilibrium state identified by the RDF, S remains in a narrow range (0.98; 1) reflecting the morphological constraint of roughly aligned platelets to the c-axis of the collagen fibril (Georgiadis et al., 2016). In Figure 4.8, the nematic order parameter for the mineral VF, i.e. 7 percent, 32 percent 42 percent and 52 percent for both MCF diameters are illustrated. Although the variation of S is on the order of magnitude of 10^{-3}, it is worth pointing out that the value of S at the equilibrium is higher for increased apatite VF. This implies that mineral platelets in hypermineralized conditions have little space to change their orientation.

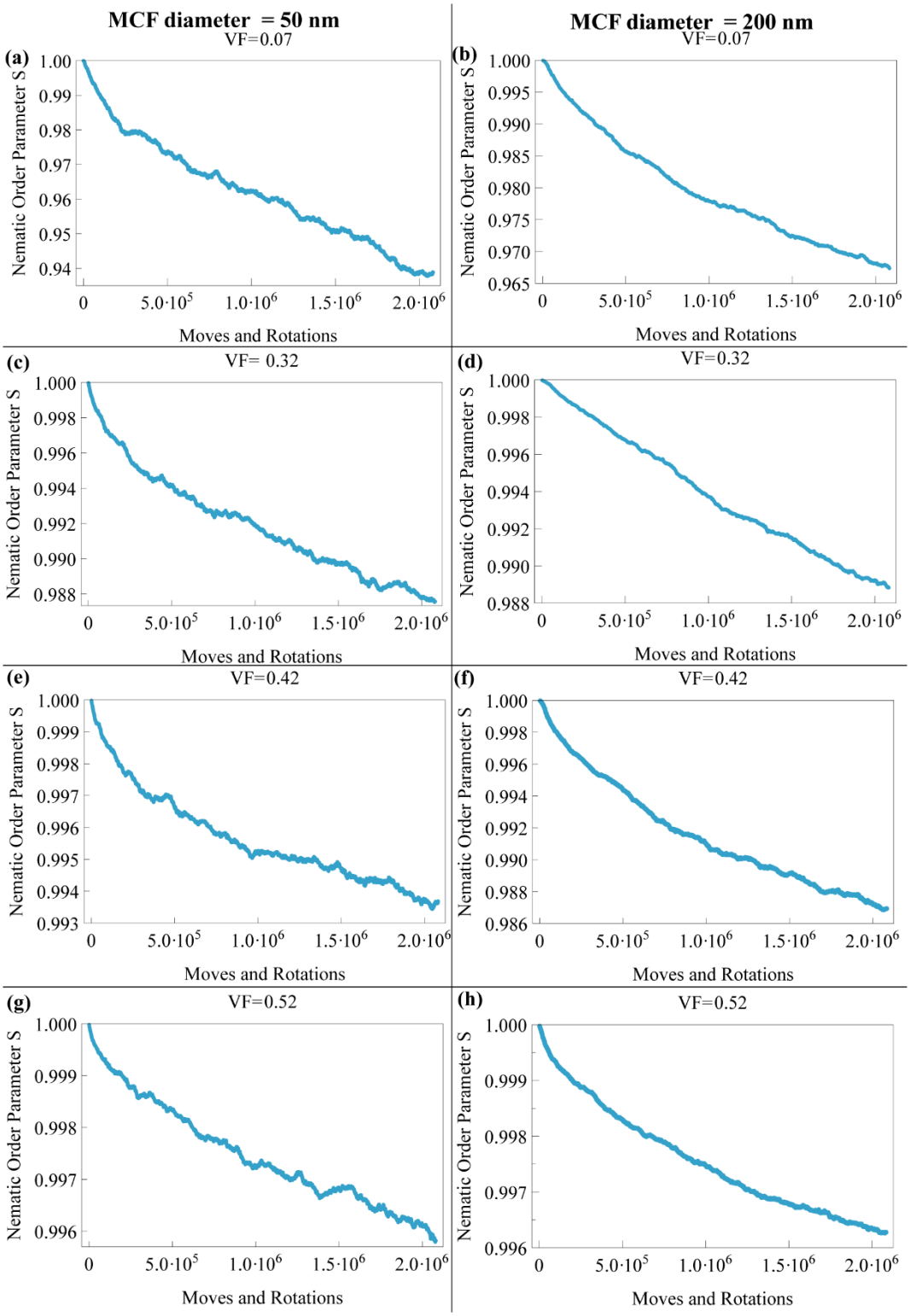

Figure 4.8: Nematic order parameter calculated for mineral volume fraction of 7 percent (a, b), 32 percent (c, d), 42 percent (e, f) and 52 percent (g, h) within the mineralized collagen fibril with diameter of 50 nm (a, c, e, g) and 200 nm (b, d, f, h).

4.2.4 Cluster identification

After the equilibration, there were performed another overall $4.2 \cdot 10^6$ displacements and rotations per platelets for each mineral VF of both MCF diameters to sample the probability that the system contains long-range connected networks. It is worth mentioning that the number of moves and rotations considered for each mineral VF is highly superior to the number of iterations performed in other studies. For instance Mathew at al. (2012) and Schilling et al. (2015) considered overall $1 \cdot 10^6$ moves per particle, while in the present study there were generated overall $6.3 \cdot 10^6$ displacements and rotations, subdivided among equilibration, i.e. $2.1 \cdot 10^6$ displacements and rotations per platelets, and successive sampling, i.e. $4.2 \cdot 10^6$ displacements and rotations per platelets.

According to Literature (Torquato et al., 2002; Schilling et al., 2015), in this study it was assumed the same number of overall moves and rotations for both MCF of 50 nm and 200 nm diameter, respectively. A Monte Carlo cycle corresponds to perform trial translations and rotations around the three axes of the coordinate system for all mineral platelets within the MCF model associated to a mineral VF. One Monte Carlo cycle is characterized, therefore, by 816 trial moves and rotations for the MCF of 50 nm diameter since it is composed of 136 platelets and by 3156 trial moves and rotations for the MCF of 200 nm diameter since it is composed of 526 platelets. Each Monte Carlo cycle generates a new configuration of the MCF. Thus, the overall movements and rotations performed, i.e. $6.3 \cdot 10^6$ displacements and rotations, generate 7735 configurations of the apatite minerals for the MCF with 50 nm diameter and 2000 configurations for the MCF with 200 nm diameter.

The cluster analysis is performed using the configurations obtained after the equilibrium for all mineral VF within the MCF of 50 nm and 200 nm diameter, respectively. Therefore, the analysis is carried out on the last 5185 configurations of the MCF with 50 nm diameter and on the last 1340 configurations of the MCF with 200 nm diameter.

The identification of groups of connected platelets within the MCF is adapted from the tree-based union find algorithm proposed by Newman and Ziff (2001). The first part of the algorithm determines the pairs of platelets that respect a previously set connectivity criterion and subsequently all minerals that form a cluster are identified.

The connectivity criterion is determined from the minimum distance d between two platelets as obtained from the minimisation problem (Eq. 4.20):

$$d = Min\sqrt{\left(w_i - w_j\right)^2 + \left(t_i - t_j\right)^2 + \left(\ell_i - \ell_j\right)^2} \tag{4.20}$$

where (w_i, t_i, ℓ_i) are the coordinates of p_i which is a point of the platelet A_i and (w_j, t_j, ℓ_j) are the coordinates of p_j which is a point of platelet A_j. The equation is solved by means of a gradient based method that minimizes the Euclidean norm between the points p_i and p_j.

To determine connected platelets, the minimum distance should be calculated between each platelet and every other platelet in the MCF. However, a strategy reported by Newman and Ziff (2001) and Torquato (2002) have been applied to increase the speed of the algorithm and reduce computational costs. Therefore, only the distances between the reference platelet and the mineral crystals which centroids are confined in an exploring volume (Torquato, 2002) are computed. The latter is generated by assuming the same geometrical values as for the exploring volume considered in the algorithm associated to platelet interpenetration.

Two platelets are identified as connected if their minimum distance is smaller than a threshold value. In this analysis, two threshold values have been investigated. Initially, the cut-off distance associated with long range electrostatic interactions between minerals is considered. From the studies of Wang et al. (2013) and von Euw et al. (2018) a distance δ = 14 Å is considered. This distance represents the thickness of the mineral hydrated layers (Combes et al., 2016). Therefore, the clusters generated with this assumption are composed by apatite platelets connected by means of their hydrated layers (Figure 4.9 a).

Thus, two platelets are connected if the following relation is valid:

$$0 < d \leq \delta \tag{4.21}$$

Secondly, the same mineral configurations are analysed assuming the connectivity criterion expressed by Eq. 4.22:

$$d = 0 \tag{4.22}$$

In this case, the connection occurs if the platelets interpenetrate each other, i.e. the minimum distance is null since the points p_i and p_j identified by the minimum distance algorithm coincide (Figure 4.9 b).

The pairwise platelets identified applying the above-described connectivity conditions represent the input data for the cluster identification algorithm. The cluster information is obtained using a data tree structure. Each platelet is identified by an index which is considered as the vertex of a graph. In this manner, the pair of platelets obtained from the previous step represent the endpoints

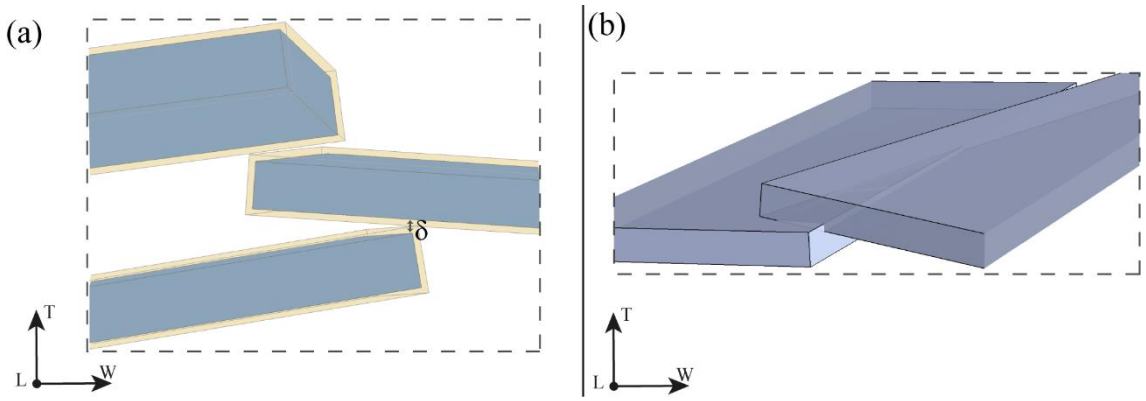

Figure 4.9: In (a) illustration of a group of connected platelets that verify the connectedness criterion based on the cut off distance δ = 14 Å of long-range interactions between minerals is represented. Apatite platelets (blue-grey regions) are covered by a shell (yellow) of thickness δ/2 that mimics the long-range interactions which occur between apatite crystals due to their hydrated layers. In (b) a representation of a group of interpenetrating platelets is depicted.

of the graph edges. The union/find algorithm (Newman and Ziff, 2001) applied to each configuration leads to identify the groups of platelets that are connected to one another.

4.2.5 Percolating cluster assessment

A cluster is defined as percolating if it spans the simulation domain in a determined direction from one boundary to the opposite one (Torquato, 2002). In this analysis, the spanning clusters are identified by taking into account the anisotropic arrangement of apatite minerals within the MCF. Thus, percolation paths are researched along the three main directions of the coordinate system, i.e. W, T, L (Figures 4.10 and 4.11).

The percolating clusters are determined applying an algorithm that compares the position of the platelets that form each cluster with the boundaries of the MCF. The approach can be outlined as follows:

(a) For each cluster, the vertices of its platelets are identified.

(b) It is made the assumption that spanning clusters in the equatorial plane should have several vertices of the platelets outside a circumference of diameter equal to 90 percent of the MCF diameter.

(b.1) For each selected cluster, the minimum (w_{min}) and maximum (w_{max}) coordinates of the vertices along W direction are identified and the corresponding distance d_W is achieved as follows:

$$d_W = w_{\max} - w_{\min} \tag{4.23}$$

In order to take into account the cylindrical geometry of the simulation domain, in W direction it was made the assumption that the clusters are percolating if their length d_W is greater or equal to the chord length $W_{percolation}$:

$$d_W \geq W_{percolation} \tag{4.24}$$

In post processing analysis, it was observed that the system follows the percolative behaviour (Torquato, 2002) when clusters composed by more than four platelets are considered. Thus, a minimum chord length of 50 nm and 120 nm for the MCF diameter of 50 nm and 200 nm respectively is assumed.

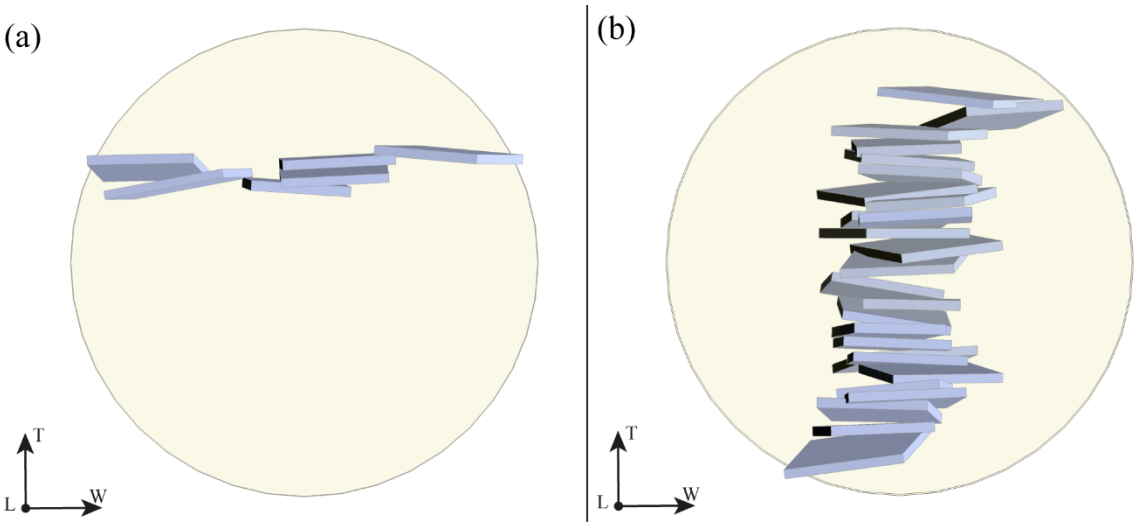

Figure 4.10: Typical clusters spanning the mineralized collagen fibril of 200 nm diameter in the equatorial plane, namely in W direction (a) and T direction (b). Depicted clusters are composed of interpenetrating platelets.

(b.2) For each selected cluster the distance in T direction is determined as the difference between the maximum (t_{max}) and minimum (t_{min}) coordinates of the vertices (Eq. 4.25).

$$d_T = t_{\max} - t_{\min} \tag{4.25}$$

Apatite clusters are percolating in T direction if the following relation is valid:

$$d_T \geq T_{percolation} \tag{4.26}$$

From the post-processing analysis, the apatite systems highlight percolative characteristics whether the minimum chord length $T_{percolation}$ is equal to 25 nm and 50 nm for the MCF diameter of 50 nm and 200 nm, respectively.

This first analysis aims to identify percolating clusters in at least one orthogonal direction of the Equatorial plane, i.e. W or T direction, indistinctly. Therefore, a subsequent verification algorithm is developed related to the WT plane. Specifically, for each MC cycle, i.e. attempt to move and rotate all mineral platelets of the MCF, associated to a mineral VF, a check is performed to establish whether spanning clusters occurs in W or T direction or both directions. If the MC realization has spanning clusters in both directions of the Equatorial plane, the largest percolating clusters is selected to be used in the statistical analysis.

(c) In the longitudinal direction, the analysed clusters have the characteristic that could span a MCF of reduced length, according with recent high resolution tomographic data (Reznikov et al., 2018). Therefore, for each cluster identified in step **(a)** the minimum (ℓ_{min}) and maximum (ℓ_{max}) coordinates of the vertices along the L direction are considered to compute the distance:

$$d_L = \ell_{\max} - \ell_{\min} \tag{4.27}$$

The clusters that verify the condition are therefore selected:

$$d_L \geq L_{cluster} \tag{4.28}$$

where $L_{cluster}$ is equal to 300 nm and 450 nm for the MCF diameter of 50 nm and 200 nm respectively. These thresholds are frequent values of MCF length individuated experimentally in the study of Reznikov et al. (2018).

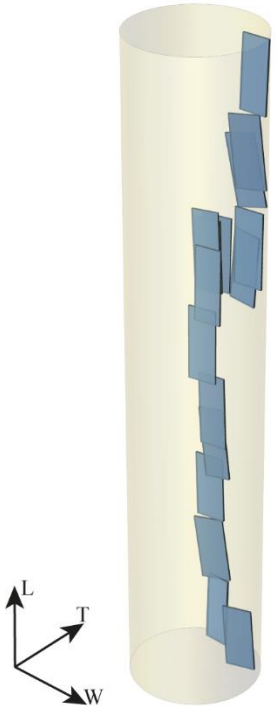

Figure 4.11: Typical cluster spanning the mineralized collagen fibril of 200 nm diameter in the longitudinal direction. Depicted cluster is composed of interpenetrating platelets.

In addition, the analysis for clusters that span the MCF from an extremity to the opposite one in the longitudinal direction is also performed. In this case, the clusters from step **(a)** with coordinates of vertices along L direction that are outside a cylinder of length equal to 950 nm, i.e. 95 percent length of the MCF have been identified.

4.3 RESULTS

In this study, the percolation behaviour in a 3D model of the MCF characterized by two different diameters, namely 50 nm and 200 nm, is investigated. To explore the percolative properties of the matrix of apatite mineral within the MCF, an analysis of the cluster statistics is performed on the MCF configurations developed after the equilibrium. It can occur that a configuration of the MCF relative to a mineral VF, might be characterized by multiple percolating clusters in the Equatorial plane or in the Longitudinal direction. For the analysis presented in this study, in these cases, the largest group of connected platelets has been considered in the Equatorial plane and in the Longitudinal direction, according to Torquato (2002), Schilling et al. (2015), Garboczi et al. (1995). The maximum number of percolating clusters for a specific mineral VF is equal to the number of MCF configurations analysed, namely 5185 for the MCF with 50 nm diameter and 1340 for the MCF with 200 nm diameter.

Figures 4.12 – 4.17 show histograms that report the percentage of percolating clusters as a function of cluster size, i.e. number of platelets that compose a percolating network, at each mineral VF over the MCF realizations generated after the equilibrium. When considered statistically relevant also the cumulative plot indicating the total percentage of percolating clusters is reported. The assessment is performed on clusters that span the simulation volume in at least one orthogonal direction in the Equatorial plane (Figure 4.12, 4.14, 4.15). The outcomes reported for the longitudinal directions are obtained considering clusters that could span MCF of reduced length, as illustrated previously in Section 4.2.5. The analysis related to spanning clusters in the longitudinal direction of the entire length of the MCF is reported in the Appendix B (Figures B.11-B.13) since few mineral VF for both MCF diameters have developed connected networks that satisfy this condition.

Figure 4.12 and 4.13 show separately the outcomes associated with the mineral degree of 7 percent since, differently from higher mineralization degrees, in the low mineralized condition, percolating clusters have not been formed for all the conditions assessed. Namely, in the equatorial plane, percolating clusters of interpenetrating minerals were identified only for the 50 nm diameter MCF, while networks characterized by the cut off distance of long- range electrostatic interactions form spanning structures in MCF of 50 nm and 200 nm diameter. In the longitudinal direction, percolating clusters composed of interpenetrating platelets were not found neither for the MCF of 50 nm diameter nor in the MCF of 200 nm diameter. For both diameters, spanning clusters were identified assuming long-range interactions between minerals.

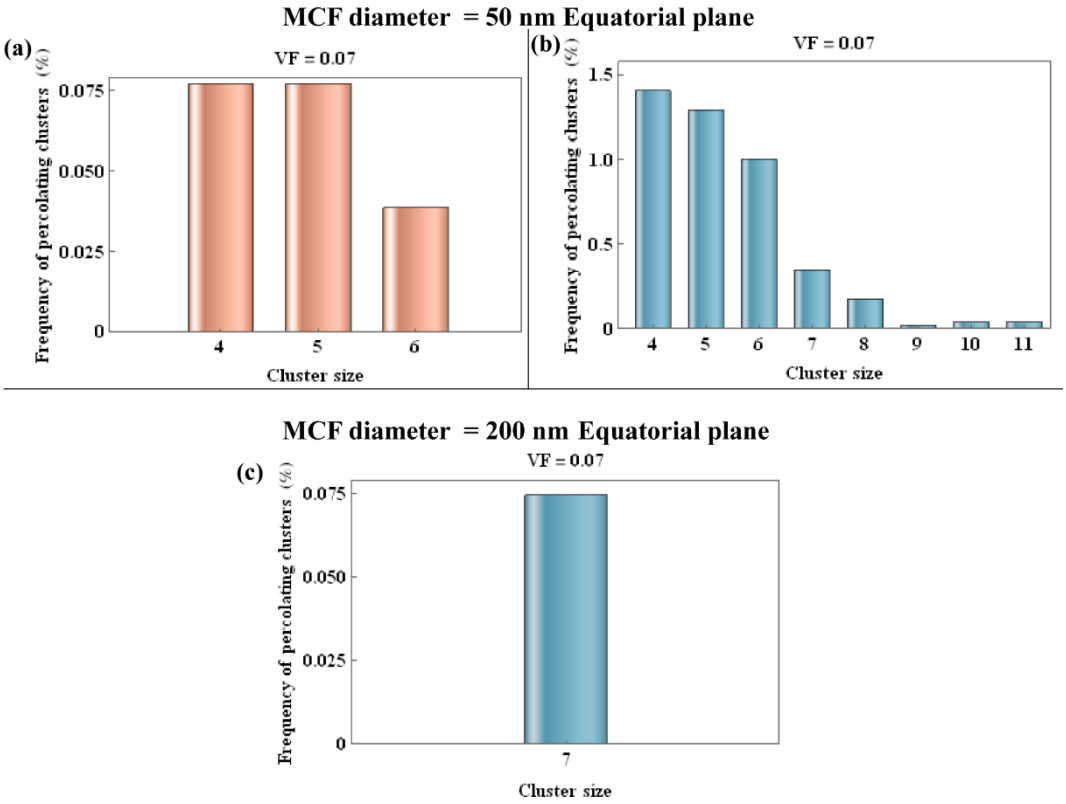

Figure 4.12: Frequency of percolating clusters (%) in function of cluster size, i.e. number of apatite platelets, for a mineral volume fraction of 7 percent in the equatorial plane of the mineralized collagen fibril (MCF) with diameter of 50 nm (a, b) and 200 nm (c). Clusters achieved assuming long-range interaction between minerals (blue) and interpenetrating crystals (light red) are reported. For the MCF of 200 nm diameter, percolating clusters composed of interpenetrating platelets were not found.

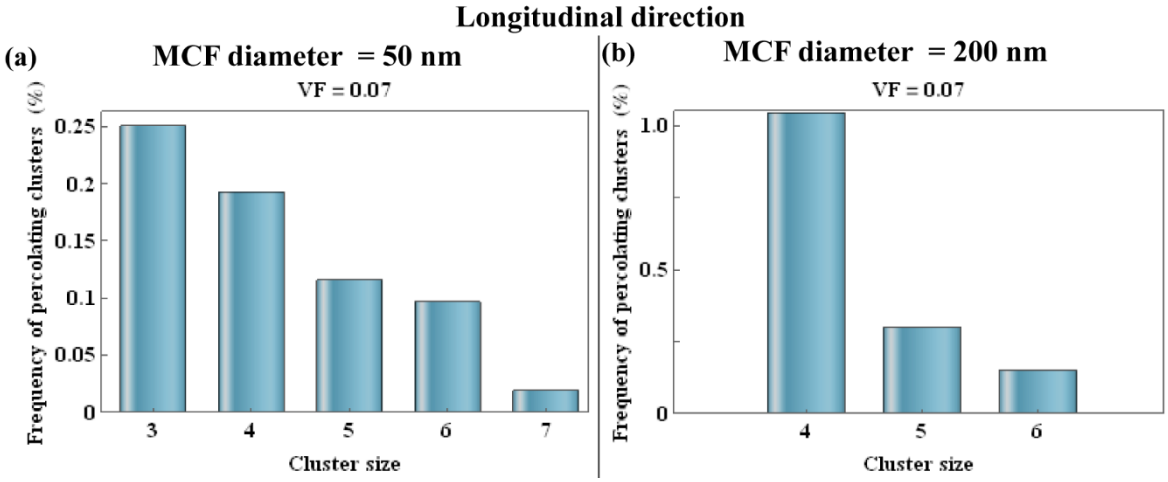

Figure 4.13: Frequency of percolating clusters (%) in function of cluster size, i.e. number of apatite platelets, for a mineral volume fraction of 7 percent in the longitudinal direction of the mineralized collagen fibril with diameter of 50 nm (a) and 200 nm (b). Spanning clusters were identified only assuming long-range interaction between minerals (blue); percolating clusters composed of interpenetrating platelets were not found.

Furthermore, in compliance with the results illustrated in the previous Chapter of this Thesis, in Figures 4.14- 4.17 the results are shown for mineral volume fraction of 32 percent, 42 percent and 52 percent. The cluster statistics concerning the remaining mineral VF conditions are reported in Appendix B.

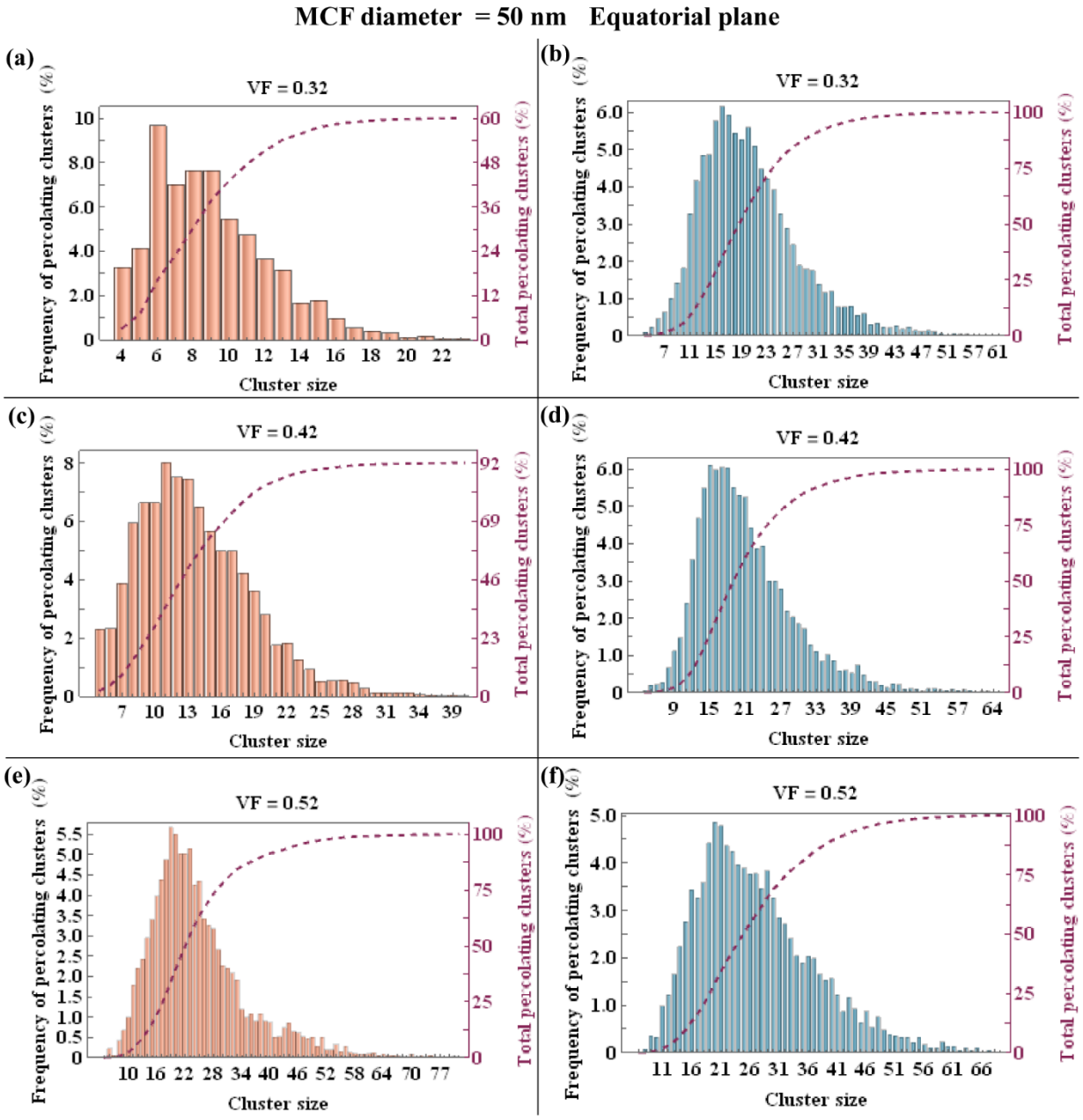

Figure 4.14: Frequency of percolating clusters (%) in function of cluster size, i.e. number of apatite platelets, for mineral volume fraction of 32 percent (a, b), 42 percent (c, d), and 52 percent (e, f) in the equatorial plane of the mineralized collagen fibril with diameter of 50 nm. The dark red curve represents the cumulative frequency (%) of percolating clusters. Clusters achieved assuming long-range interaction between minerals (blue) and interpenetrating crystals (light red) are reported.

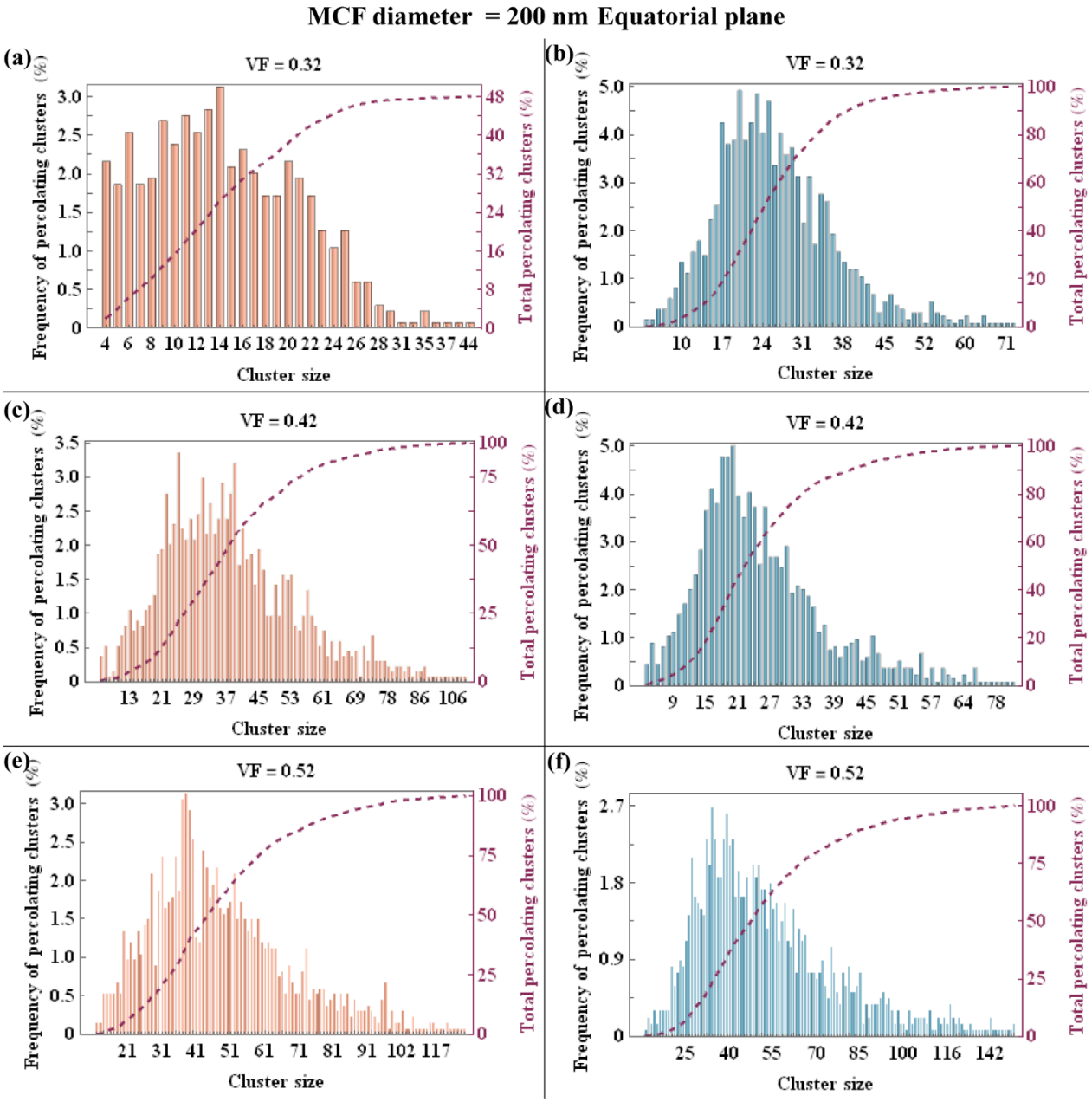

Figure 4.15: Frequency of percolating clusters (%) in function of cluster size, i.e. number of apatite platelets, for mineral volume fraction of 32 percent (a, b), 42 percent (c, d), and 52 percent (e, f) in the equatorial plane of the mineralized collagen fibril with diameter of 200 nm. The dark red curve represents the cumulative frequency (%) of percolating clusters. Clusters achieved assuming long-range interaction between minerals (blue) and interpenetrating crystals (light red) are reported.

4.4 DISCUSSIONS

The basic mechanism of bone mineralization, the arrangement and amount of mineral within the MCF represent controversial issues. Different methods have been applied to explore the influence of the apatite crystals on the properties of the MCF. A limited number of studies have highlighted that anomalous variation of mineral content may lead to a deleterious organization of the nanostructure with decreased mechanical properties (Depalle et al., 2016; Currey, 1969). This observation motivates the application of percolation theory to the MCF since this statistical physical tool describes spatial features and connectivity between the objects that compose a system.

In this Chapter, the feasibility of creating ensembles of structures that can mimic the architecture of the mineral matrix within bone nanostructure is studied. Subsequently, the characteristics of the system that may lead to connected networks of apatite mineral within the MCF are investigated. The junction of two mineral crystals to form a single crystal is referred as crystal fusion (Landis et al., 1993; Combes et al., 2016) and it is thought to introduce significative changes in the MCF mechanical behaviour influencing stress, shear or fracture strength (Landis et al., 1993).

The continuum percolation algorithms are adapted to the geometry of the MCF and allow the identification of spanning networks within the structure. The analysis of the percolating clusters is performed considering also the anisotropy of the apatite crystal arrangement within the MCF (Bini et al., 2017; 2019). Therefore, the statistical information concerning the network characteristics is achieved separately for spanning clusters in at least one of the orthogonal directions of the equatorial plane, i.e. W, T, and for percolating clusters in the longitudinal direction. Overall, the histograms reported in Figures 4.12- 4.17, show that the onset of apatite networks depends on the mineral VF. A general trend observed from Figures 4.12-4.17 highlights that the number of apatite platelets that form a cluster increases with the mineral content. In fact, at higher values of mineral VF the distance between platelets is reduced and thus, subsequently to random perturbations achieved with Metropolis algorithm, it is more likely to accomplish the connectedness criteria illustrated in Methods section. Smaller percolating clusters size is obtained for the connectedness condition of interpenetrating platelets.

Moreover, for each mineral VF, the percentage of configurations with the same size of percolating clusters shows similar values for both connectedness conditions assessed in this work.

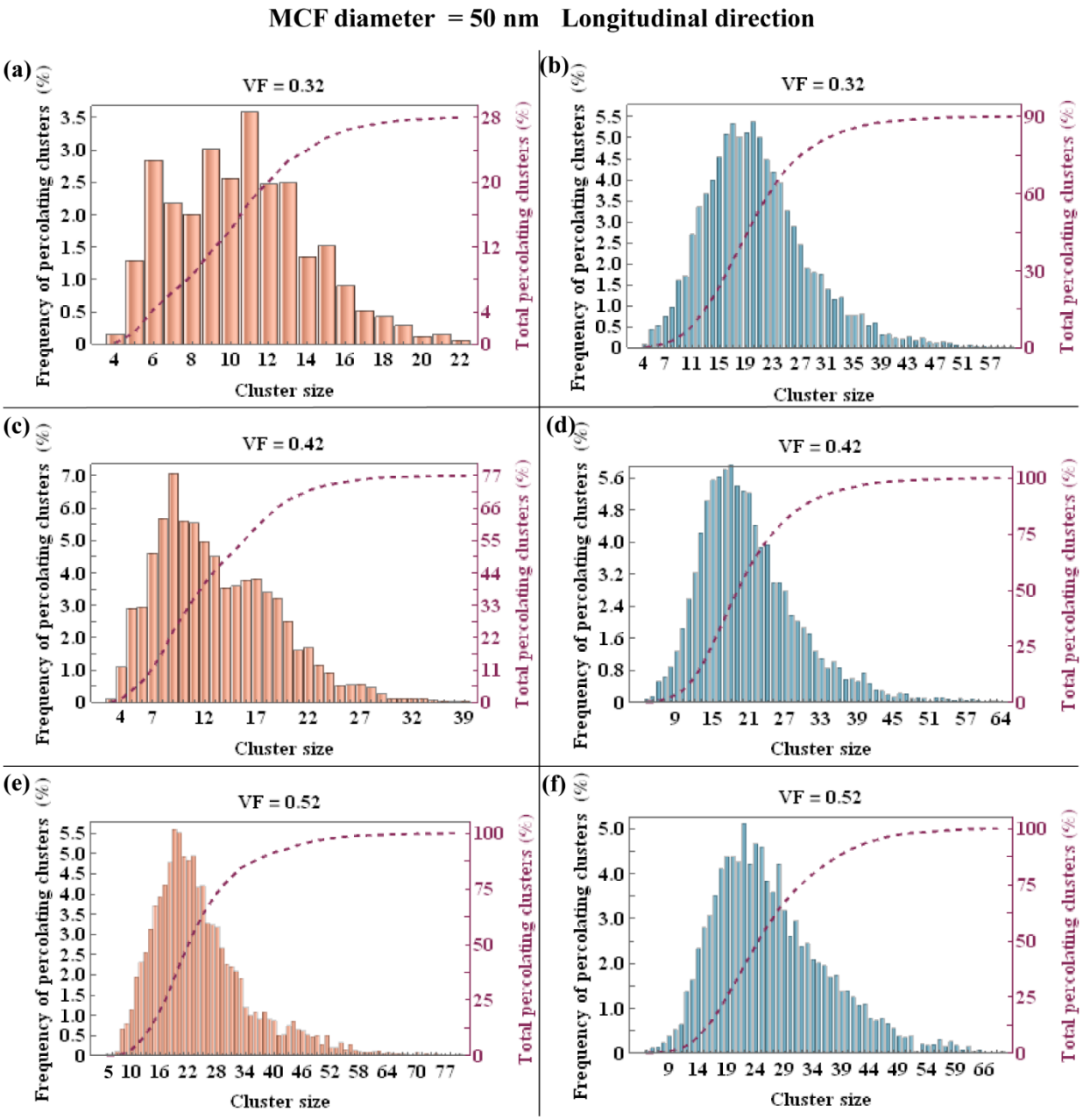

Figure 4.16: Frequency of percolating clusters (%) in function of cluster size, i.e. number of apatite platelets, for mineral volume fraction of 32 percent (a, b), 42 percent (c, d), and 52 percent (e,f) in the longitudinal axis of the mineralized collagen fibril with diameter of 50 nm. The dark red curve represents the cumulative frequency (%) of percolating clusters. Clusters achieved assuming long-range interaction between minerals (blue) and interpenetrating crystals (light red) are reported.

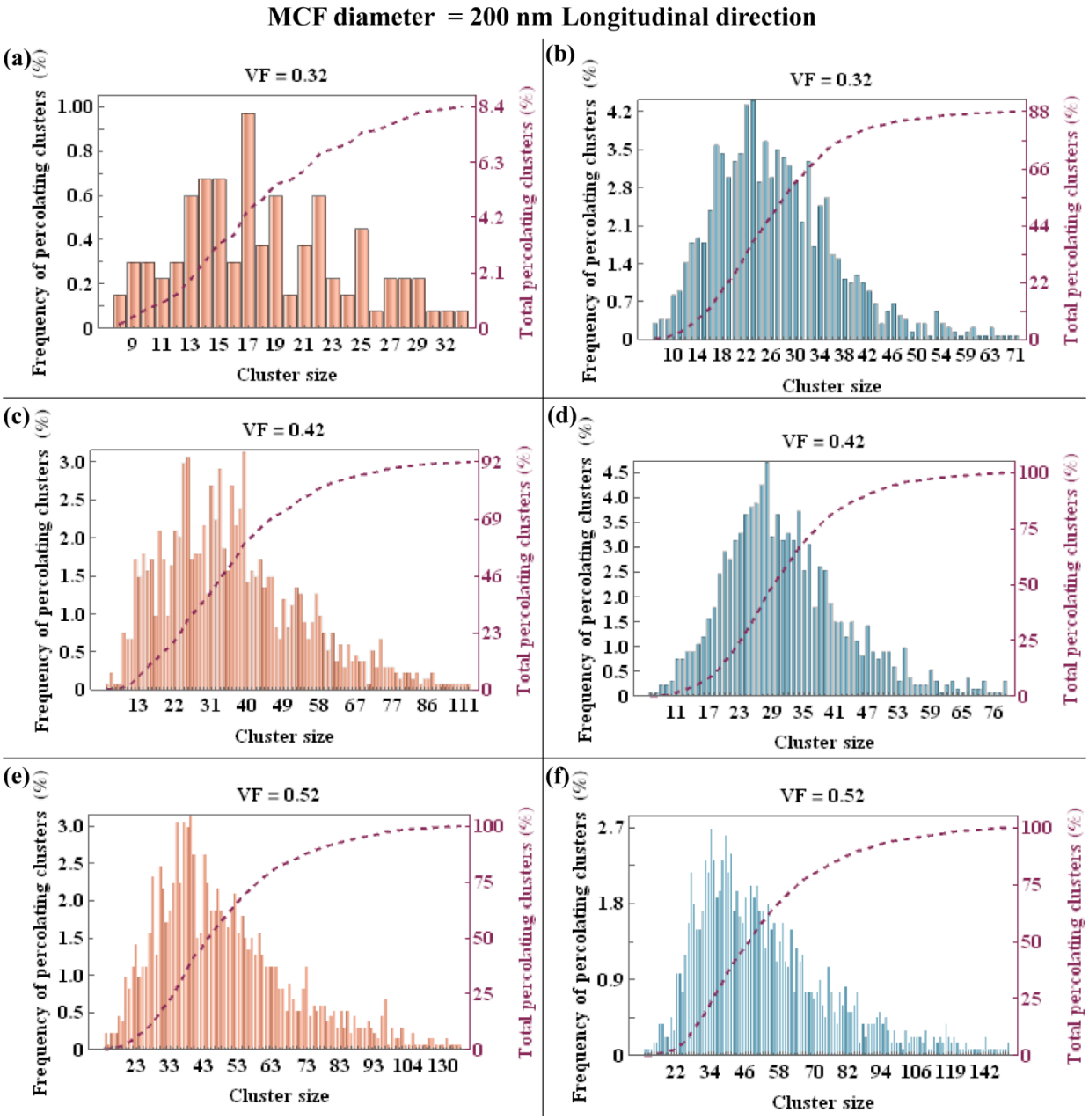

Figure 4.17: Frequency of percolating clusters (%) in function of cluster size, i.e. number of apatite platelets, mineral volume fraction of 32 percent (a, b), 42 percent (c, d), and 52 percent (e,f) in the longitudinal axis of the mineralized collagen fibril with diameter of 200 nm. The dark red curve represents the cumulative frequency (%) of percolating clusters. Clusters achieved assuming long-range interaction between minerals (blue) and interpenetrating crystals (light red) are reported.

In fact, for low mineral content, namely from 7 percent to 32 percent, the maximum frequency has a marked increasing trend reaching a maximum between 32 percent and 42 percent while for apatite VF greater than 42 percent a slightly decrement trend is noticed. This evolution finds a justification on the fact that for increasing mineral volume fraction, higher clusters are formed in detriment to smaller connected groups of platelets. Thus the distribution of cluster size is characterized by a smoother trend.

In addition, it was also observed that generally, percolating clusters in the equatorial plane are developed more frequently with respect to spanning clusters in the longitudinal direction. In the longitudinal direction, percolating clusters that span the MCF from an extremity of the simulation volume to the opposite one are less frequent. In Appendix, histograms corresponding to mineral VF of 42 percent, 47 percent and 52 percent are shown (Figure B.11 – B.13). In Figure 4.16-4.17, the plots concern percolating clusters with length greater than 300 nm and 450 nm for the MCF with 50 nm and 200 nm diameter, respectively. This approach is due to the intent to analyse length of MCF that have been recently identified by high resolution tomography investigations (Reznikov et al., 2018). Along the longitudinal direction, the trend of cluster size distributions is similar to the one that characterizes percolating clusters in the equatorial plane. In fact, the cluster size increments with increasing mineral VF for both MCF with diameter of 50 nm and 200 nm, respectively.

The results suggest that the percolation theory is a consistent approach that might describe the features of bone nanostructure. Hypomineralization conditions are characterized by small size of apatite crystals and increased value of mineral interdistance. In these cases, a reduced number of percolating clusters, composed also by modest number of platelets have been identified. The findings are in agreement with the experimental investigation of Xu et al. (2020) that identified stacks of 2- 8 minerals in a region of the MCF of 300 nm length. Thus, for low mineral VF, the apatite minerals do not predominate the MCF structure and they do not form anomalous networks, as it can be observed from the cluster analysis. This outcome suggests that the mechanical performance, the transport properties of the MCF are governed by the collagen matrix, in agreement also with Liu et al. (2013) and Depalle et al. (2016).

For higher degrees of mineralization, the percolating clusters are formed by an increased number of apatite platelets, i.e. up to 60 percent and 27 percent of the total number of mineral crystals in the MCF with diameter equal to 50 nm and 200 nm respectively. The hypermineralized conditions are characterized by the frequent development of percolating clusters. For instance, for mineral VFs greater than 42 percent, spanning clusters have been identified in more than 90 percent of the analysed configurations in both MCF diameters in the Equatorial plane. The onset of percolating clusters leads

to significative variations in the MCF architecture. In this condition, the features of the MCF are guided by the brittle mineral phase (Liu et al., 2013). Moreover, the hypermineralized condition may be characteristic of the aging process, during which the existing bone minerals are reorganized and form larger aggregates (Milovanovic et al., 2011).

The results highlight the power of the percolation theory as a qualitative and quantitative phenomenon descriptor. The numerical simulations developed in this Chapter lay the foundation to the development of a computational model that may provide insights into the phenomena observed experimentally and may highlight additional factors that contribute to the mechanical behaviour of the MCF. The model provides quantitative information concerning the mineralization degree associated with the development of connected network of platelets.

The computational model of complex systems, as the MCF, involved some limitations that should be discussed. The mineral platelets are represented as ideal geometric parallelepipeds, while tomographic investigations mentioned a plate-like irregular shape for the crystals. In addition, the finite size effects of the MCF have been overcame by the assumption of periodic boundary conditions. It became an interesting open aspect how the extension of the model to account for upper hierarchical levels, i.e. lamella level, may vary the outcomes.

The results show that the proposed method based on continuum percolation of hard-core soft-shell platelets can guide the assessment of the structure property relation of the MCF. The methodology described here may be extended to the evaluation of the effect of mineral volume fraction on the transport, structural and mechanic properties of bone nanostructure.

CHAPTER 5

Conclusions and perspectives

The overarching scope of this Thesis is to gain fundamental insight into bone nanostructure by means of computational models. For this purpose, algorithms based on Monte Carlo method and continuum percolation theory have been developed. The outcomes are, then, compared with available data in Literature. In this Chapter, the most salient results of this Thesis are discussed. Finally, an outlook towards future developments is provided.

5.1 Conclusions

Bone is a hierarchical material and the interplay of the main constituents affects its structural characteristics. Bone nanostructure has a fundamental role in determining the mechanical behaviour of the tissue, its mass transport properties or the evolution of bone pathologies. To date, the complexity and limitations of the actual imaging methods restrict the in-depth understanding of the structure (Liebi et al., 2015). Experimental investigation of the architecture of the nanoscale structure is still a challenging task and the organization and relationship between nanoscale components have not been elucidated. To overcome this limitation, computational models have been developed. Models proposed in Literature are mainly implemented adapting the framework of composite materials characterization and involving finite element method or molecular dynamics simulation. These models are mostly focused on the mechanical characterization of the mineralized collagen fibril, as described with major detail in Chapter 2. In this work, investigations concerning the features of bone nanostructure have been performed considering a continuum mechanics approach. The representation of the underlying atomic structure is beyond the scope of this study. 3D geometrical models of bone nanostructure, with increasing degree of complexity, have been proposed in this Thesis. The numerical investigations are developed applying the Monte Carlo probabilistic method.

The 3D geometrical models of bone nanostructure proposed in this study represent an extension of previous 2D models already available in Literature (Hodge and Petruska, 1969; Jäger and Fratzl, 2000). Scarce information concerning the 3D spatial arrangement of mineral platelets and distance between crystals in the MCF equatorial plane are available from experimental investigations. In Chapter 3 an idealized 3D model of a recurring unit cell within the MCF has been developed adapting the 2D models of Hodge and Petruska, (1969) and Jäger and Fratzl, (2000) by considering the indications about the spatial arrangement of the mineral crystals in the equatorial plane proposed in the study of Weiner et al. (1998). To achieve a realistic model of the unit cell, variable values extracted randomly from Gaussian Probability distribution functions for all the geometrical parameters involved and for the inclinations of mineral platelets have been considered.

Little is known about the water behaviour and interactions at the nanostructure level of bone tissue. Thus, numerical simulations based on Monte Carlo technique were successively implemented to determine the influence of the unit cell architecture on the water diffusion coefficient. The computational model investigates different mineral contents, i.e. low (7 percent), lower intermediate (32 percent), upper intermediate (42 percent) and high (52 percent) volume fraction. As extensively

discussed in Chapter 3, the agreement between the numerical values of the diffusion coefficient determined by the 3D model and literature data (Marinozzi et al., 2014b), confirms the suitability of the geometric dimensions assumed for the apatite platelets and collagen molecules and validates the arrangement of the mineral in the equatorial plane of the MCF.

The methodology presented in Chapter 3 allowed to provide quantitative information regarding the apatite crystals inclination. It is worth pointing out that the predicted apatite orientation obtained from the computational 3D model finds agreement with recent experimental investigations that utilized high resolution tomographic techniques (Xu et al., 2020).

Furthermore, the analysis concerning the influence of structural factors, i.e. tortuosity and constrictivity, on the diffusion coefficient leads to an extension of the bone nanostructure knowledge. The outcomes highlight that the tortuosity factor dominates the diffusivity rather than constrictivity. In fact, the variation of the passageway between tropocollagen molecules at different inclinations conditions and the consequent effect on the diffusivity is modest. Thus, from a perspective of mass transport phenomena, the spatial arrangement of mineral crystals has a crucial influence on the diffusion coefficient.

The findings of the 3D organization of the apatite crystals are then applied to analyse the effects of mineral VF variation on the nanostructure geometry (Chapter 4). This model overcomes the simplified unit cell structure investigated in Chapter 3 and extends the geometry to the entire MCF of 1000 nm length (Buehler, 2006). The degree of mineralization of the MCF and the arrangement of the crystals influence the behaviour of bone tissue. Several authors suggested that a fusion between mineral crystals may occur (Currey, 1969; Landis et al., 1993). However, to this date a relation between the mineral VF and the properties of the nanostructure has not been formulated. The study reported in Chapter 4 attempts to lay the foundations of a computational model that analyses the aforementioned open question.

The methodology of continuum percolation is applied and adapted to the cylindrical geometry of the MCF. The percolation theory is a versatile and diffuse methodology in the field of composite materials. Moreover, biological applications of this theory have been found in the study of the signals transmission within cells. However, in the field of bone biomechanics, this is the first attempt to apply the continuum percolation theory to a 3D model of bone nanostructure.

The analysis revealed that for high mineralization degrees, i.e. superior to 32 percent, the number and extension of spanning clusters within the MCF have a marked increase. The study provides evidence that apatite VF represents a critical factor of the MCF behaviour and it may be

related to anomalous configurations of the structure. The outcomes are also in agreement with molecular dynamics studies that identified an optimal VF of the MCF around 30 percent (Depalle et al., 2016). In addition, the formation of groups of connected apatite platelets is consistent with the recent experimental investigations of Xu et al. (2020) and Reznikov et al. (2018). The enhancement of high resolution tomographic, spectroscopic and microscopic techniques expanded the understanding of bone composition and structure. However, limitations to a thorough experimental characterization of the MCF still exist. For instance, the study of Xu et al. (2020) considers a region of the MCF, which extent is constrained by the limits of the TEM technique. The computational model described in this study overcomes this issue and analyses how different mineral VFs are organized within an entire 1000 nm long MCF.

Previous studies in literature made the hypothesis of a possible coalescence of the apatite mineral (Landis et al., 1993; Currey, 1969), that conceivably may alter the properties of the MCF. The conditions and the mechanism that foster the formation of percolating clusters have not been investigated in the current Literature. This research may pave the way to an in-depth quantitative description of the MCF in both physiological and pathological conditions, that can be associated with an increased number of percolating clusters.

In terms of methodological aspects, the 3D continuum percolation theory is applied to bone nanostructure adapting the algorithms proposed by Torquato (2002), Newman and Ziff (2001) and Schilling et al. (2015). The most relevant variations are linked to the cylindrical geometry of the MCF and concern the determination of the radial distribution function for the equatorial plane and in the longitudinal direction of the structure, as illustrated in Chapter 4, Section 4.2.3.1. Moreover, also the algorithm concerning the cluster identification had to be modified in order to take into account the non-spherical geometry of the apatite crystals and their polydispersivity. It is worth pointing out that the available models in Literature analysing the 3D continuum percolation are based on objects characterized by 1 or 2 geometric parameters, e.g. spheres, ellipsoids, cuboids or spherocylinders. For instance, the geometrical contact between two spheres occurs when the distance between their centres is inferior or equal to the sphere radius in any 3D direction. In the present study the apatite platelets were modelized as ideal parallelepipeds. Therefore, to determine contact and interpenetration between platelets an optimization algorithm based on identifying the nearest point between two parallelepipeds had to be implemented.

Bone properties are closely related to the hierarchical structure. The study of the structural organization at the nanoscale, where the MCF represents the basic building block of bone tissue,

outlines the functional conditions for the development of biomimetic strategies for tissue engineering and for the creation of biomaterials with similar properties to those of bone tissue.

Knowledge about the organization and orientation of apatite crystals that emerged from the presented research may facilitate the design of synthetic systems. Tissue engineering aims creating functional constructs mimicking native tissues, e.g. liver, skin, bone, for repair and replacement of damaged biological regions (Agarwal et al., 2020). Among the approaches used in the field of tissue engineering, the 3D bioprinting represents an emerging technique that provides the possibility of combining different materials, various specific cell types and biologically active factors in a spatially defined pattern (Kilian et al., 2020). This strategy enables accurate control of scaffold morphology and cell distribution and allows the development of more specific complex tissue models. However, despite the advantages and convenience offered by the 3D bioprinting, the state-of-art technology involves several key challenges, e.g. vascularization of the tissue, improvement of nutrient exchange process, biocompatibility, shape-fidelity and preservation of functionality of printed tissue (Genova et al., 2020; Agarwal et al., 2020).

To date, 3D bioprinting methods for the generation of mineralized collagen scaffolds were already designed (Chimene et al., 2020; Kilian et al., 2020), but further improvements are required in order to provide an environment similar to that of bone natural matrix. Thus, from a tissue engineering point of view, the optimization of bio-scaffold should take into account and mimic biochemical and physical stimuli and the hierarchical structure of bone. The current strategy to simulate hierarchical organization is to build the nano – and micro -scale bone features (Gong et al., 2015; Chimene et al., 2020). Moreover, bio-scaffolds should have similar properties to bone tissue in terms of mass transport properties and mechanical characteristics in order to ensure the transport of nutrients, waste products, signalling molecules and to maintain the strength and toughness of the structure at physiological values. The outcomes of this study concerning the influence of the mineral crystals on the diffusion coefficient and the information about critical behaviour of bone tissue dependent on the mineral VF, may help to control the mechanical and biological performance of bio-scaffolds. Therefore, the condition for the design, development and optimization of synthetic mineralized collagen materials is a better comprehension of the structure – property relationship in physiological conditions. Thorough knowledge of bone nanostructure is essential to improve longevity of bioscaffolds and to decrease the risk of failure.

In summary, the arrangement and organization of apatite mineral at the MCF level have been investigated throughout this Thesis. Computational methodologies to get deeper insights into bone nanostructure have been proposed and implemented. Monte Carlo technique has been applied with

different approaches: from Gibbs sampler algorithm (Chapter 3) to Metropolis algorithm (Chapter 4). Overall, the added value of applying probabilistic methods as complementary investigations to experimental data has been highlighted in this work. The agreement with experimental investigations confirms that the assumptions made during the development of the 3D geometrical models of bone nanostructure are appropriate.

The analyses of the mass transport property and the investigation of the development of connected network of apatite crystals have focused on several conditions of hypo – and hyper – mineralization that could reflect pathological conditions. According to experimental data, aging, diseases of low mineral content (osteomalacia) or high mineralization (osteoporosis) produce abnormalities in bone structure. For instance, osteoporosis is thought to become an essential health issue (Burr, 2002). It is due to aging, decreased endocrine functions, but may be also caused by other types of health issues, e.g. immobilization or weightless conditions as well as special working conditions, e.g. microgravity. Therefore, knowledge about the behaviour of bone structure in normal and pathological conditions is fundamental for the definition of the therapeutic strategy, targeted to the different groups of persons, e.g. elderly persons or space flights participants.

5.2 Future perspectives

Next to the aforementioned conclusions there are many questions that have remained unanswered and merit attention in future studies. Several future research directions are conceivable, aiming at confirming the insights presented in this work and extending the underlying model.

The 3D models of bone nanostructure represent the foundation of predictive studies that analyse the structural and mechanical behaviour at several length scales, e.g. from the MCF at the nanoscale, to the lamella level and to the trabecula.

In Chapter 3 the algorithm based on the Monte Carlo method allows to investigate the dependence of the diffusion coefficient on the orientation of the apatite crystals and on the structural factors, i.e. constrictivity and tortuosity. A future development of this study should estimate the tendency of diffusion under some specific tortuosity and constrictivity values with mineral VF variation from lower to higher values. Thus, several values of the mineral volume fraction within the range indicated in literature should be considered, while the tortuosity factor should be characterized by an extremely narrow interval of values. It is worth pointing out that the values adopted for the

tortuosity should take into account the direction of the flow direction, since the results achieved in this study highlight that the tortuosity factor exhibits a significant dependence on the arrangement of the mineral platelets. Conversely, the constrictivity could be characterized by a fixed value for each volume fraction considered and for specific flow direction, since the outcomes of the numerical simulation performed in the present work highlight that this structural factor results less influenced by the arrangement of the apatite crystals.

In Chapter 4 the percolation theory is applied to a 3D model of MCF in order to investigate the onset of connected networks of mineral crystals. The mineral configuration is developed using the Metropolis algorithm in which platelets start in a regular configuration and then are subjected to random displacements and inclinations. The perturbations are allowed if they do not cause an interpenetration superior to 10 percent of apatite platelet volume. Since information in literature is missing related to the value of the allowed interpenetration, this was selected in order to reflect an initial stage of crystal fusion. An extension of this study may concern a parametrization with increasing values of the interpenetration percentage and the subsequent analysis of the development of connected clusters of apatite. Increased values of interpenetration may be attributed to advanced stage of mineral fusion, that could occur in pathological conditions characterized by hypermineralization, e.g. osteoporosis, osteopetrosis. This hypothesis should be investigated in the future.

In Chapter 4 and in Appendix B it was highlighted that clusters that span the entire length of the MCF are rarely formed. It will be interesting to investigate whether an increment of the number of iterations considered in the Monte Carlo algorithm may affect the development of percolating clusters in the longitudinal direction. Probably, a major number of moves and rotations per platelets would lead to a growth of the number of spanning clusters in the longitudinal direction. However, this hypothesis needs further studies.

It is worth to pointing out that there still exists a large gap of information when switching between the structure bottom levels to the next structural level. Therefore, an interesting study would aim to identify connected networks of apatite crystals at higher length scales, i.e. lamella and subsequently trabecula, for different degrees of mineralization, and therefore in normal and pathological conditions.

Appendix A

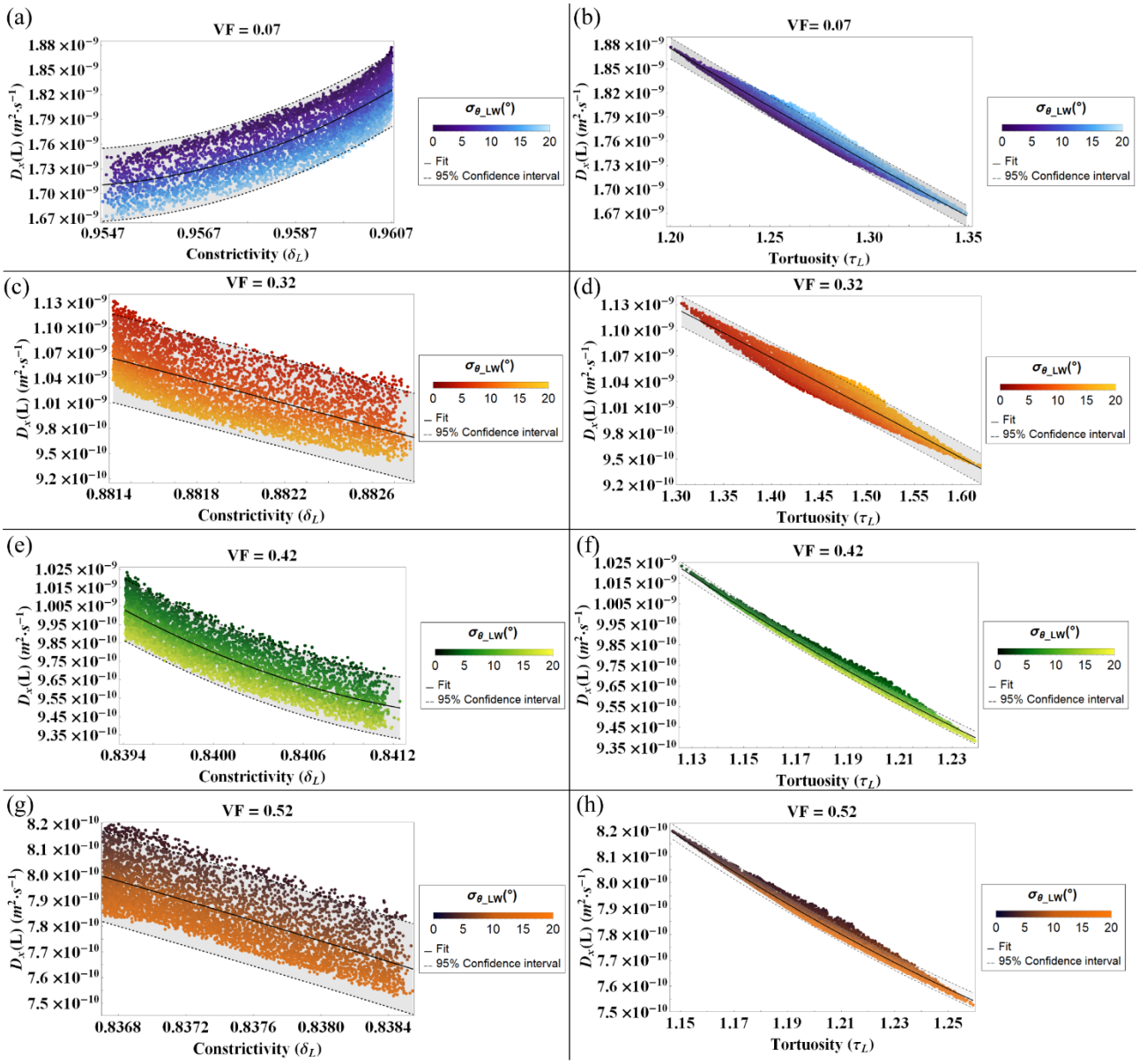

Figure A.1: Diffusion coefficient (D_L) for a flow parallel to the longitudinal axis (L) represented in function of the constrictivity (a, c, e, g) and tortuosity factors (b, d, f, h) for different mineralization degrees, i.e. V_{f_A} = 0.07 (a, b), V_{f_A} = 0.32 (c, d), V_{f_A} = 0.42 (e, f) and V_{f_A} = 0.52 (g, h). The colour gradient indicates the standard deviation (σ_{LW}) of the Gaussian PDF that characterizes the inclination of the apatite minerals in the LW plane. The grey bands show the Confidence Interval at 95 percent.

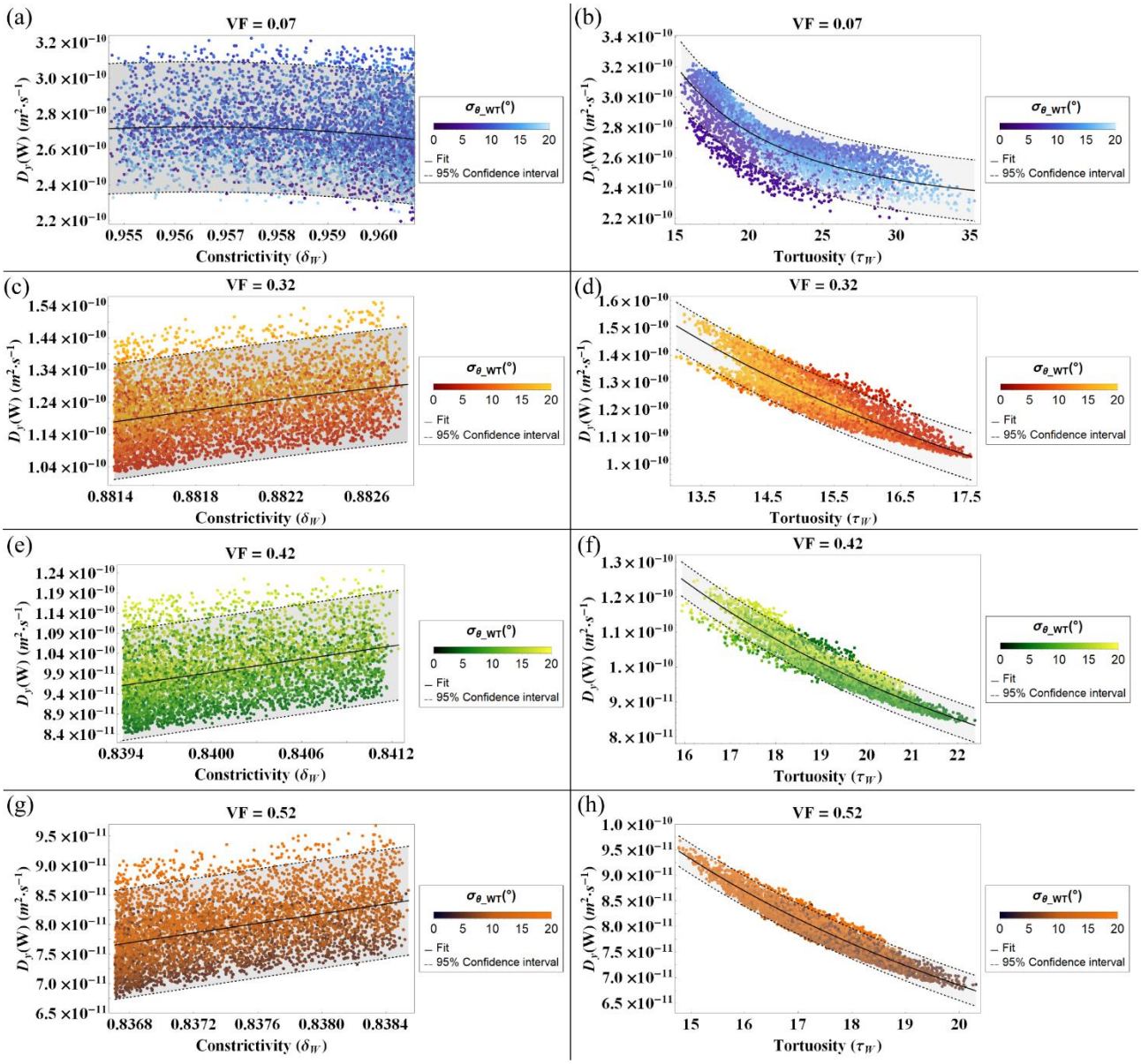

Figure A.2: Diffusion coefficient (D_W) for a flow parallel to the width direction (W) represented in function of the constrictivity (a, c, e, g) and tortuosity factors (b, d, f, h) for different mineralization degrees, i.e. V_{f_A} = 0.07 (a, b), V_{f_A} = 0.32 (c, d), V_{f_A} = 0.42 (e, f) and V_{f_A} = 0.52 (g, h). The colour gradient indicates the standard deviation (σ_{WT}) of the Gaussian PDF that characterizes the inclination of the apatite minerals in the WT plane. The grey bands show the Confidence Interval at 95 percent.

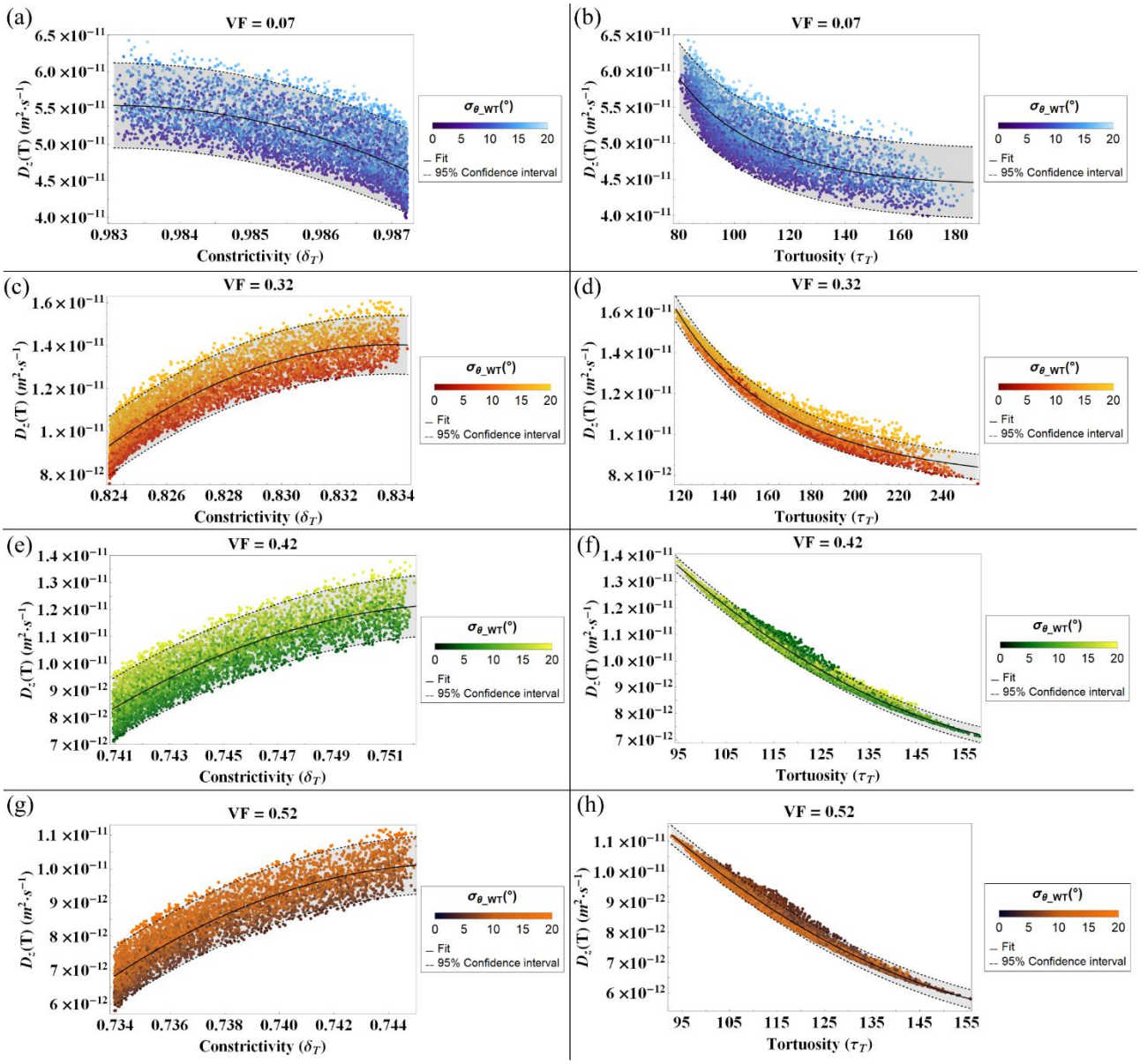

Figure A.3: Diffusion coefficient (D_T) for a flow parallel to the thickness direction (T) represented in function of the constrictivity (a, c, e, g) and tortuosity factors (b, d, f, h) for different mineralization degrees, i.e. V_{f_A} = 0.07 (a, b), V_{f_A} = 0.32 (c, d), V_{f_A} = 0.42 (e, f) and V_{f_A} = 0.52 (g, h). The colour gradient indicates the standard deviation (σ_{WT}) of the Gaussian PDF that characterizes the inclination of the apatite minerals in the WT plane. The grey bands show the Confidence Interval at 95 percent.

Appendix B

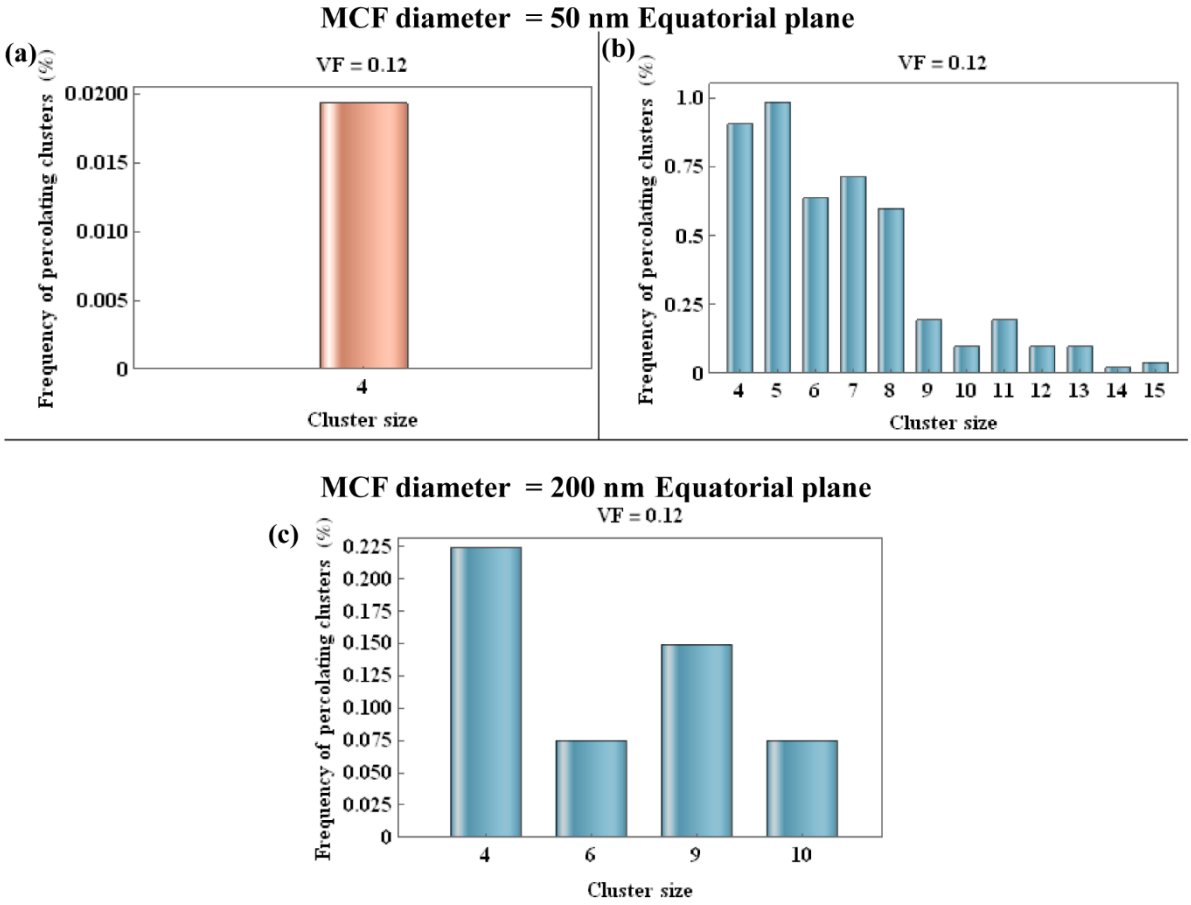

Figure B.1: Frequency of percolating clusters (%) in function of cluster size, i.e. number of apatite platelets, for a mineral volume fraction of 12 percent in the equatorial plane of the mineralized collagen fibril with diameter of 50 nm (a, b) and 200 nm (c). Clusters achieved assuming long-range interaction between minerals (blue) and interpenetrating crystals (light red) are reported. For the MCF of 200 nm diameter, percolating clusters composed of interpenetrating platelets were not found.

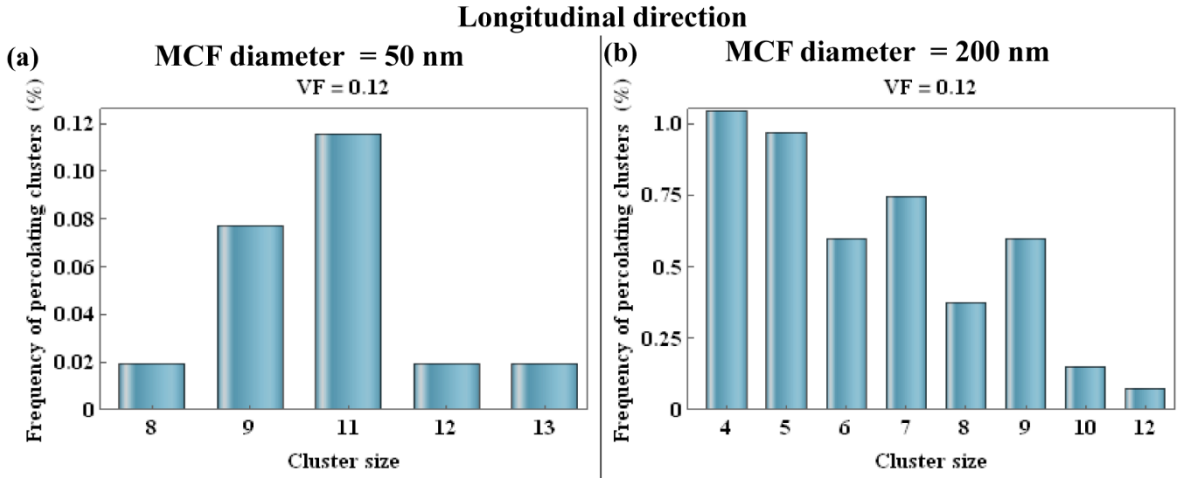

Figure B.2: Frequency of percolating clusters (%) in function of cluster size, i.e. number of apatite platelets, for a mineral volume fraction of 12 percent in the longitudinal direction of the mineralized collagen fibril with diameter of 50 nm (a) and 200 nm (b). Spanning clusters were identified only assuming long-range interaction between minerals (blue).

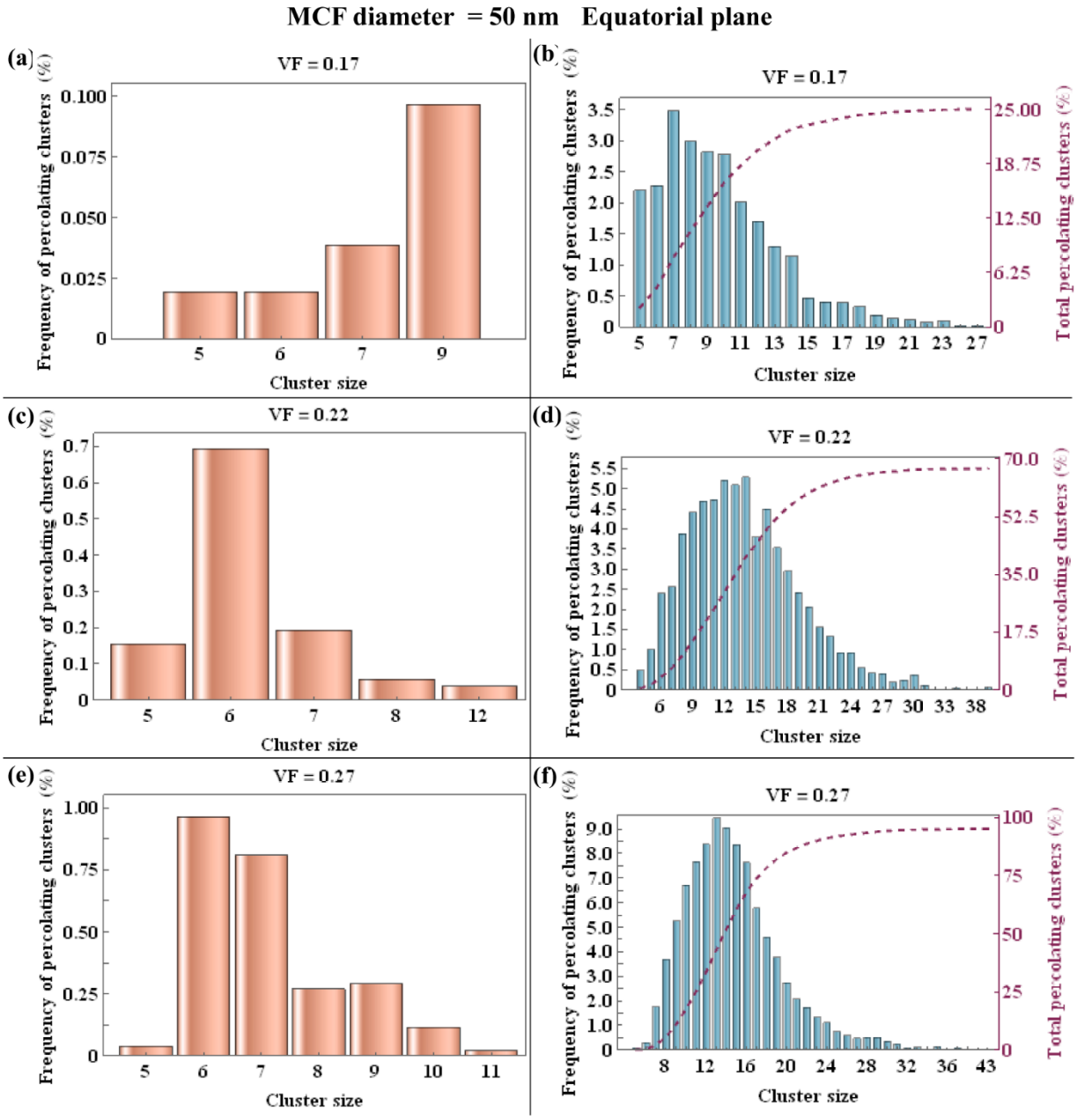

Figure B.3: Frequency of percolating clusters (%) in function of cluster size, i.e. number of apatite platelets, for a mineral volume fraction of 17 percent (a, b), 22 percent (c, d), and 27 percent (e,f) in the equatorial plane of the mineralized collagen fibril with diameter of 50 nm. The dark red curve represents the cumulative frequency (%) of percolating clusters. Clusters achieved assuming long-range interaction between minerals (blue) and interpenetrating crystals (light red) are reported.

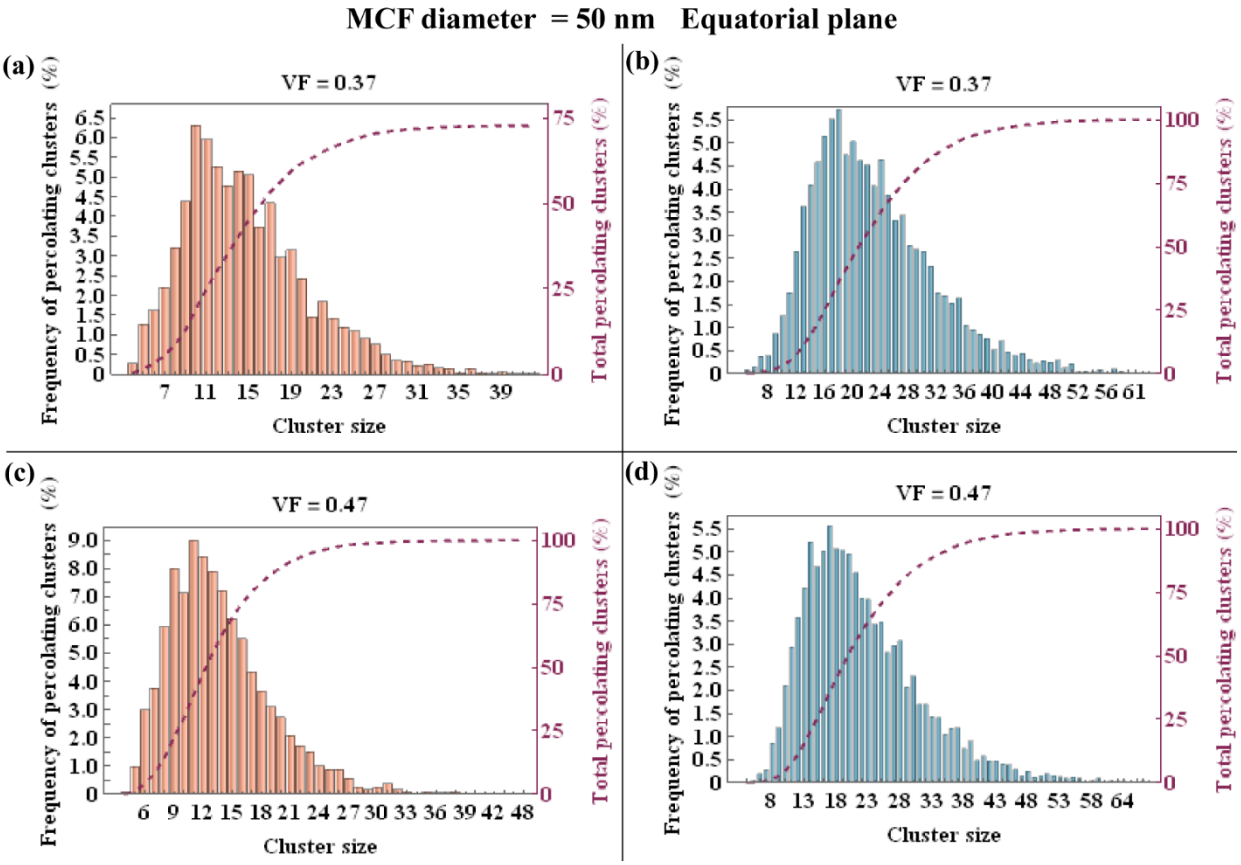

Figure B.4: Frequency of percolating clusters (%) in function of cluster size, i.e. number of apatite platelets, for a mineral volume fraction of 37 percent (a, b), 47 percent (c, d) in the equatorial plane of the mineralized collagen fibril with diameter of 50 nm. The dark red curve represents the cumulative frequency (%) of percolating clusters. Clusters achieved assuming long-range interaction between minerals (blue) and interpenetrating crystals (light red) are reported.

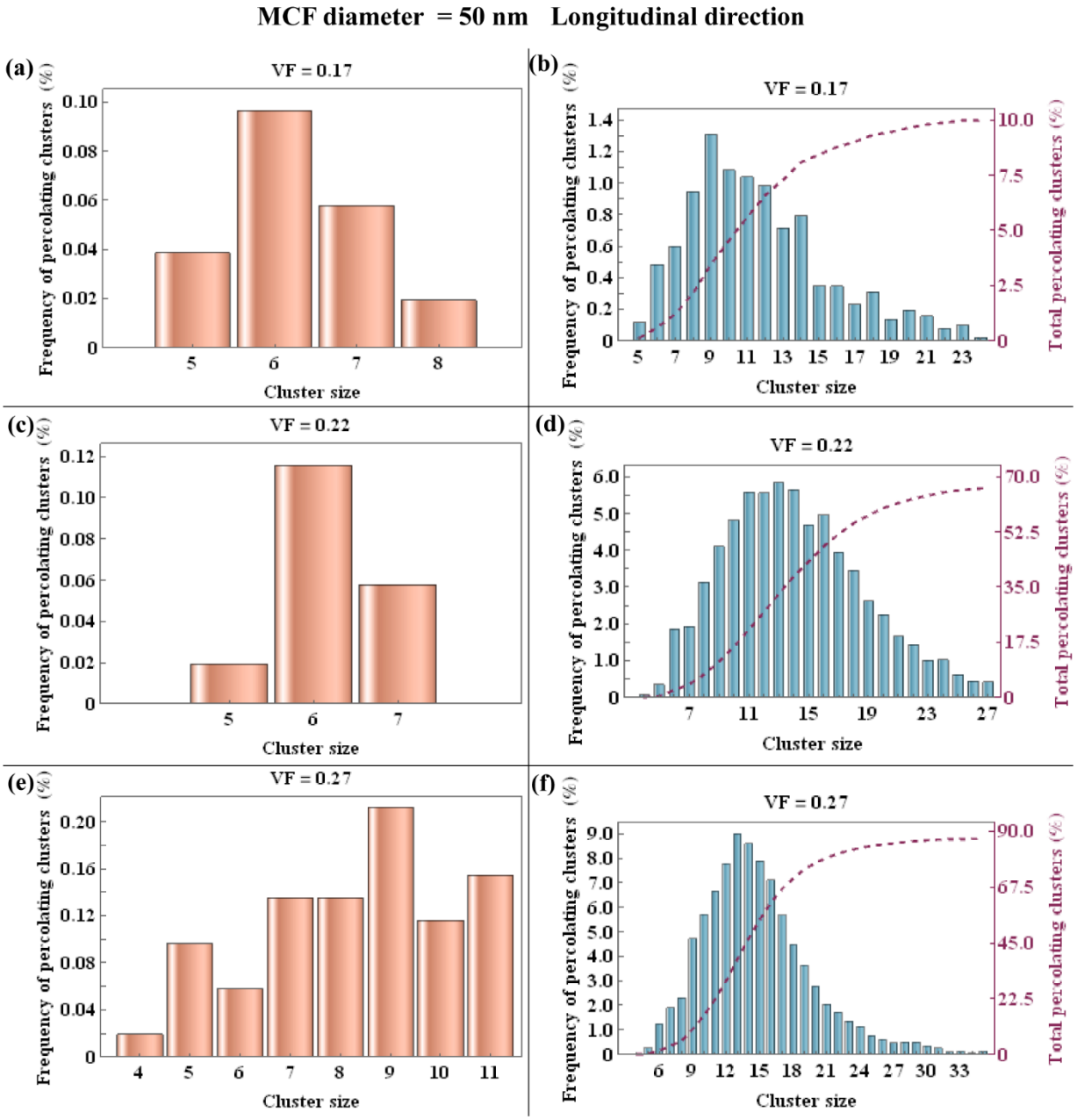

Figure B.5: Frequency of percolating clusters (%) in function of cluster size, i.e. number of apatite platelets, for a mineral volume fraction of 17 percent (a, b), 22 percent (c, d), and 27 percent (e,f) in the longitudinal direction of the mineralized collagen fibril with diameter of 50 nm. The dark red curve represents the cumulative frequency (%) of percolating clusters. Clusters achieved assuming long-range interaction between minerals (blue) and interpenetrating crystals (light red) are reported. The clusters have been identified considering a MCF length of 300 nm.

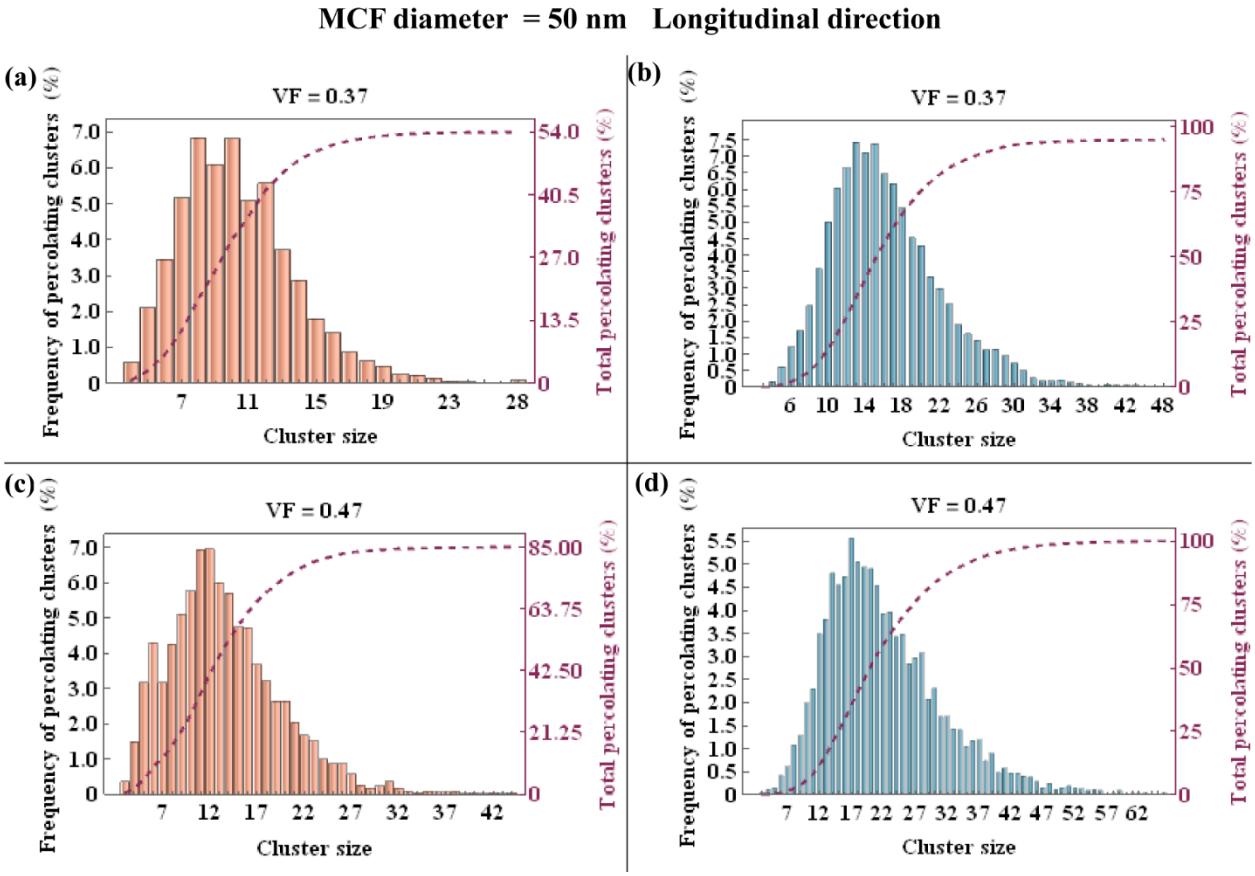

Figure B.6: Frequency of percolating clusters (%) in function of cluster size, i.e. number of apatite platelets, for a mineral volume fraction of 37 percent (a, b), 47 percent (c, d) in the longitudinal direction of the mineralized collagen fibril with diameter of 50 nm. The dark red curve represents the cumulative frequency (%) of percolating clusters. Clusters achieved assuming long-range interaction between minerals (blue) and interpenetrating crystals (light red) are reported. The clusters have been identified considering a MCF length of 300 nm.

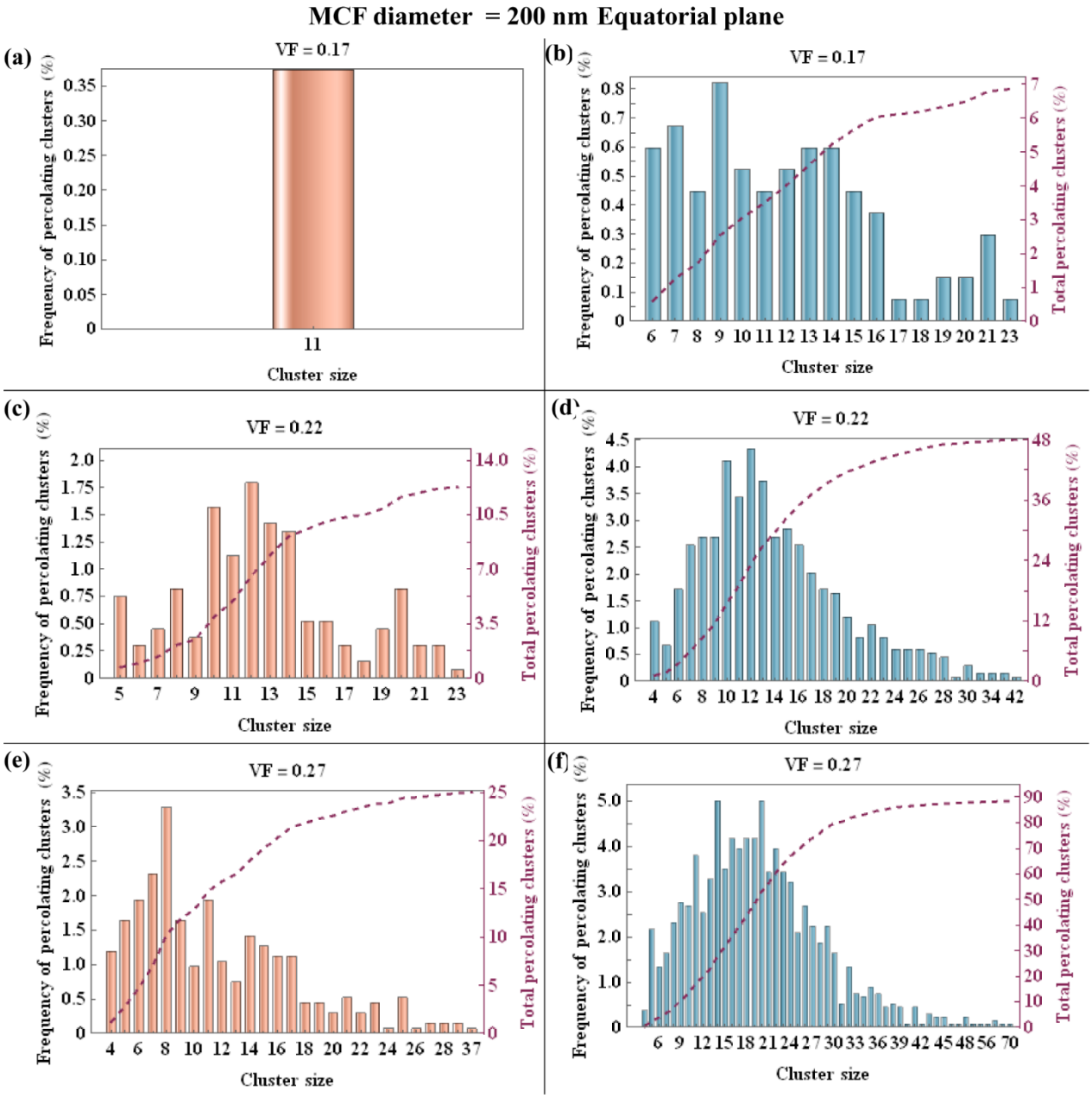

Figure B.7: Frequency of percolating clusters (%) in function of cluster size, i.e. number of apatite platelets, for a mineral volume fraction of 17 percent (a, b), 22 percent (c, d), and 27 percent (e,f) in the equatorial plane of the mineralized collagen fibril with diameter of 200 nm. The dark red curve represents the cumulative frequency (%) of percolating clusters. Clusters achieved assuming long-range interaction between minerals (blue) and interpenetrating crystals (light red) are reported.

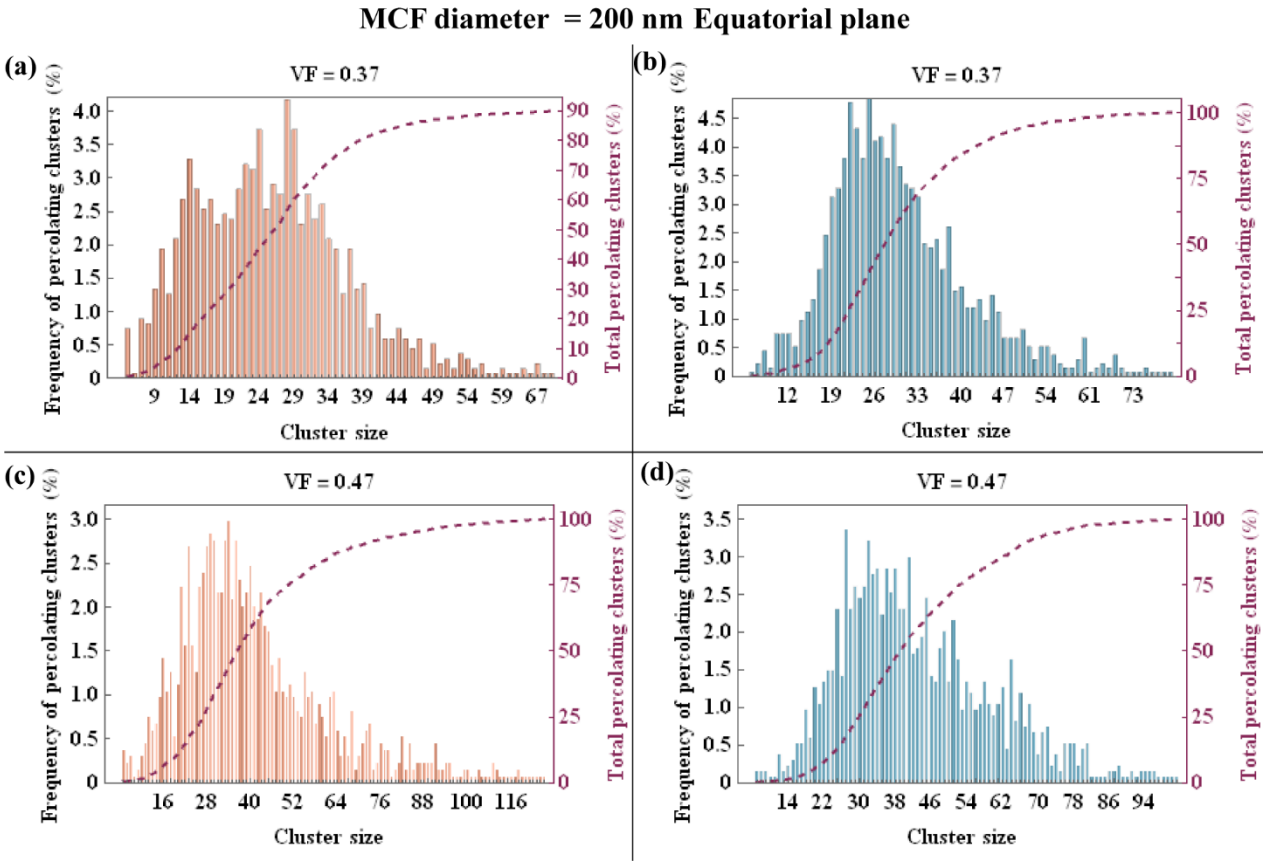

Figure B.8: Frequency of percolating clusters (%) in function of cluster size, i.e. number of apatite platelets, for a mineral volume fraction of 37 percent (a, b), 47 percent (c, d) in the equatorial plane of the mineralized collagen fibril with diameter of 200 nm. The dark red curve represents the cumulative frequency (%) of percolating clusters. Clusters achieved assuming long-range interaction between minerals (blue) and interpenetrating crystals (light red) are reported.

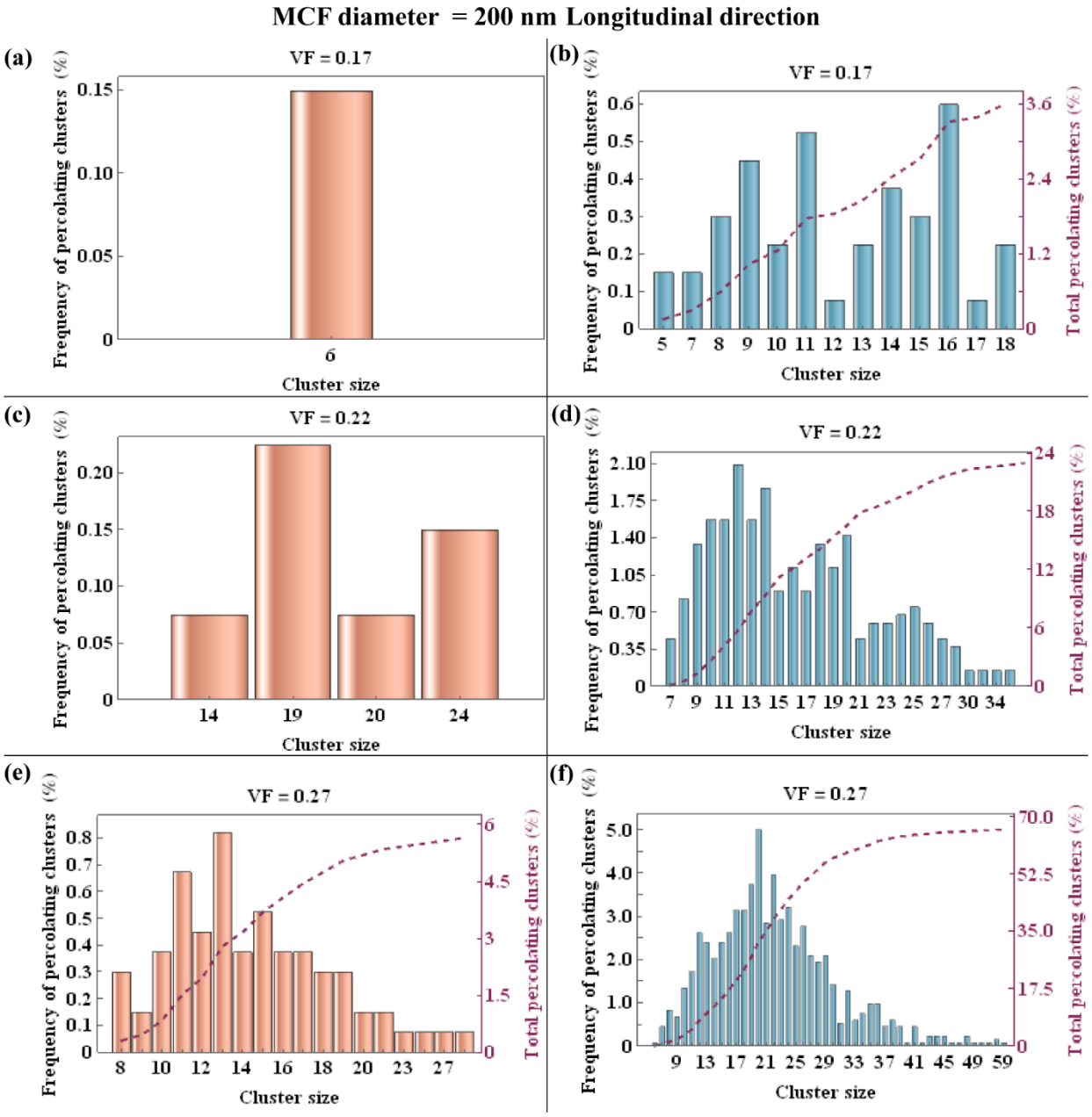

Figure B.9: Frequency of percolating clusters (%) in function of cluster size, i.e. number of apatite platelets, for a mineral volume fraction of 17 percent (a, b), 22 percent (c, d), and 27 percent (e,f) in the longitudinal direction of the mineralized collagen fibril with diameter of 200 nm. The dark red curve represents the cumulative frequency (%) of percolating clusters. The clusters have been identified considering a MCF length of 450 nm. Clusters achieved assuming long-range interaction between minerals (blue) and interpenetrating crystals (light red) are reported.

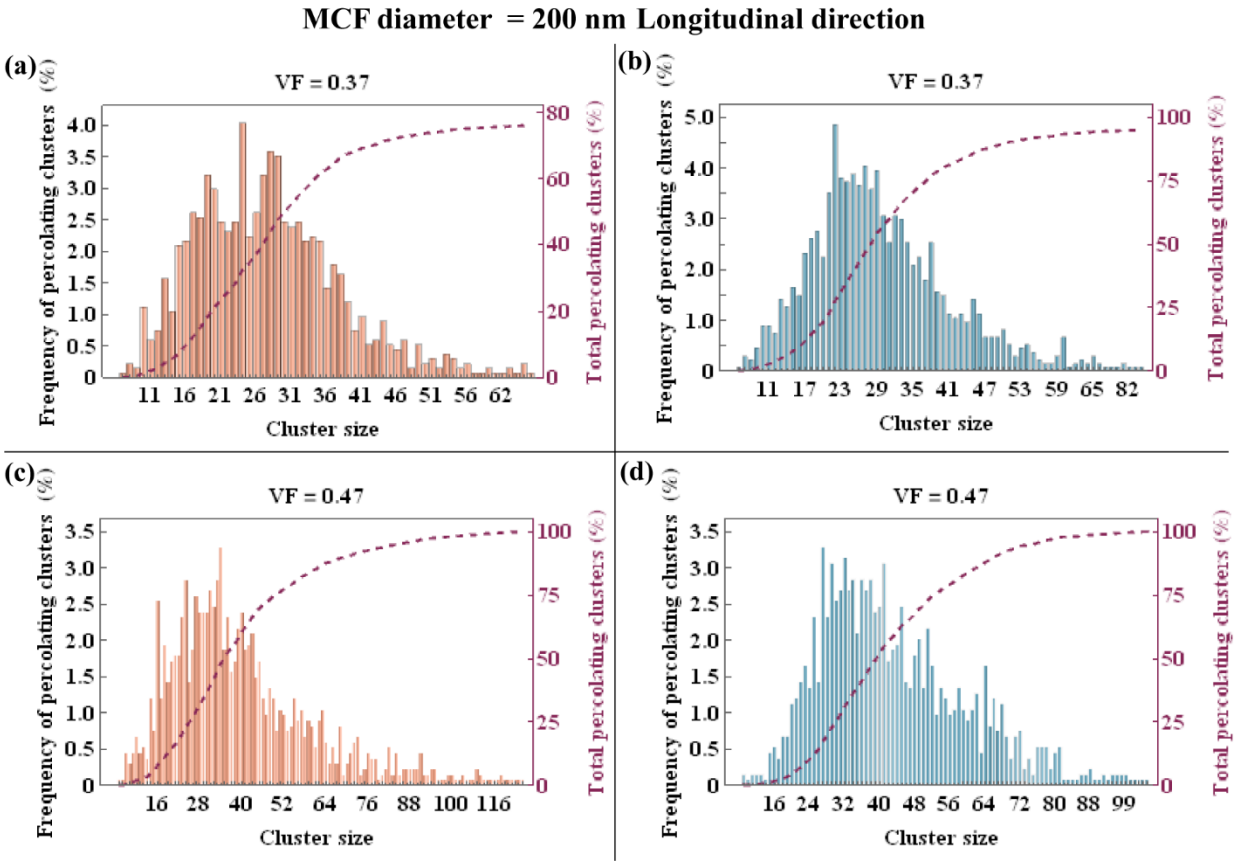

Figure B.10: Frequency of percolating clusters (%) in function of cluster size, i.e. number of apatite platelets, for a mineral volume fraction of 37 percent (a, b), 47 percent (c, d) in the longitudinal direction of the mineralized collagen fibril with diameter of 200 nm. The dark red curve represents the cumulative frequency (%) of percolating clusters. The clusters have been identified considering a MCF length of 450 nm. Clusters achieved assuming long-range interaction between minerals (blue) and interpenetrating crystals (light red) are reported.

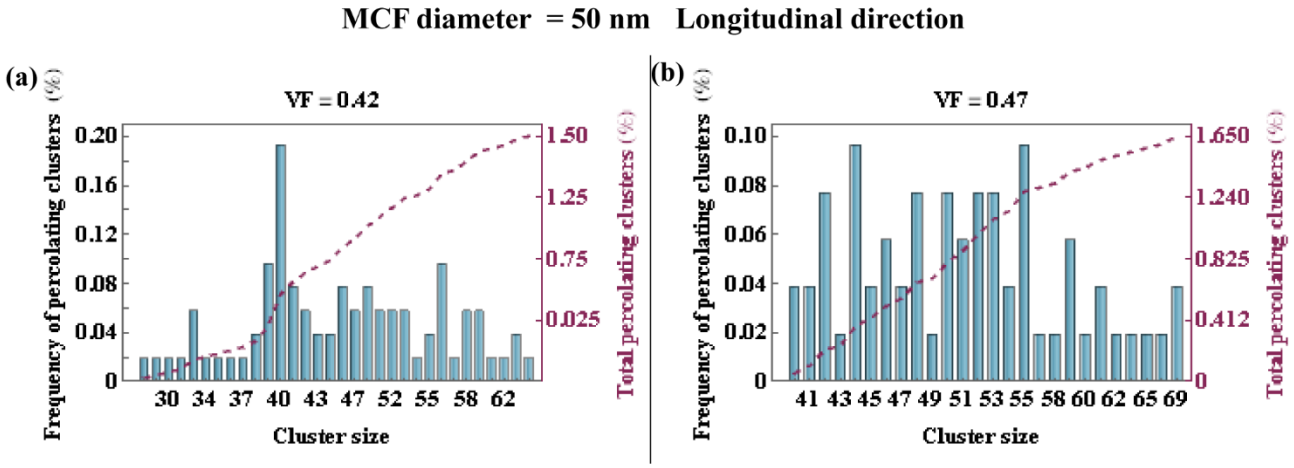

Figure B.11: Frequency of percolating clusters (%) in function of cluster size, i.e. number of apatite platelets, for a mineral volume fraction of 42 percent (a), 47 percent (b) in the longitudinal direction of the mineralized collagen fibril with diameter of 50 nm. The dark red curve represents the cumulative frequency (%) of percolating clusters. Clusters achieved assuming long-range interaction between minerals. Spanning clusters along the full length of the MCF are considered.

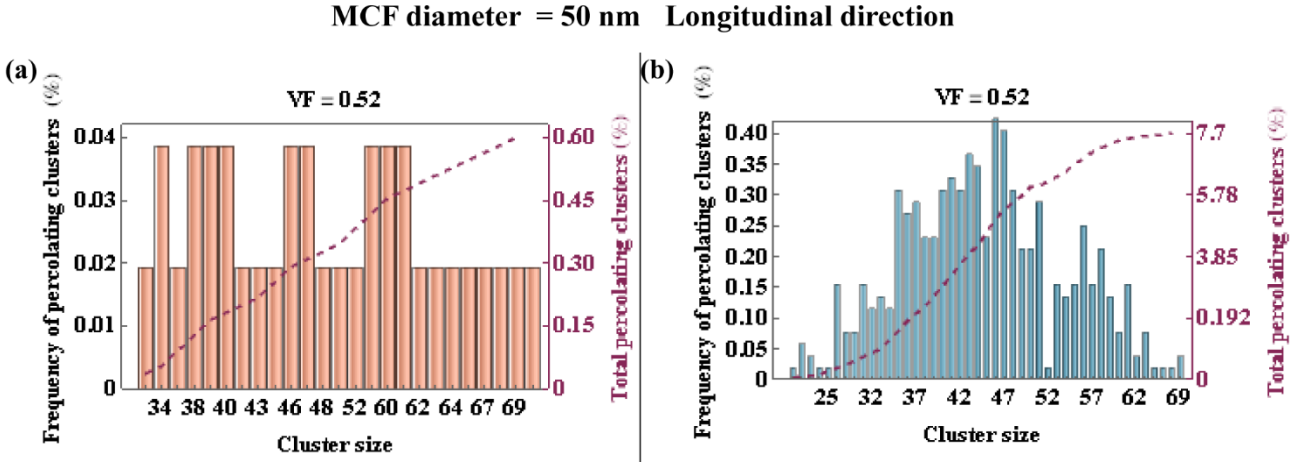

Figure B.12: Frequency of percolating clusters (%) in function of cluster size, i.e. number of apatite platelets, for a mineral volume fraction of 52 percent in the longitudinal direction of the mineralized collagen fibril with diameter of 50 nm. The dark red curve represents the cumulative frequency (%) of percolating clusters. Clusters achieved assuming long-range interaction between minerals (blue) and interpenetrating crystals (light red) are reported. Spanning clusters along the full length of the MCF are considered.

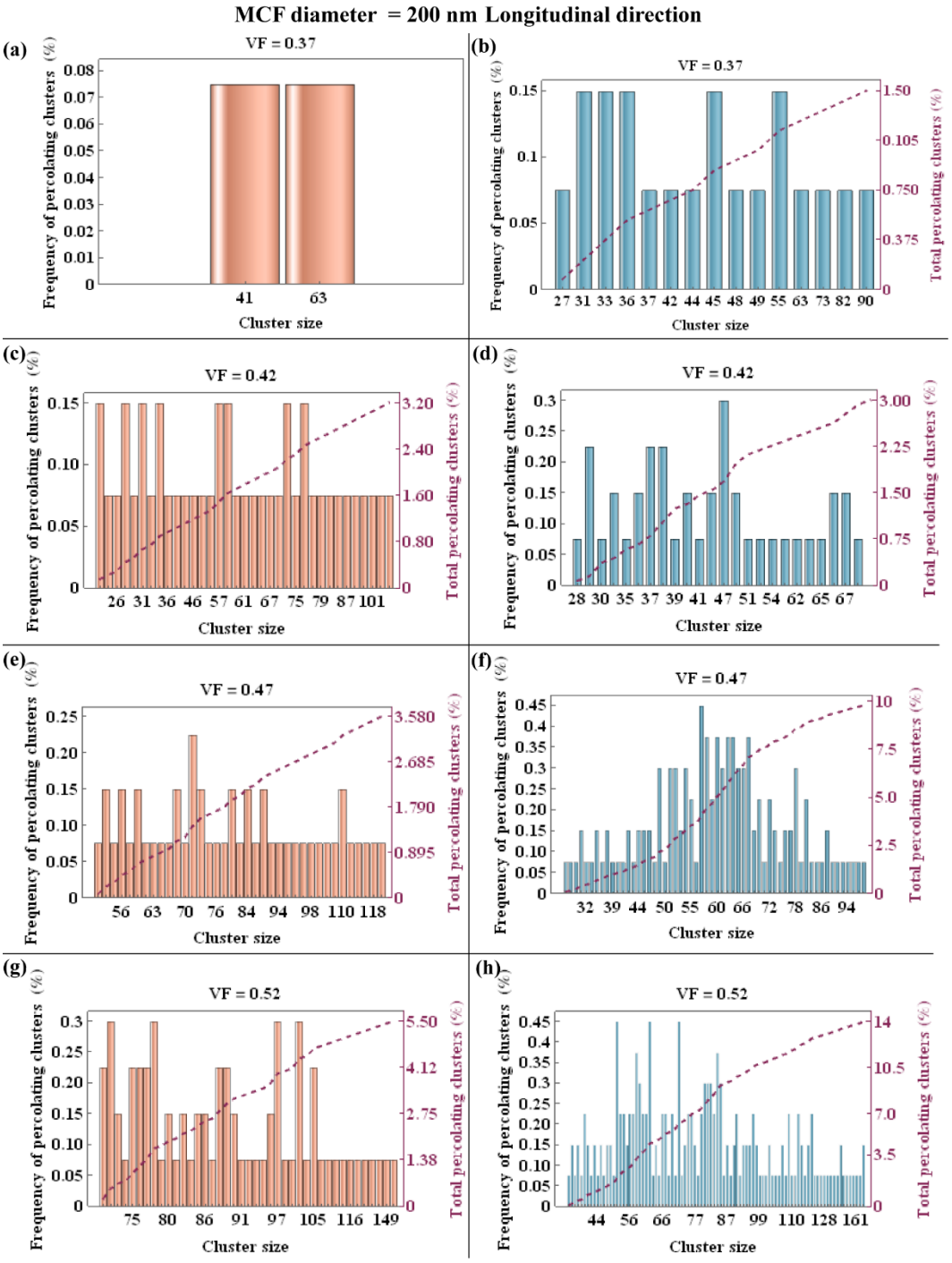

Figure B.13: Frequency of percolating clusters (%) in function of cluster size, i.e. number of apatite platelets, for a mineral volume fraction of 37 percent (a, b), 42 percent (c, d), 47 percent (e,f) and 52 percent (g,h) in the longitudinal direction of the mineralized collagen fibril with diameter of 200 nm. The dark red curve represents the cumulative frequency (%) of percolating clusters. Clusters achieved assuming long-range interaction between minerals (blue) and interpenetrating crystals (light red) are reported. Spanning clusters along the full length of the MCF are considered.

It is worth pointing out that the histograms related to spanning clusters along the entire length of the MCF (Figures B.11-B.13) show a different trend with respect to the correspondent plots achieved considering minor length of the MCF. This is justified by the extremely small frequencies obtained for this condition of percolation. Probably a major number of moves and rotations would allow to achieve significative numbers of percolating clusters, especially in hypermineralized conditions (Landis et al., 1993).

Appendix C: Publications and presentations

C.1 Peer-Reviewed Journals

- Fabiano Bini, **Andrada Pica**, Andrea Marinozzi, Franco Marinozzi. A 3D Model of the effect of tortuosity and constrictivity on the diffusion in mineralized collagen fibril. Scientific Reports vol. 9: 1, Article number 2658 (2019) – Impact Factor 3.998 (2019)
- Fabiano Bini, **Andrada Pica**, Andrea Marinozzi, Franco Marinozzi. 3D diffusion model within the collagen apatite porosity: An insight to the nanostructure of human trabecular bone. PLoS ONE 12(12): e0189041 (2017) – Impact Factor 1.164 (2017)

C.2 International Conference proceedings

- Fabiano Bini, **Andrada Pica**, Simone Novelli, Andrea Marinozzi, Franco Marinozzi. 2019. 3D-FEM Modeling of iso-concentration maps in single trabecula from human femur head. In: Tavares J., Natal Jorge R. (eds) VipIMAGE 2019 – Proceedings of the VII ECCOMAS thematic conference on computational vision and medical image processing, October 16-18, 2019, Porto, Portugal. Lectures notes in computational vision and biomechanics, vol. 34 Springer, Cham, pp. 509-518 (2019)

C.3 Published conference abstracts

- Fabiano Bini, **Andrada Pica**, Andrea Marinozzi, Franco Marinozzi. Random walk in 3D model of water diffusion in the human mineralized collagen fibril. Journal of Bone Mineral Research, Volume 35, IssueS1 - Supplement: 2020 Annual Meeting of the American Society for Bone and Mineral Research Virtual Event September 11–15, 2020, page S146, (2020) – Impact Factor 5.854 (2020)

REFERENCES

Abe, H., Hayashi, K., Sato, M. (eds). Data Book on Mechanical Properties of Living Cells, Tissues and Organs. Springer, Tokyo, Berlin (1996).

Abramowitz, M., Stegun, I. A. (Eds.). Elliptic Integrals in *Handbook of Mathematical Functions with Formulas, Graphs, and Mathematical Tables*, 9th printing, 587-607, New York: Dover (1972).

Agarwal, S., Saha, S., Balla, V.K., Pal, A., Barui, A., Bodhak, S. Current developments in 3D bioprinting for tissue and organ regeneration – a review. Front. Mech. Eng. 6:589171 (2020).

Aido, M., Kerschnitzki, M., Hoerth, R., Burghammer, M., Montero, C., Checa, S., Fratzl, P., Duda, G.N., Willie, B.M., Wagermaier, W. Relationship between nanoscale mineral properties and calcein labeling in mineralizing bone surfaces. Connect. Tissue Res. 55, 15–17 (2014).

Allen, M.P., Tildesley. Computer simulations of liquids. Clarendon Press, Oxford (1989).

Baalberg, I., In: Encyclopedia of Complexity and Systems Science - Continuum Percolation. Meyers R. (eds) Springer, Berlin, Heidelberg (2016).

Baker, D.R., Paul, G., Sreenivasan, S., Stanley, H.E. Continuum percolation threshold for interpenetrating squares and cubes. Phys Rev E Stat Nonlin Soft Matter Phys. 66 (4 Pt 2): 046136 (2002).

Barkaoui, A., Hambli, R., Tavares, J.M.R.S. Effect of material and structural factors on fracture behaviour of mineralised collagen microfibril using finite element simulation. Comput Methods Biomech Biomed Engin, 18:11, 1181-1190 (2015).

Barkaoui, A., Tlili, B., Vercher-Martínez, A., Hambli, R. A multiscale modelling of bone ultrastructure elastic proprieties using finite elements simulation and neural network method. Comput Methods Programs Biomed, 134: 69-78 (2016).

Bar-On, B., Wagner D. Mechanical model for staggered bio-structure. Journal of the Mechanics and Physics of Solids 59,1685–1701 (2011).

Bar-On, B., Wagner D. Structural motifs and elastic properties of hierarchical biological tissues – A review. J. Struct. Biol. 183, 149–164 (2013).

Bar-On, B., Wagner D. The emergence of an unusual stiffness profile in hierarchical biological mineralized tissues: A perspective. J. Struct. Biol. 201, 187–198 (2018).

Berhan, L., Sastry, A.M. Modeling percolation in high-aspect-ratio fiber systems. I. Soft-core versus hard-core models. Phys. Rev. E 75, 041120 (2007).

Bertolotti, F., Carmona. F.J., Dal Sasso, G., Ramírez-Rodríguez, G.B., Delgado-López, J.M., Pedersen, J.S., Ferri, F., Masciocchi, N., Guagliardi, A. On the amorphous layer in bone mineral and biomimetic apatite: A combined small- and wide-angle X-ray scattering analysis., Acta Biomater, doi.org/10.1016/j.actbio.2020.04.026. (2020)

Bini, F., Marinozzi, A., Marinozzi, F., Patanè, F. Microtensile measurements of single trabeculae stiffness in human femur. J. Biomech. 35, 1515–1519 (2002).

Bini, F., Pica, A., Marinozzi, A., Marinozzi, F. 3D diffusion model within the collagen apatite porosity: An insight to the nanostructure of human trabecular bone. PLoS One **12**(12), e0189041 (2017).

Bini, F., Pica, A., Marinozzi, A., Marinozzi, F. A 3D model of the effect of tortuosity and constrictivity on the diffusion in mineralized collagen fibril. Sci Rep 9, 2658 (2019).

Bloebaum, R.D., Skedros, J.G., Vajda, E.G., Bachus, K.N., Constantz, B.R. Determining mineral content variations in bone using backscattered electron imaging. Bone **20**, 485–490 (1997).

Boskey, A.L., Imbert, L. Bone quality changes associated with aging and disease: a review. Ann. N. Y. Acad. Sci. 1410, 93–106 (2017).

Boving, T.B., Grathwohl, P. Tracer diffusion coefficients in sedimentary rocks: Correlation to porosity and hydraulic conductivity. J. Contam. Hydrol. 53, 85–100 (2001).

Broadbent, S., Hammersley, J. Percolation processes: I. Crystals and mazes. Mathematical Proceedings of the Cambridge Philosophical Society, 53(3), 629-641 (1957).

Buehler M.J. Nature designs tough collagen: explaining the nanostructure of collagen fibrils. Proc Natl Acad Sci USA 103, 12285-12290 (2006).

Buehler M.J., Keten, K., Ackbarow, T. Theoretical and computational hierarchical nanomechanics of protein materials: Deformation and fracture, Prog Mat Sci, Volume 53, Issue 8 (2008).

Burger, C., Zhou, H.W., Wang, H., Sics, I., Hsiao, B.S., Chu, B., Graham, L., Glimcher, M.J. Lateral packing of mineral crystals in bone collagen fibrils. Biophys J 95: 1985-1992 (2008).

Burr, D. Bone material properties and mineral matrix contributions to fracture risk or age in women and men. J Musculoskel Neuron Interact; 2(3):201-204 (2002).

Burr, D., Chapter 1 - Bone Morphology and Organization, in Basic and Applied Bone Biology (Second Edition), Editor(s): David B. Burr, Matthew R. Allen, Academic Press, pp3 -26 (2019).

Cardoso, L., Fritton, S.P., Gailani, G., Benalla, M., Cowin, S.C. Advances in assessment of bone porosity, permeability and interstitial fluid flow. J. Biomech. 46 (2), 253–265 (2013).

Carles, G., Zammit, P., Harvey, A.R. Holistic Monte-Carlo optical modelling of biological imaging. Sci Rep 9, 15832 (2019).

Carneiro, I., Carvalho, S., Henrique, R., Oliveira, L.M., Tuchin, V.V. A robust ex vivo method to evaluate the diffusion properties of agents in biological tissues. J. Biophotonics. 12: e201800333 (2019).

Cassella, J.P., Barber, P., Catterall, A.C., Ali, S.Y. A morphometric analysis of osteoid collagen fibril diameter in osteogenesis imperfecta. Bone. 15(3): 329-34 (1994).

Chiavazzo, E., Fasano, M., Asinari, P., Decuzzi, P. Scaling behaviour for the water transport in nanoconfined geometries. Nat. Commun. 5, 1–11 (2014).

Chimene, D., Miller, L., Cross, L.M., Jaiswal, M.K., Singh, I., Gaharwar, A.K. Nanoengineered osteoinductive bioink for 3D bioprinting bone tissue. ACS Appl. Mater. Interfaces 12, 15976–15988 (2020).

Combes, C., Cazalbou, S., Rey, C. Apatite biominerals, Minerals, 6, 34 (2016).

Comte de Buffon, Leclerc, G.L. Solutions des problémes qui regardoient le jeu du franc carreau. Histoire de l'Acadèmie Royale des Sciences de Paris, pp. 43–45 (1733).

Cowin, S.C. (Ed.). Bone Mechanics Handbook (2nd ed.). CRC Press (2001).

Cowin, S.C. Bone poroelasticity. J. Biomech. 32, 217–238 (1999).

Craig, A.S., Parry, D.A. Growth and development of collagen fibrils in immature tissues from rat and sheep. Proc R Soc Lond B Biol Sci; 212(1186): 85-92 (1981).

Cui, F.Z., Li, Y., Ge, J. Self-assembly of mineralized collagen composites. Mater Sci Eng R 57, 1–27 (2007).

Curie J.A. Gaseous Diffusion in Porous Media. Part 1. A non-steady state method. Br. J. Appl. Phys. 11, 314–317 (1960).

Currey JD. The relationship between stiffness and mineral content of bone. J Biomech, 2, 477-480 (1969).

Dant J.T., Richardson, R.B., Nie, L.H. Monte Carlo simulation of age-dependent radiation dose from alpha- and beta-emitting radionuclides to critical trabecular bone and bone marrow targets. Phys. Med. Biol. 58, 3301–3319 (2013).

De Gennes, The Physics of Liquid Crystals, Clarendo Press Oxford (1993).

Depalle B., Qin, Z., Shefelbine, S.J., Buehler, M.J. Large deformation mechanisms, plasticity and failure of an individual collagen fibril with different mineral content. J. Bone Miner. Res. 31, 380-390 (2016).

Derwin, K.A., Soslowsky, L.J. A quantitative investigation of structure-function relationships in a tendon fascicle model. J Biomech Eng. 121(6):598-604 (1999).

Di Tommaso, D., Prakash, M., Lemaire, T., Lewerenz, M., De Leeuw, N.H., Naili, S. Molecular Dynamics Simulations of Hydroxyapatite Nanopores in Contact with Electrolyte Solutions: The Effect of Nanoconfinement and Solvated Ions on the Surface Reactivity and the Structural, Dynamical, and Vibrational Properties of Water. Crystals 7, 57 (2017).

Dubey, D.K., Tomar, V. Role of the nanoscale interfacial arrangement in mechanical strength of tropocollagen-hydroxyapatite-based hard biomaterials. Acta Biomater 5(7): 2704-16 (2009).

Dutta, A., Vanderklok, A., Tekalur, S.A. High strain rate mechanical behavior of seashell-mimetic composites: Analytical model formulation and validation. Mech. Mater. 55, 102–111, (2012).

Eppell, S.J., Tong, W., Katz, J.L., Kuhn, L., Glimcher, M.J. Shape and size of isolated bone mineralites measured using atomic force microscopy. J Orthop Res 19, 1027-1034 (2001).

Epstein N. On tortuosity and the tortuosity factor in flow and diffusion through porous media. Chen Eng Science 44: 777-779 (1989).

Fang, M., Banaszak Holl, M.M. Variation in type I collagen fibril nanomorphology: the significance and origin. BoneKEy Reports 2, Article number 394 (2013).

Fernández-Seara, M.A., Wehrli, S.L., Wehrli, F.W. Diffusion of Exchangeable Water in Cortical Bone Studied by Nuclear Magnetic Resonance, Biophys J 82: 522-529 (2002).

Fielder, M., Nair, A.K. Effects of hydration and mineralization on the deformation mechanisms of collagen fibrils in bone at the nanoscale. Biomech Model Mechanobiol 18, 57–68 (2019).

Finner, S.P., Kotsev, M.I., Miller, M.A., van der Schoot, P. Continuum percolation of polydisperse rods in quadrupole fields: Theory and simulations. J Chem Phys. 148(3): 034903 (2018).

Fratzl, P. Collagen. Structure and Mechanics. Springer, New York (2008).

Fratzl, P., Groschner, M., Vogl, G., Plenk, H.Jr., Eschberger, J., Fratzl-Zelman N., Koller, K., Klaushofer, K. Mineral crystals in calcified tissues: a comparative study by SAXS. J Bone Miner Res., 7: 3 (1992).

Fratzl, P., Gupta, H.S., Paschalis, E.P., Roschger, P. Structure and mechanical quality of the collagen-mineral nano-composite in bone. J Mater Chem; 14: 2115–2123 (2004).

Fratzl, P., Weinkamer, R. Nature's hierarchical materials. Progr Mat Sci 52, 1263–1334 (2007).

Frenkel, D., Smit, B. Understanding Molecular Simulations. From Algorithms to applications. Academic Press (2002).

Friedman, S.P., Seaton, N.A. A corrected tortuosity factor for the network calculation of diffusion coefficients. Chem Eng Science 50: 897-900 (1995).

Fritton, S.P., Weinbaum, S. Fluid and solute transport in bone: flow-induced mechanotransduction. Ann. Rev. Fluid Mech. 41, 347–374 (2009).

Fu, C., Jin, X., Ye, H., Jin, N. Theoretical and Experimental Investigation of Loading Effects on Chloride Diffusion in Saturated Concrete. J Adv Concr Technol Volume 13, Issue 1, Pages 30-43 (2015).

Gao, H., Ji, B., Jager, I.L., Arzt, E., Fratzl, P. Materials become insensitive to flaws at nanoscale: lessons from nature. Proc Natl Acad Sci USA 100, 5597-5600 (2003).

Garboczi, E.J., Snyder, K.A, Douglas, J.F, Thorpe, M.F. Geometrical percolation threshold of overlapping ellipsoids. Phys. Rev. E 52, 819 (1995).

Gatti, V., Azoulay, E.M., Fritton, S.P. Microstructural changes associated with osteoporosis negatively affect loading-induced fluid flow around osteocytes in cortical bone. J. Biomech. 66, 127–136, (2017).

Genin, G.M., Kent, A., Birman, V., Wopenka, B., Pasteris, J.D., Marquez, P.J., Thomopoulos, S. Functional Grading of Mineral and Collagen in the Attachment of Tendon to Bone. Biophys J 97: 976–985 (2009).

Genova, T., Roato, I., Carossa, M., Motta, C., Cavagnetto, D., Mussano, F. Advances on Bone Substitutes through 3D Bioprinting. Int J Mol Sci. 21: 7012 (2020).

Georgiadis, M., Guizar-Sicairos, M., Zwahlen, A., Trüssel, A.J., Bunk, O., Müller, R., Schneider, P. 3D scanning SAXS: A novel method for the assessment of bone ultrastructure orientation. Bone 71, 42–52, (2015).

Georgiadis, M., Müller, R., Schneider, P. Techniques to assess bone ultrastructure organization: orientation and arrangement of mineralized collagen fibrils. J. R. Soc. Interface 13, ID 20160088 (2016).

Gerbaix, M., Gnyubkin, V., Farlay, D., Olivier, C., Ammann, P., Courbon, G., Laroche, N., Genthial, R., Follet, H., Peyrin, F., Shenkman, B., Gauquelin-Koch, G., Vico, L. One-month spaceflight compromises the bone microstructure, tissue-level mechanical properties, osteocyte survival and lacunae volume in mature mice skeletons. Sci. Rep. 7, 1–12 (2017).

Ghanbarian, B., Hunt, A. G., Ewing, R. P., Sahimi, M. Tortuosity in Porous Media: A Critical Review. Soil Sci. Soc. Am. J. 77, 1461-1477, (2013).

Glimcher, M.J. Molecular biology of mineralized tissues with particular reference to bone. Rev Mod Phys, 31 (2): 359-393 (1959).

Gong, T., Xie, J., Liao, J., Zhang, T., Lin, S., Lin, Y. Nanomaterials and bone regeneration. Bone Res 3, 15029 (2015).

Grünewald, T.A., Liebi, M., Wittig, N.K., Johannes, A., Sikjaer, T., Rejnmark, L., Gao, Z., Rosenthal, M., Guizar-Sicairos, M., Birkedal, H., Burghammer, M. Mapping the 3D orientation of nanocrystals and nanostructures in human bone: Indications of novel structural features. Sci. Adv. 6: eaba4171 (2020).

Gu, H., Wang, J., Yu, C. Three-dimensional Modeling of Percolation Behavior of Electrical Conductivity in Segregated Network Polymer Nanocomposites Using Monte Carlo Method. Adv Mat. 5(1): 1-8 (2016).

Gupta, H.S., Seto, J., Wagermaier, W., Zaslansky, P., Boesecke, P., Fratzl, P. Cooperative deformation of mineral and collagen in bone at the nanoscale. Proc Natl Acad Sci USA, 103 (47): 17741–17746 (2006).

Habelitz, S., Balooch, M., Marshall, S.J., Balooch, G., Marshall, G.W.Jr. In situ atomic force microscopy of partially demineralized human dentin collagen fibrils. J Struct Biol. 138(3):227-36 (2002).

Hambli, R., Barkaoui, A. Physically based 3D finite element model of a single mineralized collagen microfibril. J Theor Biol; 301: 28–41 (2012).

Hamed, E., Jasiuk, I. Elastic modeling of bone at nanostructural level. Mat Sci Eng R 73 27–49 (2012).

Hassenkam, T., Fantner, G.E., Cutroni, J.A., Weaver, J.C., Morse, D.E., Hansma, P.K. High-resolution AFM imaging of intact and fractured trabecular bone. Bone 35, 4–10 (2004).

Hebbeker, P., Linse, P., Schneider, S. Optimal Displacement Parameters in Monte Carlo Simulations. J Chem Theory Comput 12 (4), 1459-1465 (2016).

Herega, A. Some Applications of the Percolation Theory: Brief Review of the Century Beginning, J Mat Sci Eng A5 (11-12) 409-414 (2015)

Hodge, A.J., Petruska, J.A. Recent studies with the electron microscope on ordered aggregates of the tropocollagen molecule. In: Ramachandran (Ed.), Aspects of Protein Structure. Academic Press. 289–300 (1963).

Holzer, L., Wiedenmann, D., Münch, B., Keller, L., Prestat, M., Gasser, Ph., Robertson, I., Grobéty, B. The influence of constrictivity on the effective transport properties of porous layers in electrolysis and fuel cells. J. Mater. Sci. 48, 2934–2952 (2013).

Hrabe, J., Hrabětová, S., Segeth, K. A model of effective diffusion and tortuosity in the extracellular space of the brain. Biophys. J. 87, 1606–1617 (2004).

Jäger, C., Welzel, T., Meyer-Zaika, W., Epple, M. A solid-state NMR investigation of the structure of nanocrystalline hydroxyapatite. Magn. Reson. Chem. 44: 573–580 (2006).

Jäger, I., Fratzl, P. Mineralized collagen fibrils: A mechanical model with a staggered arrangement of mineral particles. Biophys. J. **79**, 1737–1746 (2000).

Jaschouz, D., Paris, O., Roschger, P., Hwang, H. S., Fratzl, P. Pole figure analysis of mineral nanoparticle orientation in individual trabecula of human vertebral bone. J. Appl. Crystallogr. 36, 494–498 (2003).

Jin, S., Zador Z., Verkman A.S. Random-Walk model of diffusion in three dimensions in brain extracellular space: comparison with microfiberoptic photobleaching measurements. J Biophys, 95, 1785-1794 (2008).

Katz, E.P., Li, S.T. Structure and Function of Bone Collagen Fibrils. J. Mol. Biol. 80, 1-15 (1973).

Kilian, D., Ahlfeld, T., Akkineni, A.R., Bernhardt, A., Gelinsky, M, Lode, A. 3D Bioprinting of osteochondral tissue substitutes – in vitro-chondrogenesis in multi-layered mineralized constructs. Sci Rep 10, 8277 (2020).

Kopera, B.A.F., Retsch, M. Computing the 3D Radial Distribution Function from Particle Positions: An Advanced Analytic Approach. Analytical Chemistry 90 (23), 13909-13914 (2018).

Landis, W.J., Silver, F.H. The structure and function of normally mineralizing avian tendons. Comp. Biochem. Physiol. A 133, 1135–1157 (2002).

Landis, W.J., Song, M.J., Leith, A., McEwen, L., McEwen, B.F. Mineral and organic matrix interaction in normally calcifying tendon visualized in three dimensions by high-voltage electron microscopic tomography and graphic image reconstruction. J Struct Biol 110: 39–54 (1993).

Launey, M.E., Buehler, M.J., Ritchie, R.O. On the Mechanistic Origins of Toughness in Bone. Annu. Rev. Mater. Res. 40, 25–53, (2010).

Lee, S.B, Torquato, S. Pair connectedness and mean cluster size for continuum-percolation models: Computer-simulation results. J. Chem. Phys. 89 (10) (1988).

Lees, S. Considerations regarding the structure Of the mammalian mineralized osteoid From viewpoint of the generalized Packing model. Connect Tiss Res, 16: 281-303 (1987).

Leigh, J.W., Bryant, D. Monte Carlo Strategies for Selecting Parameter Values in Simulation Experiments. Syst Biol 64(5): 741-51 (2015).

Lemaire, T., Pham, T.T., Capiez-Lernout, E., de Leeuw, N.H., Naili, S. Water in hydroxyapatite nanopores: possible implications for interstitial bone fluid flow. J Biomech; 48: 3066-3071 (2015).

Lemaire, V., Tobin, F. L., Greller, L. D., Cho, C. R., Suva, L. J. Modeling the interactions between osteoblast and osteoclast activities in bone remodeling. J. Theor. Biol. 229, 293–309 (2004).

Li, M., Wang, L., Zhang, W., Putnis, C.V., Putnis, A. Direct observation of spiral growth, particle attachment and morphology evolution of hydroxyapatite. Cryst. Growth Des. 16, 4509-4518 (2016).

Liebi, M., Georgiadis, M., Menzel, A., Schneider, P., Kohlbrecher, J., Bunk, O., Guizar-Sicairos, M. Nanostructure surveys of macroscopic specimens by small-angle scattering tensor tomography. Nature 527, 349–352 (2015)

Lin J., Chen, H., Xu, W. Geometrical percolation threshold of congruent cuboidlike particles in overlapping particle systems. Phys Rev E 98, 012134 (2018).

Liu Y, Thomopoulos, S., Chen, C., Birman, V., Buehler, M.J., Genin, G.M. Modelling the mechanics of partially mineralized collagen fibrils, fibres and tissue. J. R. Soc. Interface 11, 20130835 (2013).

Luengo, D., Martino, L., Bugallo, M., Elvira, V., Sarkka, S. A survey of Monte Carlo methods for parameter estimation. EURASIP J. Adv. Signal Process. 2020, 25 (2020).

Marinozzi, F., Bini, F., De Paolis, A., De Luca, R., Marinozzi, A. Effects of hip osteoarthritis on mechanical stimulation of trabecular bone: A finite element study. J. Med. Biol. Eng. 35, 535–544 (2015).

Marinozzi, F., Bini, F., De Paolis, A., Zuppante, F., Bedini, R., Marinozzi, A. A finite element analysis of altered load distribution within femoral head in osteoarthritis. Comput. Methods Biomech. Biomed. Eng. Imaging Vis. 3, 84–90 (2015).

Marinozzi, F., Bini, F., Marinozzi, A. Evidence of entropic elasticity of human bone trabeculae at low strains. J. Biomech. 44, 988–991, (2011).

Marinozzi, F., Bini, F., Marinozzi, A. Water uptake and swelling in single trabeculæ from human femur head. Biomatter 4, 1–6 (2014a).

Marinozzi, F., Bini, F., Marinozzi, A., Zuppante, F., De Paolis, A., Pecci, R., Bedini R. Technique for bone volume measurement from human femur head samples by classification of micro-CT image histograms. Ann. Ist. Super. Sanità, 49, 300–305, 2013.

Marinozzi, F., Bini, F., Quintino, A., Corcione, M., Marinozzi, A. Experimental study of diffusion coefficients of water through the collagen: Apatite porosity in human trabecular bone tissue. Biomed Res. Int. 2014, Article ID 796519 (2014b).

Marinozzi, F., Marinozzi, A., Bini, F., Zuppante, F., Pecci, R., Bedini, R. Variability of morphometric parameters of human trabecular tissue from coxo-arthritis and osteoporotic samples. Ann. Ist. Super. Sanità, 48, 19–25, (2012).

Mathew M., Schilling, T., Oettel, M. Connectivity percolation in suspensions of hard platelets. Phys. Rev. E 85, 061407 (2012).

Matyka, M., Khalili, A., Koza, Z. Tortuosity-porosity relation in porous media flow. Phys. Rev. E. 78, ID 026306 (2008).

McNally, E.A., Schwarcz, H.P., Botton, G.A., Arsenault, A.L. A model for the ultrastructure of bone based on electron microscopy of ion-milled sections. PLoS One **7**, e29258 (2012).

McNamara, L.M., Prendergast, P.J., Schaffler, M.B. Bone tissue material properties are altered during osteoporosis. J Musculoskelet Neuronal Interact 5, 342-343 (2005).

Metropolis, N., Rosenbluth, A.W., Rosenbluth, M.N., Teller, A.H., Teller, E. Equation of State Calculations by Fast Computing Machines. The Journal of Chemical Physics 21, 1087 (1953).

Michaels, A.S. Diffusion in a Pore of Irregular Cross Section-a Simplified Treatment. Al. Ch.E. Journal. 5(2): 270-271 (1959).

Miller, M.A. On structural correlations in the percolation of hard-core particles. J. Chem. Phys. 131, 066101 (2009).

Milovanovic, P., Potocnik, J., Stoiljkovic, M., Djonic, D., Nikolic, S., Neskovic, O., Djuric, M., Rakocevic, Z. Nanostructure and mineral composition of trabecular bone in the lateral femoral neck: Implications for bone fragility in elderly women. Acta Biomater 7, 3446-3451 (2011).

Misof, K., Rapp, G., Fratzl, P. A new molecular model for collagen elasticity based on synchrotron X-ray scattering evidence. Biophys J 72, 1376–1381 (1997).

Moussatov, A., Ayrault, C., Castagnède, B. Porous material characterization - Ultrasonic method for estimation of tortuosity and characteristic length using a barometric chamber. Ultrasonics 39, 195–202 (2001).

Münch, B., Holzer, L. Contradicting geometrical concepts in pore size analysis attained with electron microscopy and mercury intrusion. J. Am. Ceram. Soc. 91, 4059–4067 (2008).

Nair, A., Gautieri, A., Chang, S.W., Buehler, M.J. Molecular mechanics of mineralized collagen fibrils in bone. Nat Commun 4, 1724 (2013).

Newman M.E.J., Ziff, R.M. Fast Monte Carlo algorithm for site or bond percolation. Phys. Rev. E 64, 016706 (2001).

Ni Q., Nyman, J.S., Wang, X., De Los Santos, A., Nicolella, D.P. Assessment of water distribution changes in human cortical bone by nuclear magnetic resonance," Measurement Science and Technology, 18(3): 715-723 (2007).

Nikolov, S., Raabe, D. Hierarchical modelling of the elastic properties of bone at submicron scales: the role of extrafibrillar mineralization. Biophys. J. 94, 4220-4232, (2008).

Nudelman, F., Lausch, A.J., Sommerdijk, N.A.J.M., Sone, E.D. In vitro models of collagen biomineralization. J Struct Biol 183, 258–269 (2013).

Nudelman, F., Pieterse, K., George, A., Bomans, P.H., Friedrich, H., Brylka, L.J., Hilbers, P.A., de With, G., Sommerdijk, N.A. The role of collagen in bone apatite formation in the presence of hydroxyapatite nucleation inhibitors. Nature Mater 9, 1004–1009 (2010).

Olszta, M.J., Cheng, X., Jee, S.S., Kumar, R., Kim, Y.Y., Kaufman, M.J., Douglas, E.P., Gower, L.B. Bone structure and formation: A new perspective. Mater. Sci. Eng. R Reports 58, 77–116, (2007).

Orgel, J.P.R.O., Irving, T.C., Miller, A., Wess, T.J. Microfibrillar structure of type I collagen in situ. Proc Natl Acad Sci USA 103 (24), 9001-9005 (2006).

Orgel, J.P.R.O., Persikov, A.V., Antipova, O. Variation in the Helical Structure of Native Collagen. PLoS ONE 9(2): e89519 (2014).

Petersen, E.E. Diffusion in a pore varying cross section. Al. Ch.E. Journal. 4(3): 343-345 (1958).

Pham, T.T., Lemaire, T., Capiez-Lernout, E., Lewerenz, M., To, Q.D., Christie, J.K., Di Tommaso, D., de Leeuw, N.H., Naili, S. Properties of water confined in hydroxyapatite nanopores as derived from molecular dynamics simulations. Theor. Chem. Acc. 134, 1–14 (2015).

Pike, G.E., Seager, C.H. Percolation and conductivity: A computer study. I Phys. Rev. B 10, 14 (1974).

Posner, A.S. Crystal Chemistry of bone mineral. Physiological Review, 49: 4 (1969).

Reznikov, N., Chase, H., Brumfeld, V., Shahar, R., Weiner, S. The 3D structure of the collagen fibril network in human trabecular bone: Relation to trabecular organization. Bone 71, 189–195, (2015).

Reznikov, N., Shahar, R., Weiner, S. Bone hierarchical structure in three dimensions. Acta Biomater 10, 3815–3826 (2014).

Reznikov. N., Bilton, M., Lari, L., Stevens, M.M., Kröger, R. Fractal-like hierarchical organization of bone begins at the nanoscale. Science, 360, eaao2189 (2018).

Rho, J.Y., Kuhn-Spearing, L., Zioupos, P. Mechanical properties and the hierarchical structure of bone. Med Eng Phys; 20: 92–102 (1998).

Rinnerthaler, S., Roschger, P., Jakob, H., Nader, A., Klaushofer, K., Fratzl, P. Scanning Small Angle X-ray Scattering Analysis of Human Bone Sections. Calcif Tissue Int 64, 422–429 (1999).

Rintoul, M.D., Torquato, S. Precise determination of the critical threshold and exponents in a three-dimensional continuum percolation model. J. Phys. A: Math. Gen. 30, L585–L592 (1997).

Robinson, R.A, Watson, M.L. Collagen-crystal relationships in bone as seen in the electron microscope. Anat Rec. 114(3): 383-409 (1952).

Roschger, P., Paschalis, E.P., Fratzl, P., Klaushofer, K. Bone mineralization density distribution in health and disease. Bone 42, 456–466 (2008).

Rottreau, T.J., Parlett, C.M.A., Lee, A.F., Evans, R. Diffusion NMR Characterization of Catalytic Silica Supports: A Tortuous Path. J. Phys. Chem. C 121, 16250–16256 (2017).

Rubin, M.A., Jasiuk, I., Taylor, J., Rubin, J., Ganey, T., Apkarian, R.P. TEM analysis of the nanostructure of normal and osteoporotic human trabecular bone. Bone 33, 270–282 (2003).

Sabet, F.A., Raeisi Najafi, A., Hamed, E., Jasiuk, I. Modelling of bone fracture and strength at different length scales: a review. Interface Focus 6: 20150055 (2016).

Schilling, T., Miller, M.A., van der Schoot, P. Percolation in suspensions of hard nanoparticles: From spheres to needles EPL 111 56004 (2015).

Schwarcz, H.P., Abueidda, D., Jasiuk, I. The ultrastructure of bone and its relevance to mechanical properties. Front. Phys. 5(39) (2017).

Seidel, R., Gourrier, A., Kerschnitzki, M., Burghammer, M., Fratzl, P., Gupta, H.S., Wagermaier, W. Synchrotron 3D SAXS analysis of bone nanostructure. Bioinspired, Biomimetic and Nanobiomaterials, 1:123-131 (2011).

Shah, F.A., Zanghellini, E., Matic, A., Thomsen, P., Palmquist, A. The Orientation of Nanoscale Apatite Platelets in Relation to Osteoblastic–Osteocyte Lacunae on Trabecular Bone Surface. Calcif Tissue Int 98, 193–205 (2016).

Shahar, R., Weiner, S. Open questions on the 3D structures of collagen containing vertebrate Tissues. J Struct Biol. 201(3): 187-198 (2018).

Shen, L., Chen, Z. Critical review of the impact of tortuosity on diffusion. Chem. Eng. Sci. 62, 3748–3755 (2007).

Sherwood, J.D. Packing of spheroids in three-dimensional space by random sequential addition. J. Phys. A: Math. Gen. 30, L839–L843 (1997).

Siegmund, T., Allen, M.R., Burr, D.B. Failure of mineralized collagen fibrils: modeling the role of collagen cross-linking. J Biomech. 41(7):1427-35 (2008).

Sobieski, W., Zhang, Q., Liu, C. Predicting Tortuosity for Airflow Through Porous Beds Consisting of Randomly Packed Spherical Particles. Transp Porous Med 93, 431–451 (2012).

Spiesz, E.M., Reisinger, A.G., Kaminsky, W., Roschger, P., Pahr, D.H., Zysset, P.K. Computational and experimental methodology for site-matched investigations of the influence of mineral mass fraction and collagen orientation on the axial indentation modulus of lamellar bone. J Mech Behav Biomed Mater.28:195-205 (2013).

Stauffer, D., Aharony, A. Introduction to percolation, Taylor & Francis Group (1985).

Stenzel, O., Pecho, O., Holzer, L., Neumann, M., Schmidt, V. Predicting effective conductivities based on geometric microstructure characteristics. AIChE J. 62, 1834–1843 (2016).

Stock, S.R. The Mineral–Collagen Interface in Bone. Calcif Tissue Int 97, 262–280 (2015).

Su, X., Sun, K., Cui, F.Z., Landis, W.J. Organization of apatite crystals in human woven bone. Bone, 32: 150-162 (2003).

Svensson, R.B., Hassenkam, T., Grant, C.A., Magnusson, S.P. Tensile properties of human collagen fibrils and fascicles are insensitive to environmental salts. Biophys J. 99(12):4020-7 (2010).

Takahashi, H., Seida, Y., Yui, M. 3D X-ray CT and diffusion measurements to assess tortuosity and constrictivity in a sedimentary rock. diffusion-fundamentals.org. 11, 1–11 (2009).

Tong, W., Glimcher, M.J., Katz, J.L., Kuhn, L., Eppell, S.J. Size and shape of mineralites in young bovine bone measured by atomic force microscopy. Calcified Tissue Int; 72:592–598 (2003)

Torquato, S. Random heterogeneous materials: microstructure and macroscopic properties. Springer Science, New York (2002).

Traub, W., Arad, T., Weiner, S. Three-dimensional ordered distribution of crystals in turkey tendon collagen fibers. Proc Natl Acad Sci U S A. 86(24):9822-6 (1989).

Turunen, M.J., Kaspersen, J.D., Olsson, U., Guizar-Sicairos, M., Bech, M., Schaff, F., Tägil, M., Jurvelin, J.S., Isaksson, H. Bone mineral crystal size and organization vary across mature rat bone cortex. J Struct Biol 195, 337–344 (2016).

Valdés-Parada, F. J., Porter, M. L., Wood, B. D. The role of tortuosity in upscaling. Transp. Porous Med. 88, 1–30 (2011).

Van Brakel, J., Heertjes, P.M. Analysis of diffusion in macroporous media in terms of a porosity, a tortuosity and a constrictivity factor. Int J Heat Mass Transfer 17: 1093-1103 (1974).

Vercher, A., Giner, E., Arango, C., Tarancon, J.E., Fuenmayor, F.J. Homogenized stiffness matrices for mineralized collagen fibrils and lamellar bone using unit cell finite element models. Biomech Model Mechanobiol 13, 437–449 (2014).

Vercher-Martinez, A., Giner, E., Arango, C., Fuenmayor, F.J. Influence of the mineral staggering on the elastic properties of the mineralized collagen fibril in lamellar bone. J Mech Behav Biomed Mater, 42: 243-256 (2015).

Vesentini, S., Redaelli A., Gautieri A. Nanomechanics of collagen fibril. Muscles, Ligaments and Tendons Journal 3 (1): 23-34 (2013).

Viceconti, M. Multi scale modelling of the skeletal system, Cambridge University press (2012).

Voltolini, M., Wenk, H.R., Gomez Barreiro, J., Agarwal, S.C. Hydroxylapatite lattice preferred orientation in bone: a study of macaque, human and bovine samples. J. Appl. Cryst. 44, 928-934 (2011).

Von Euw, S., Chan-Chang, T.H.C., Paquis, C., Haye, B., Pehau-Arnaudet, G., Babonneau, F., Azaïs, T., Nassif, N. Organization of Bone Mineral: The Role of Mineral–Water Interactions. Geosciences, 8, 466 (2018).

Wagermaier W., K. Klaushofer, P. Fratzl. Fragility of bone material controlled by internal interfaces. Calcif. Tissue Int. 97, 201-212 (2015).

Wang Q., Wang, M., Liu, X., Wang, K., Fang, L., Ren, F., Lu, G. Effects of atomic level nano-structured hydroxyapatite on adsorption of bone morphogenetic protein-7 and its derived peptide by computer simulation. Sci Rep 7, 15152 (2017).

Wang, X., Qian, C. Prediction of microdamage formation using a mineral-collagen composite model of bone, J Biomech, 39, 595-602 (2006).

Wang, Y., Von Euw, S., Fernandes, F.M., Cassaignon, S., Selmane, M., Laurent, G., Pehau-Arnaudet, G., Coelho, C., Bonhomme-Coury, L., Giraud-Guille, M.M., Babonneau, F., Azaïs, T., Nassif, N. Water-mediated structuring of bone apatite. Nature materials; 12: 1144-1153 (2013).

Wegst, U., Bai, H., Saiz, E., Tomsia, A.P., Ritchie, R.O. Bioinspired structural materials. Nature Mater 14, 23–36 (2015).

Weiner S., Price, P.A. Disaggregation of bone into crystals. Calcif Tissue Int 39, 365-375 (1986).

Weiner, S., Arad, T., Traub, W. Crystal organization in rat bone lamellae. FEBS Lett, 285: 49-54 (1991).

Weiner, S., Wagner, H.D. The material bone: Structure-mechanical function relations. Annu Rev Mater Sci, 28: 271–298 (1998).

Wenger, M.P., Bozec, L., Horton, M.A., Mesquida, P. Mechanical properties of collagen fibrils. Biophys J. 93(4):1255-63 (2007).

Wigger, C., Plöze, M., Van Loon, L.R. Pore Geometry as a Limiting Factor for Anion Diffusion in Argillaceous Rocks. Clays Clay Miner. 66, 329–338 (2018).

Wilson, E.E., Awonusi, A., Morris, M.D., Kohn, D.H., Tecklenburg, M.M., Beck, L.W. Three structural roles for water in bone observed by solid-state NMR. Biophys J, 90: 3722-3731 (2006)

Wu, Y.S., van Vliet, L.J., Frijlink, H.W., van der Voort Maarschalk, K. The determination of relative path length as a measure for tortuosity in compacts using image analysis. Eur. J. Pharm. Sci. 28, 433–440 (2006).

Xu, Y., Nudelman, F., Eren, E.D., Wirix, M.J.M., Cantaert, B., Nijhuis, W.H., Hermida-Merino, D., Portale, G., Bomans, P.H.H., Ottmann, C., Friedrich, H., Bras, W., Akiva, A., Orgel, J.P.R.O., Meldrum, F.C., Sommerdijk, N. Intermolecular channels direct crystal orientation in mineralized collagen. Nat Commun 11, 5068 (2020).

Yamauchi, M., Katz, E.P., Otsubo, K., Teraoka, K., Mechanic, G.L. Cross-linking and stereospecific structure of collagen in mineralized and nonmineralized skeletal tissues. Connect Tissue Res 21(1-4):159-67 (1989).

Younge, K., Christenson, C., Bohara, A., Crnkovic, J., Saulnier, P. A model system for examining the radial distribution function Am. J. Phys. 72, 1247 (2004).

Yuan, F., Stock, S.R., Haeffner, D.R., Almer, J.D., Dunand, D.C., Brinson, L.C. A new model to simulate the elastic properties of mineralized collagen fibril. Biomech. Model. Mechanobiol. 10, 147–160 (2011).

Yun, M., Yu, B., Xu, P., Wu, J. Geometrical Models for Tortuosity of Streamlines in Three-Dimensional Porous Media. Can. J. Chem. Eng. 84, 301–309 (2006).

Zeng, X., Xu, X., Shenai, P.M., Kovalev, E., Baudot, C., Mathews, N., Zhao, Y. Characteristics of the Electrical Percolation in Carbon Nanotubes/Polymer Nanocomposites. J. Phys. Chem. C, 115, 44, 21685–21690 (2011).

Ziv, V., Weiner, S. Bone crystal sizes: a comparison of transmission electron microscopic and X-ray diffraction line width broadening techniques. Connect Tissue Res. 30(3):165-75 (1994).